Supplement of Earth Syst. Sci. Data, 17, 5377–5488, 2025
https://doi.org/10.5194/essd-17-5377-2025-supplement

Open Access Earth System Science Data

Supplement of

State of Wildfires 2024–2025

Douglas I. Kelley et al.

Correspondence to: Douglas I. Kelley (doukel@ceh.ac.uk), Chantelle Burton (chantelle.burton@metoffice.gov.uk), Francesca Di Giuseppe (francesca.digiuseppe@ecmwf.int), and Matthew W. Jones (matthew.w.jones@uea.ac.uk)

S2 Supplementary Material for Section 2: Context of Recent Extremes

S2.1 Method

S2.1.1 Contemporaneous Fire Weather

In this edition of the report, we introduce routine summaries of the extreme (95th percentile) fire weather days during the March 2024–February 2025 global fire season based on the fire weather index (FWI), a common metric of fire danger developed by the Canadian Forest Service as part of the Canadian Forest Fire Danger Rating System (CFFDRS) (van Wagner, 1987). The FWI comprises various components that consider the influence of weather on fire danger, with 2m temperature, 10m wind speed, precipitation, and 2m relative humidity as prerequisite variables. Higher FWI values are generally seen during droughts and heatwaves but they are more broadly indicative of meteorological conditions more conducive to wildfires in environments with sufficient fuel load (Di Giuseppe et al., 2016; Jones et al., 2022).

We base our analysis of extreme (95th percentile) fire weather on the FWI dataset derived from the Copernicus Climate Change Service ERA5 reanalysis (Hersbach et al., 2023; Vitolo et al., 2020) and maintained by the Copernicus Emergency Management Service (CEMS, version4.1 2019). This dataset provides global fire weather data at a 0.25° spatial resolution and daily temporal resolution. To identify extreme fire weather conditions, we computed the 95th percentile of daily FWI values at 0.25° resolution over the reference period March 1978–February 2025 (i.e., covering 46 fire seasons). For each fire season, we then calculated the number of days on which the daily FWI exceeded this threshold, yielding our estimate of extreme fire weather days, referred to as FWI_{95d}—defined as the annual number of days when fire weather conditions surpass the 95th percentile threshold.

Anomalies in FWI_{95d} for the March 2024–February 2025 fire season were subsequently calculated following the same methodology used for the observational fire variables, and are presented as (i) ranks, (ii) proportional anomalies, and (iii) standardised anomalies (see **Section 2.1.2 "Regions with Extreme Wildfire Seasons"**). The data produced using these methods are available from (Turco et al., 2025).

We adopt FWI_{95d} as our metric for extreme fire weather for several reasons. First, FWI_{95d} focuses on periods of high fire danger, when fire ignition and rapid spread are more likely (e.g. Barbero et al., 2014). Second, it has been widely used in previous studies assessing fire–climate relationships (Abatzoglou et al., 2019; Jones et al., 2022; Quilcaille et al., 2023) , supporting consistency with the broader literature. Third, and crucially for a global analysis, the use of a quantile-based threshold reduces the impact of regional biases in absolute FWI values, allowing for a more robust comparison of fire weather extremes across geographically diverse environments.

S2.1.2 21st Century Trends in Burned Area

To place recent extremes in the context of fire trends of the past two decades, we update our regional analyses of trends in annual BA from Jones et al. (2022). In contrast, we present trends that align more closely with global fire seasons, spanning the period March 2002-February 2025 rather than trends over calendar years. We quantified trends using the Theil-Sen slope estimator, which is useful when data may contain outliers or be non-normally distributed making it less sensitive to outliers than a standard least squares regression slope. Changes were calculated by multiplying trends (unit year^{-1}) by the number of fire

seasons in the period of coverage for each variable (**Section 2.1.1 "Input Data Uncertainties"**). Relative changes were calculated as the absolute changes divided by the mean annual BA during the period following (Andela et al., 2017; Jones et al., 2022). The significance of trends was evaluated using the Mann-Kendall test, with a confidence level set at 95%.

In addition to reporting trends in *total* BA, we also present trends in *forest* BA as these regularly diverge from total BA trends, following Jones et al. (2024a) see **Section 2.2.2**). Forest BA is calculated as described in **Section 2.1.1,** but after isolating burned cells in areas with tree cover exceeding 30% in NASA's annual MODIS MOD44B collection 6.0 Continuous Vegetation Field product (250m; Dimiceli et al., 2015). The 30% threshold is widely used amongst studies of forest cover change (Cunningham et al., 2020; e.g. Li et al., 2017; Sexton et al., 2016).

S2.2 Results

S2.2.1 Contemporaneous Fire Weather

Section 4 of this report comprehensively explores the drivers of the extreme fire season for 4 selected events during 2024-25, not only in terms of meteorological factors influencing the preconditioning of vegetation fuels for fire but also including factors such as fuel loading, land use and management, and ignition opportunities. However, because large-scale regional patterns of drought and heatwave are known to influence fire extent (Abatzoglou et al., 2018; Jolly et al., 2015; Jones et al., 2022), we briefly summarise here the meteorological circumstances underlying some of the regional extremes of the 2024-25 fire season identified above. Robust relationships are observed between fire weather and fire activity in regions with ample fuels across multiple decades, particularly in forests (Abatzoglou et al., 2018; Jones et al., 2022, 2024a; Turco et al., 2018).

Figure S2 shows world regions experiencing high levels of extreme fire weather during the 2024-25 fire season (data are available from Turco et al., 2025). Extreme fire weather was notably prevalent in the majority of regions in tropical South America, with the highest number of fire weather days on record in most states of Brazil, Bolivia and Peru and many other states of Colombia, Venezuela, and the Guianas experiencing a high-ranking–if not record-breaking–number of days with extreme fire weather. For example, Amazonas State in Brazil experienced more than 50 additional days of extreme fire weather than its annual mean and many regions saw more than a month of additional fire weather days than is the average year (**Figure S2**). The spatial pattern of fire weather anomalies (**Figure S2**) clearly aligns with the elevated fire activity across the Amazon, broader moist tropical forests, Pantanal, and Chiquitano regions of South America during 2024-25 (**Figure 2, Figure 3**). Similarly, Mesoamerica experienced an unusually high number of extreme fire weather days during 2024-25 (**Figure S2**) and this is likely one factor contributing to higher than average fire activity in parts of Mexico during 2024-25 (**Figure 2**, **Figure 3**).

In Canada, some anomalies in extreme fire weather were observed in the northernmost provinces of western Canada (e.g. Northwest territories) and some eastern provinces during 2024-25 (**Figure S2**). Although anomalies in BA and C emissions were indeed centred on the same regions of Canada, we note that the anomalies in extreme fire weather days were fairly small and overall less widespread than the anomalies in BA and C emissions. This evidence points towards other factors (beyond contemporaneous fire weather) as drivers of the elevated fire activity during 2024-25, potentially including the carryover effects of the prior-year heatwave and drought from 2023 and of overwintering ignitions from smouldering peat combustion (Scholten et al., 2021).

In Africa, widespread high fire weather was observed across the Congo basin during the 2024-25 fire season (**Figure S2**), aligning strongly with the anomalous BA and fire C emissions observed in the region (**Figure 2, Figure 3**). In Southern Africa, extreme fire weather anomalies were widespread (**Figure S2**) but also characteristically decoupled from anomalies in BA (**Figure 2**) due to the inverted relationship between fire weather and fire activity in this fuel-limited region, where fire weather tends to correlate with poor vegetation productivity (Jones et al., 2022).

In Eastern Europe, anomalies in extreme fire weather were centred on Ukraine and the Balkan states (**Figure S2**), corresponding with BA and C emissions anomalies in some parts of Ukraine, Serbia, and North Macedonia (**Figure 2**, **Figure 3**). However, spatial relationship between extreme fire weather and extreme fire activity was not direct in neighbouring regions, with western Turkey (for example) experiencing above-average BA and emissions (**Figure 2**, **Figure 3**) despite no clear anomaly in extreme fire weather (**Figure S2**). Similarly, anomalies in extreme fire weather spanned much of southern and southeast Asia (**Figure S2**), yet positive anomalies in BA and fire C emissions emerged in northern India, Nepal and Bangladesh but not in nearby parts of Thailand, Cambodia and Myanmar (**Figure 2**, **Figure 3**). In Siberia, a record-breaking number of extreme fire weather days occurred during the 2024-25 fire season (**Figure S2**) but did not translate into especially high BA or fire C emissions (**Figure 2**, **Figure 3**). This is a somewhat surprising finding for this region, given that the most extreme fire seasons of 2020 and 2021 were previously linked with extreme fire weather associated with heatwave and drought (Zheng et al., 2023).

Overall, these findings highlight that there is noise in the relationship between fire weather and BA, with extreme fire weather preconditioning vegetation to burn but a variety of other factors such as ignition availability, fuel loading, and management factors driving dissociation in certain regions and years. For certain focal events, **Section 4** formally evaluates the role of fire weather's sub-components (temperature, precipitation, humidity and wind speed) as drivers of fire alongside non-meteorological factors.

While the present report focuses primarily on explaining focal events that did emerge as extremes, we recognise the underexplored value of examining the factors that constrain fire occurrence in regions where anomalously high fire weather might otherwise be expected to drive extremes in burned area and associated carbon emissions. Future iterations of the State of Wildfires assessment may therefore consider giving greater emphasis to understanding why such extremes did not materialise. That said, this type of analysis has not, to our knowledge, been a common approach in fire science to date. For example, we are not aware of any formal attribution studies focusing on non-extreme fire events, in contrast to the growing number of attribution studies of extreme events. It may therefore be more appropriate for such investigations to be pursued initially as a dedicated exercise, whether within our network or by others.

S2.2.2 21st Century Trends in Burned Area

The anomalies of 2024-25 occur against a backdrop of trends in BA this century that point towards shifts in fire regime. **Figure S3** shows significant trends in BA and forest BA across the fire seasons in the period March 2002-February 2025 derived from MODIS BA data. While many world regions are experiencing declines in total BA, increases in forest BA are far more prevalent than declines at the scale of continental biomes, countries, and administrative regions.

In South America, trends in total and forest BA are varied. The more than doubling of both total and forest BA in Amazonas (significant at $p<0.05$; **Figure S3**), among the most pristine parts of Amazonia, contrasts with the neighbouring state of Pará, where total BA has fallen by 44% ($p<0.05$) as deforestation rates and deforestation-related fires have broadly declined

since their peak during the early 2000s (Mataveli et al., 2025). The anomalous fire activity and C emissions in Amazonas state during the 2024-25 fire season is consistent with the emerging pattern of increased fire extent within in the state, whereas in Pará and other regions of South America's tropical forests, the 2024-25 anomaly punctuates the either reducing or stable BA trends of recent decades.

More broadly across the tropics, total BA has reduced across many savannah regions of Africa, South America, and northern Australia (**Figure S3**). The low fire seasons of 2024-25 and 2023-24 in the African savannahs (**Section 2.2.1 "An Unprecedented Fire Season in South America"**) are highly consistent with the decline in BA seen in those regions this century. In tropical forests, BA has generally fallen in Southeast Asia, increased in the Congo basin, and shown no significant trend in South America. Hence, fires in the tropics do not show a consistent global trend (**Figure S3**). Notably, the BA anomalies seen in the Congo basin during the 2024-25 fire season appear to be an extension of a trend towards increased BA across in the region over recent decades (**Figure S3**).

Northern hemisphere extratropical regions in North America and Asia show a clear pattern of increased forest BA since 2002 (**Figure S3**), which is also visible on national scales in Canada and the US and on state/provincial scales in various states of western and eastern Canada, the western US, and northeast Russia. The consecutive large anomalies in BA in Canada during 2023-2024 and 2024-25 align with the doubling of forest BA seen in Canada across fire seasons since 2002 (significant trend, $p < 0.05$) and a 22% increase in total BA in Canada (marginally significant at $p < 0.1$). Three Canadian provinces showed significant increases in both total and forest BA this century: British Columbia (+39-49%); Northwest Territories (+52-80%), and; Yukon (+75-141%). No Canadian provinces experienced a significant decline in forest BA or total BA. More widely, there was a 51% increase in forest BA in the North American boreal forest biome since 2002, and a 118% increase across the pan-boreal forest biome of North America and Eurasia. The succession of events affecting boreal forests in Canada in 2023 and 2024, Siberia in 2020, and both North America and Siberia during 2021 are part of a continued trend towards rising fire extent in high latitude forests this century (Jones et al., 2024a).

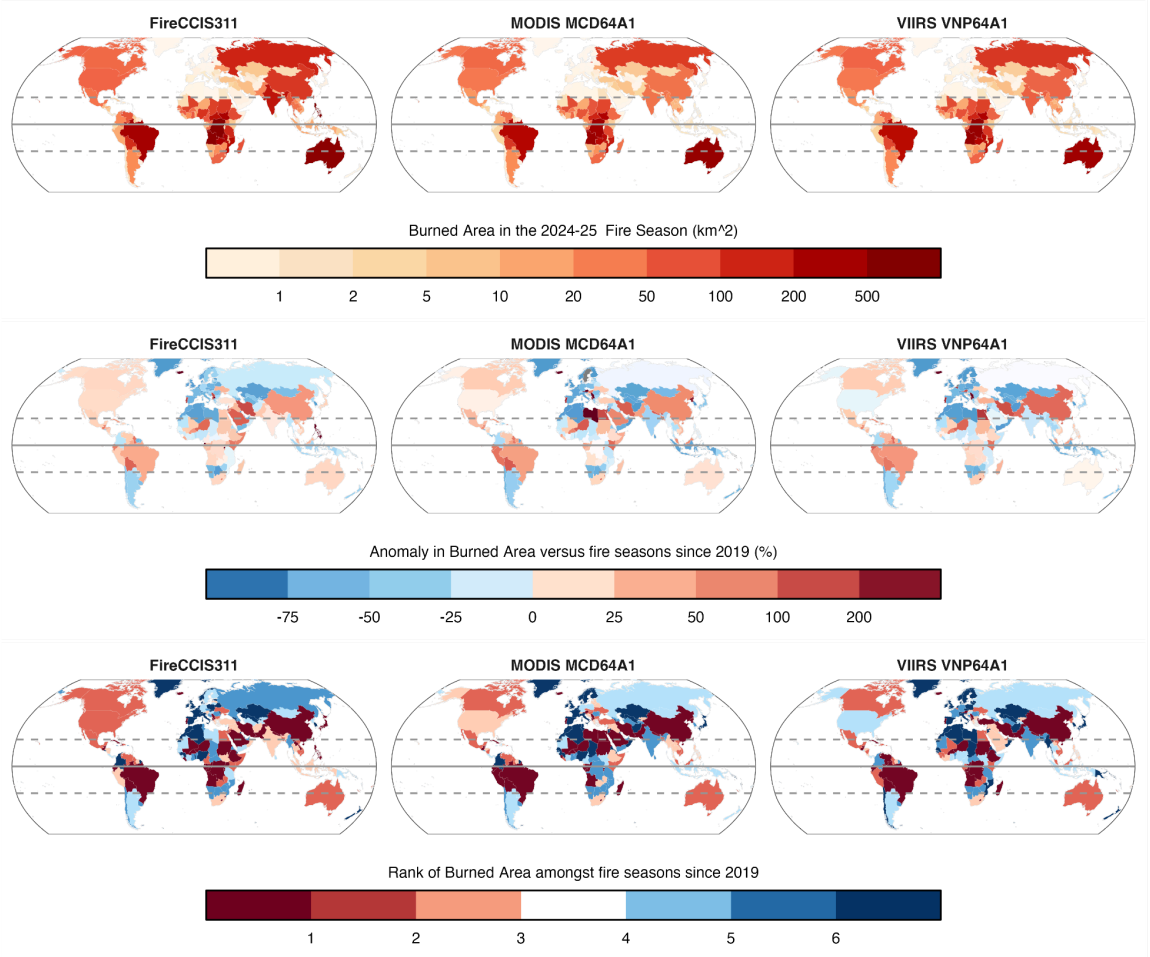

Figure S1: Comparison of the burned area (BA) estimates from **(left column)** the ESA Climate Change Initiative FireCCI product Sentinel-3 SYN Burned Area Grid product, version 1.1 (Chuvieco et al., 2024; FireCCIS311; Lizundia-Loiola et al., 2022), **(middle column)** the VIIRS BA product produced by NASA (VNP64A1 v002) (Giglio, 2024; Zubkova et al., 2024) and **(right)** the MODIS BA product produced by NASA (MCD64A1 collection 6.1; Giglio et al., 2018).

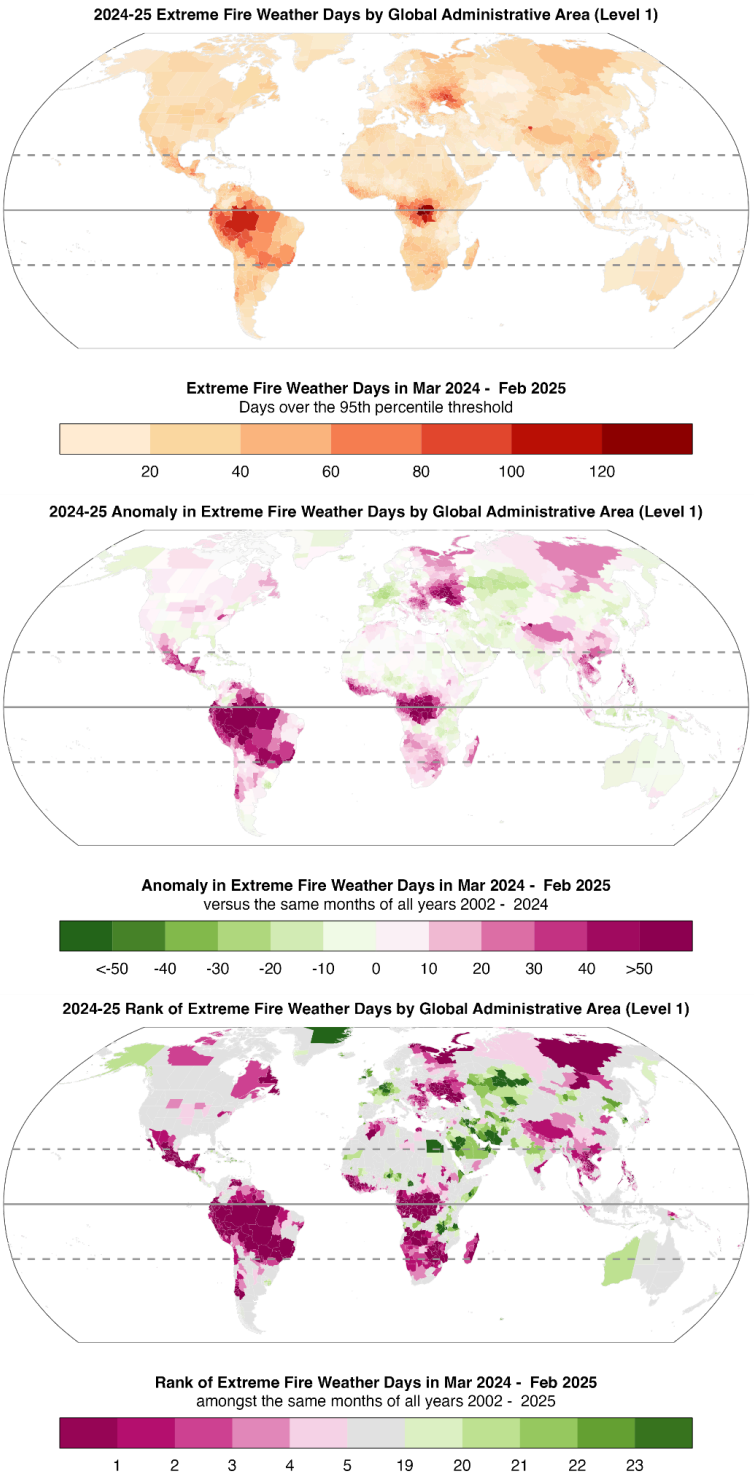

Figure S2: Extreme fire weather in the past fire season, including **(top panel)** the number of days with extreme (95th percentile) fire weather during the 2024-25 fire season, **(middle panel)** the anomaly versus the mean of all prior fire seasons 2002-2024, and **(bottom panel)** rank amongst all fire seasons since 2002.

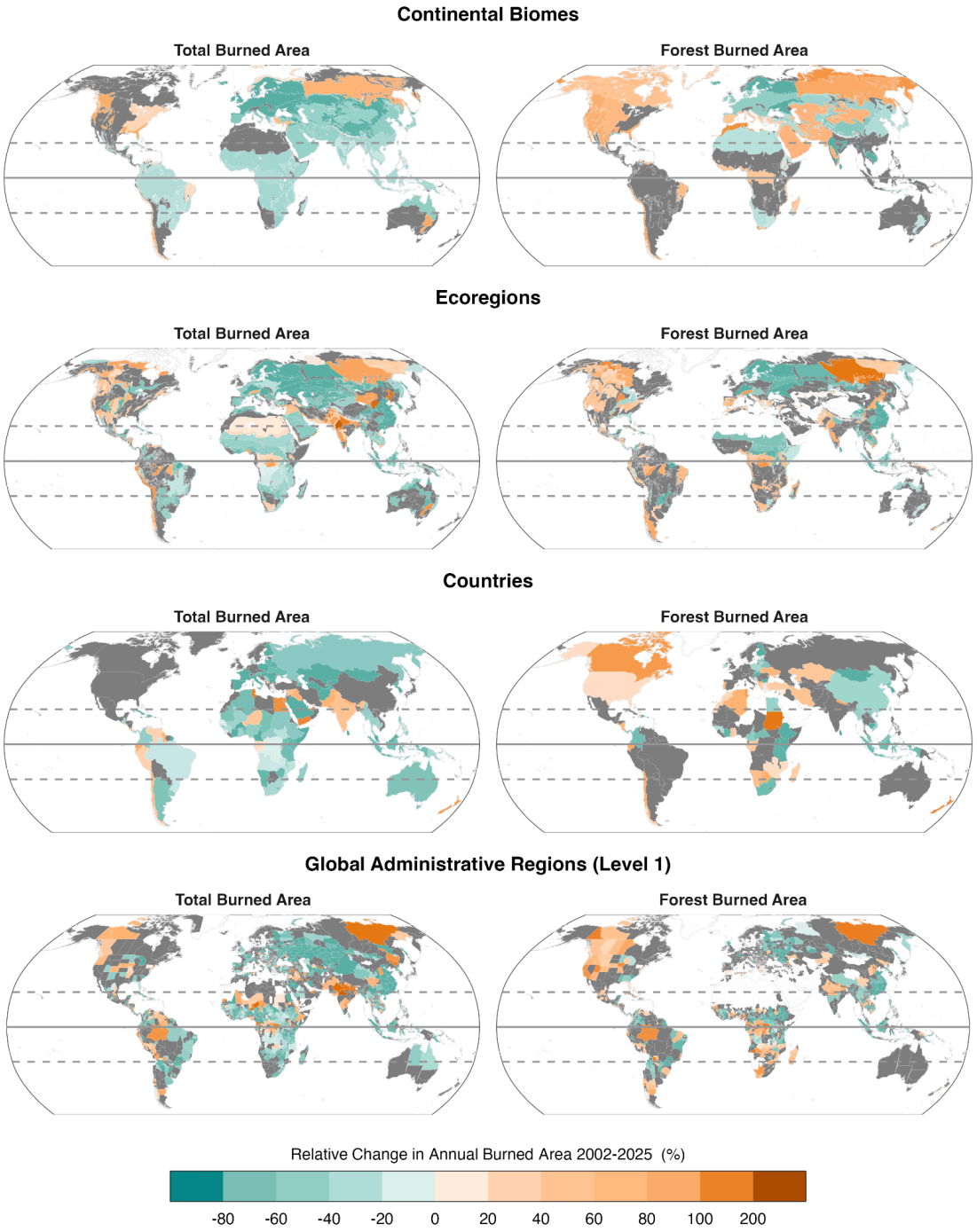

Figure S3: Relative changes (%) in **(left panels)** total annual BA and **(right panels)** forest BA across March-February fire seasons during 2002-2025 for three regional layers: **(top panels)** continental biomes; **(middle panels)** countries, and; **(bottom panels)** level 1 administrative regions (e.g. states or provinces). Forest BA considers only areas with tree cover over 30% at the native (500 m) resolution of the BA observations. Relative changes are calculated as the trend in BA across fire seasons March 2002-February 2003 through March 2024-February 2025 multiplied by the number of years in the time series and divided by the mean annual BA during the period. Trends in BA are derived using the Theil-Sen slope estimator. Only significant trends in BA are shown (dark grey fill signifies no significant trend).

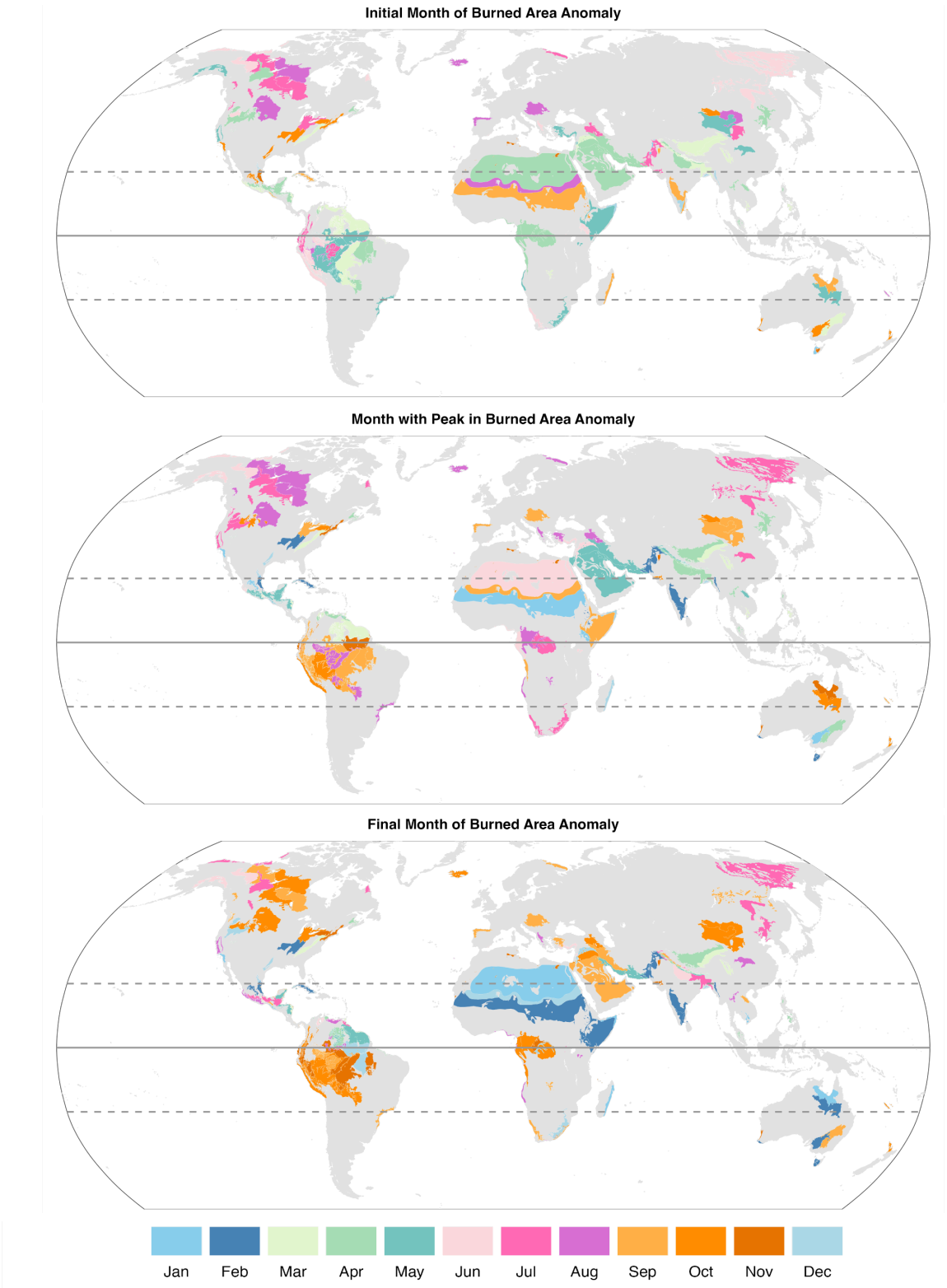

Figure S4: (Top panel) first month, **(middle panel)** peak month, and **(lower panel)** final month of positive BA anomalies at Global Administrative Level 1 during March 2024-February 2025. Peak anomalies are identified relative to the monthly climatology in 2001-2024. The first and final months of the BA anomaly incorporate the period when BA was continuously above the climatological mean. Graduated colours are separated seasonally.

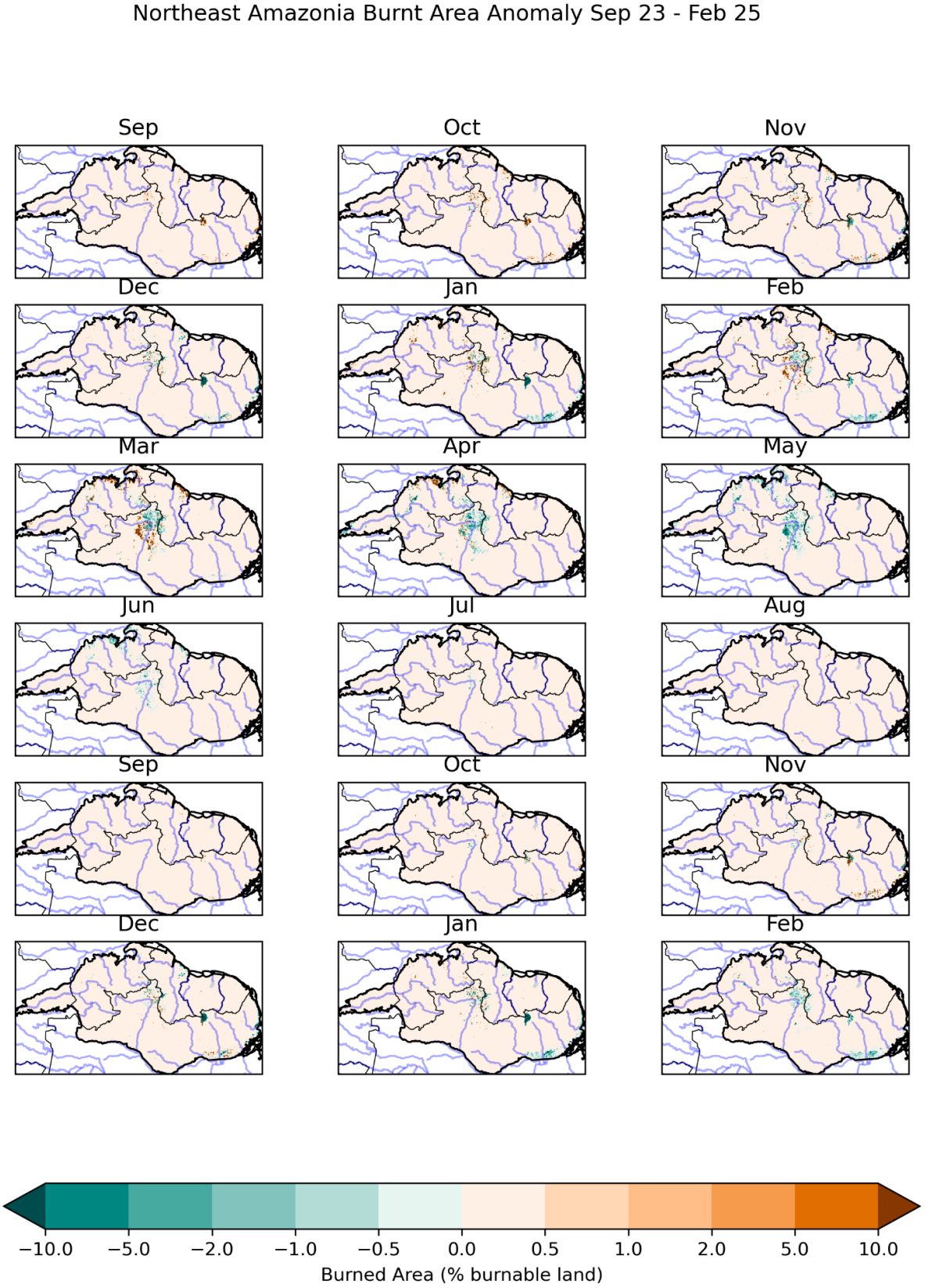

Figure S5: Monthly anomalies in absolute BA fraction (unit: additional % of cell area burned) at 0.25° for Northeast Amazonia throughout the 2024-25 fire season compared with the 2001-2024 climatological mean.

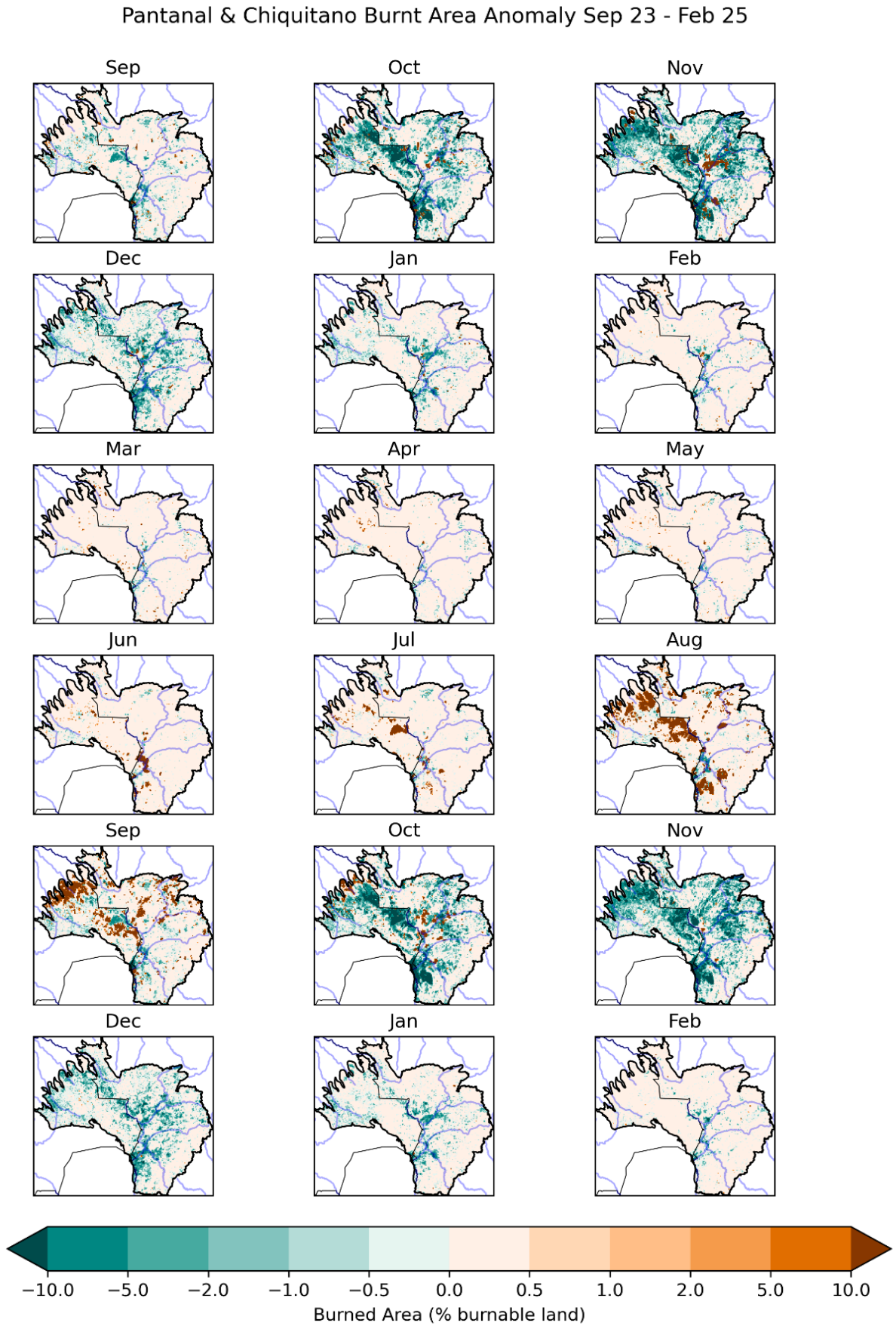

Figure S6: Same as **Figure S5** but for the Pantanal & Chiquitano.

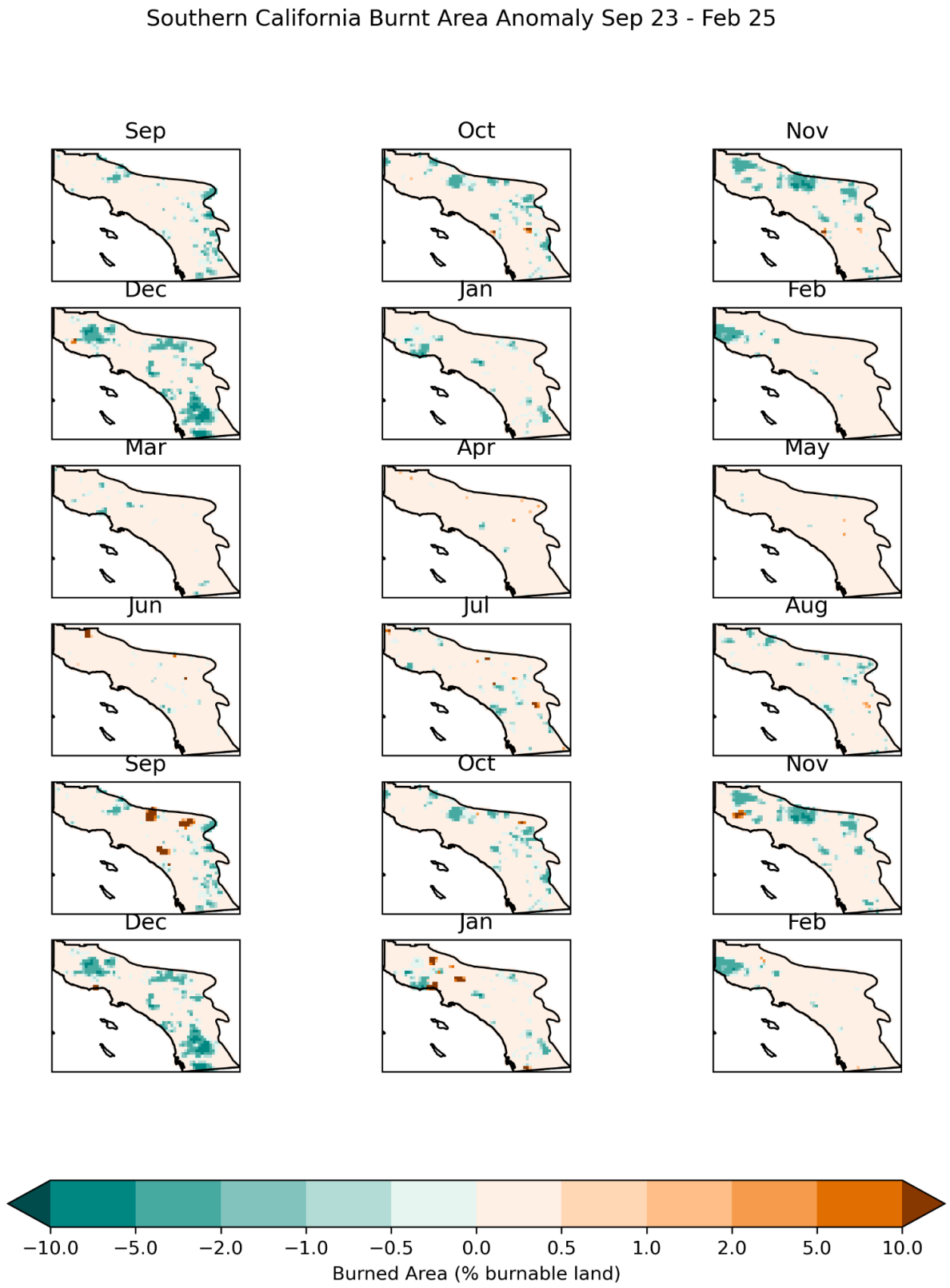

Figure S7: Same as **Figure S5** but for Southern California.

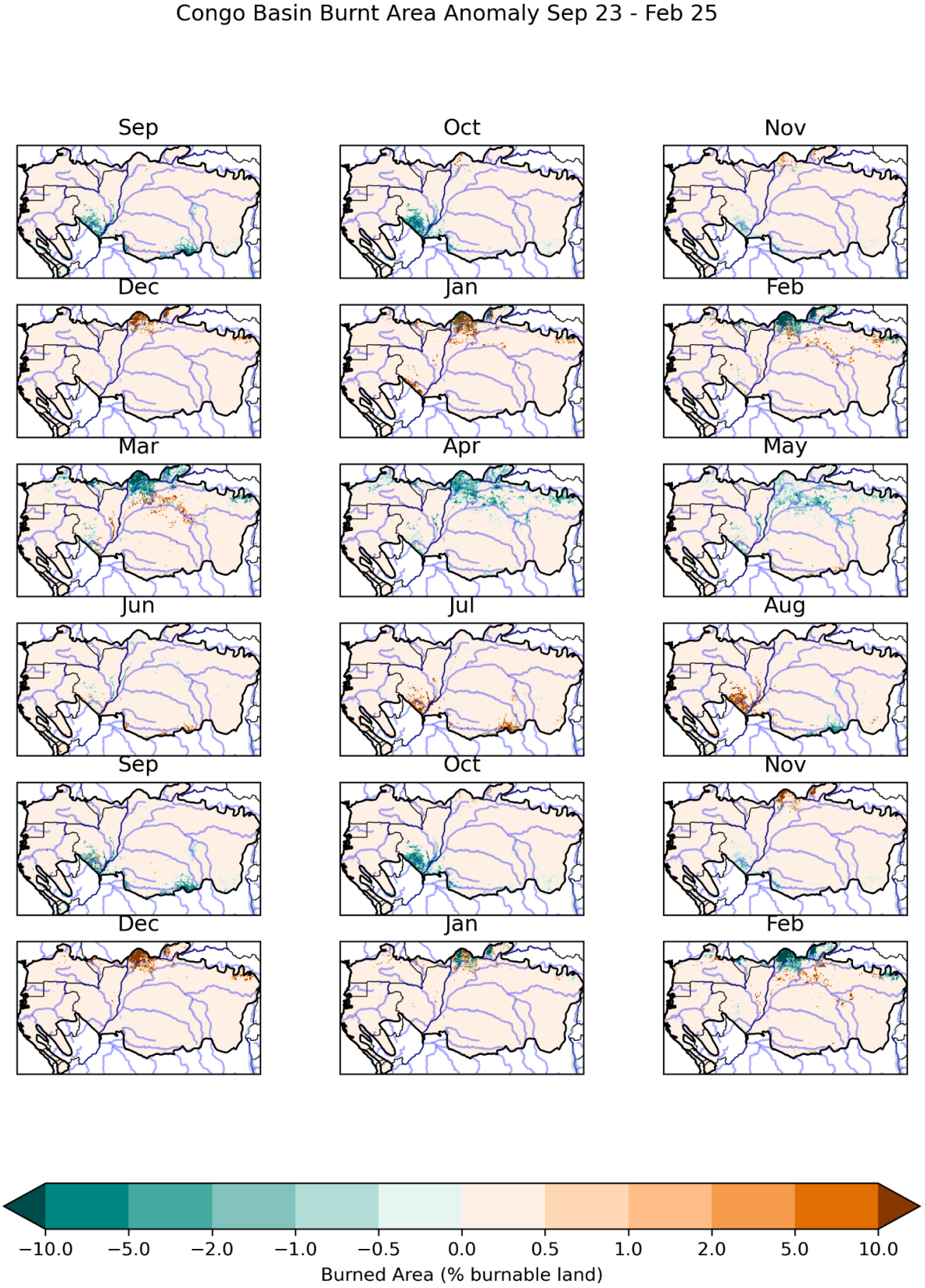

Figure S8: Same as **Figure S5** but for the Congo Basin.

S3 Supplementary Material for Section 3

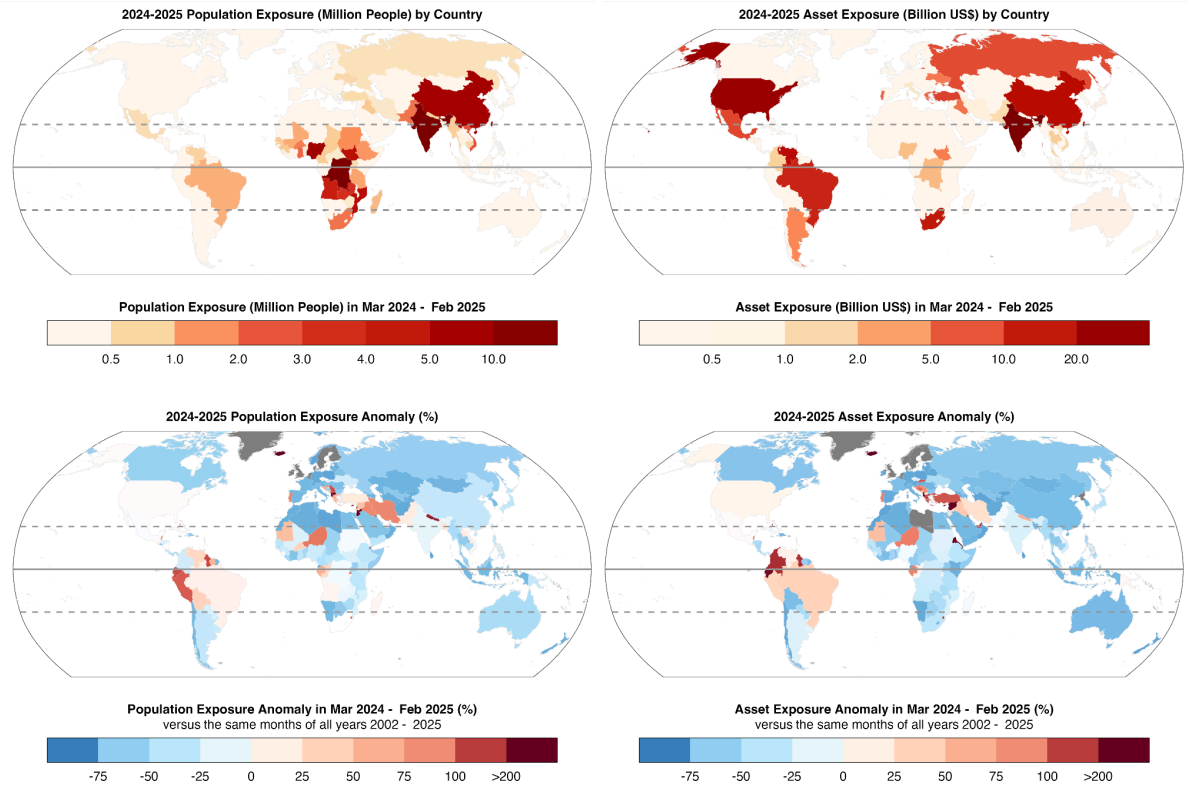

Figure S9: (left panels) Population and **(right panels)** physical assets exposed to burned area (BA) during the 2024-25 global fire season. The figure shows **(top panels)** the number of people or the asset value (billion US$) exposed to fire and **(bottom panels)** the relative anomaly versus all years since 2002.

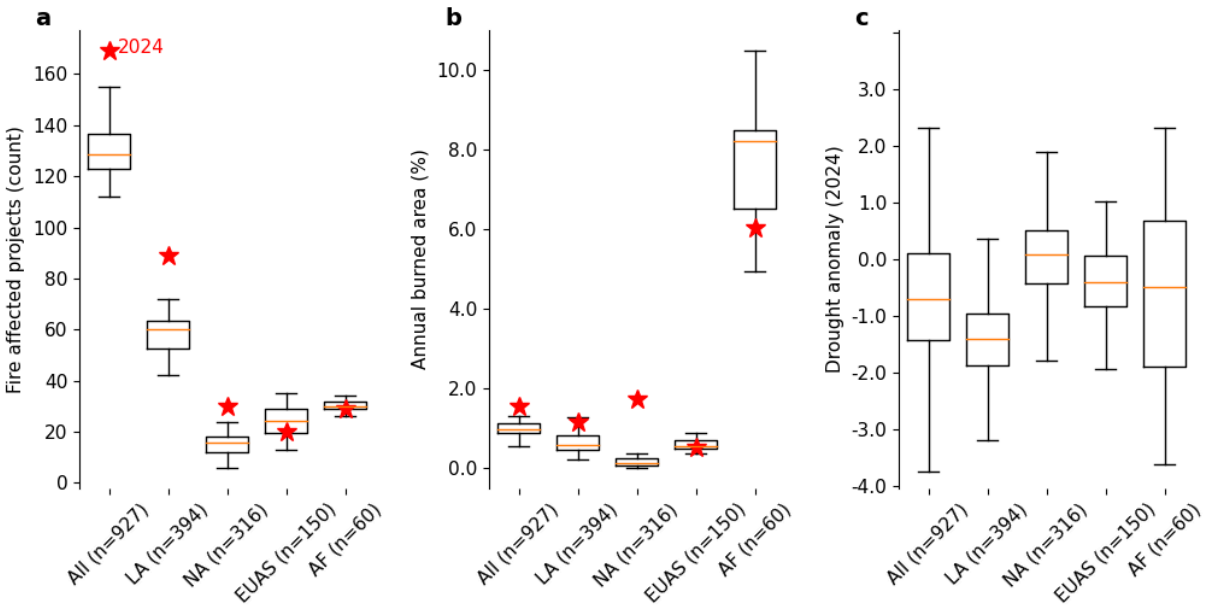

Figure S10: Exceptional 2024 fire activity in carbon projects can be explained by regional drought extremes and a long-term increase in drought and forest fire risk. (a) Number of projects with burned area (BA) in each year, (b) average annual percentage of project area burned, (c) 2024 drought anomaly for all projects (12-month SPEI; negative values indicate drier conditions). In (a) and (b), the red star indicates the 2024 ranking among other years. Data are shown for all projects (all), Latin America (LA), northern America (NA), Eurasia (EUAS), and Africa (AF).

S4 Supplementary Material for Section 4

S4.1 Methods

S4.1.1 Probability of Fire

To model the probability of active fire occurrence at high spatial and temporal resolution, Sparky is trained on daily, gridded observations of satellite-detected active fires from the MCD14ML fire location product, produced by the University of Maryland (Giglio et al., 2020). This dataset contains point-based fire detections from the MODIS instruments aboard the Terra and Aqua satellites. We first aggregated these fire detections onto the model's regular latitude–longitude grid at approximately 9 km resolution, using a daily time step. For each grid cell and day, the target variable was assigned a binary value: 1 if at least one MODIS active fire detection was present in that cell on that day, and 0 otherwise. The model was then trained to predict the probability of observing at least one active fire in a given grid cell on a given day. After training, we applied the model globally to generate daily, grid-based probability maps. While the model outputs the likelihood of at least one fire occurring per grid cell per day, we interpret the sum of predicted probabilities across all grid cells within a domain as an estimate of the expected number of active fire-affected grid cells. This interpretation is consistent with the probabilistic nature of classification outputs in ensemble tree models and is particularly suitable for modelling sparse events such as fire occurrence (Gneiting and Katzfuss, 2014).

S4.1.2 ConFLAME

ConFLAME (Controlar Fogo Local Analise pela Máxima Entropia, or “Local Fire Control Analysis by Maximum Entropy' in English) is a probabilistic, control-based fire model designed to evaluate and attribute burned areas under diverse climate and socio-environmental scenarios. It directly builds upon the established ConFire and FLAME models (Barbosa et al., 2025; Kelley et al., 2019, 2021), integrating ConFire’s control-structured approach with FLAME's Bayesian inference framework based on the Maximum Entropy principle. Full details can be found in Barbosa et al. (submitted). ConFLAME is specifically developed for attribution purposes, including compatibility with satellite-derived burned area data. This hybrid model allows for spatially explicit, event-scale attribution, making it applicable across different timeframes and regions. This means that, new to this year's report, our burned area (BA) driver and attribution assessments can now target both high burned area zones within subregions and the overall burned area across our entire focal region.

ConFLAME simulates monthly fractional burned area at grid-cell level using a set of environmental and anthropogenic *controls*, each representing a key dimension of fire regulation. These controls capture the limitations imposed by factors such as:

- Fuel availability and continuity
- Fuel dryness
- Fire weather (including temperature and relative humidity)
- Wind speed
- Ignition sources (both natural and human-caused)
- Fragmentation and suppression (e.g., from land use, roads, or firefighting)
- Stochastic influences (unmodelled or residual variation)

Each control predicts the maximum possible burned area under ideal conditions for that specific factor. For instance, the “fuel dryness” control estimates the area that *could* burn if all other factors, such as fuel, ignition or suppression, impose no limitations. These controls are derived as linear combinations of their respective drivers (see Table S1 for assignment details**)**, which are then transformed using the logistic function to produce a value between 0 and 1. The individual control outputs are multiplied together to give a final burned area estimate, capturing the combined effects of all constraints (Kelley et al., 2021). This multiplicative structure allows interactions between drivers to influence fire outcomes and accommodates compound extremes where multiple drivers align to produce extreme BAs. As per Barbosa et al. (2025), this BA is corrected for sub-grid spatial/temporal autocorrelation that may alter overall fire spread and therefore BA.

ConFLAME uses a Bayesian inference approach following a similar protocol to (Barbosa, 2024). We use the PyMC (v5) Python package with the Metropolis-Hastings MCMC sampler (Hoffman and Gelman, 2011). Optimisation runs over 10 parallel chains with 1,000 tuning and 1,000 sampling iterations per chain to determine the probability distribution of model parameters, such as those describing driver combination control strength and BA autocorrelation. The model employs a Maximum Entropy update function to avoid unnecessary assumptions beyond data constraints (Barbosa et al., 2025). Training utilising 50% of the data or a minimum of 4000 grid cells. Instead of a single outcome. This approach

produces a full distribution of possible burned area results for each grid cell and month, capturing uncertainty in parameters and fire variability. This allows rare but plausible outcomes, such as unusual BA levels, to emerge when multiple conditions favour fire.

Once trained, ConFLAME is run in large ensembles to approximate the posterior BA probability distributions:

- For attribution experiments (e.g., climate vs human vs combined forcing), we randomly sample 400 simulations from each chain (so 4000 samples), each using parameter samples drawn from the posterior distribution. For climate or human attribution, we pair each of these with an additional sample using counterfactual (either without anthropogenic forcing, without climate change or without people) inputs.

- For future projections, a smaller ensemble of 1000 sampled (100 for each chain)..

- As per (Barbosa, 2024), for evaluation we trained the first half of the period and test on the second half using 1000 samples. For the rest of the results, we trained on the full period.

Each simulation in the ensemble represents one possible realisation of fire behaviour, conditioned on a plausible combination of parameters and driver inputs. The ensemble as a whole approximates the posterior distribution of burned area for each grid cell and time step.

When analysing outputs across time (e.g., seasonal totals) or space (e.g., regional aggregates), probability metrics (mean, median, percentiles) are computed per ensemble member first, and then the distribution of these metrics is used to reconstruct a consistent posterior for the aggregated quantity. This preserves the dependencies within each realisation and avoids artificial narrowing of uncertainty that would result from averaging across distributions rather than ensembles.

Table S1: Overview of predictors used in the two fire attribution models (PoF and ConFLAME). Predictors are grouped into four control categories. ✓ indicates inclusion in the model, with (+) or (–) signs representing positive or negative influence over fire occurrence in ConFLAME. Resolution and temporal coverage refer to the dataset version used during model training.

Category	Predictor	PoF	Con-FLAME (section 4)	Con-FLAME (section 5)	Spatial Resolution	Temporal Coverage	Reference
Weather	2m Temperature	✓	✓ (+)	✓ (+)	~9 km (0.1°)	2003–2025	(Muñoz-Sabater et al., 2021)
	2m Dewpoint Temperature	✓	✓ (–)	✗	~9 km (0.1°)	2003–2025	(Muñoz-Sabater et al., 2021)
	Relative Humidity	✗	✗	✓ (–)	(0.25°)	2003–2025	(Muñoz-Sabater et al., 2021)
	10m Wind Speed	✓	✓ (+)	✓ (+)	~9 km (0.1°)	2003–2025	(Muñoz-Sabater et al., 2021)
	Precipitation	✓	✓ (–)	✓ (–)	~9 km (0.1°)	2003–2025	(Muñoz-Sabater et al., 2021)
Fuel	Live Leaf Fuel Load	✓	✓ (+)	✓ (+)	~9 km (0.1°)	2003–2025	(McNorton and Di Giuseppe, 2024)
	Live Wood Fuel Load	✓	✓ (+)	✓ (+)	~9 km (0.1°)	2003–2025	(McNorton and Di Giuseppe, 2024)
	Dead Foliage Fuel Load	✓	✓ (+)	✓ (+)	~9 km (0.1°)	2003–2025	(McNorton and Di Giuseppe, 2024)
	Dead Wood Fuel Load	✓	✓ (+)	✓ (+)	~9 km (0.1°)	2003–2025	(McNorton and Di Giuseppe, 2024)
	LAI – Low/High Vegetation	✓	✓ (+)	✓ (+)	~9 km (0.1°)	2003–2025	(Boussetta et al., 2021)
	Live Fuel Moisture Content	✓	✓ (–)	✗	~9 km (0.1°)	2003–2025	(McNorton and Di Giuseppe, 2024)
	Dead Foliage Moisture Content	✓	✓ (–)	✗	~9 km (0.1°)	2003–2025	(McNorton and Di Giuseppe, 2024)
	Dead Wood Moisture Content	✓	✓ (–)	✗	~9 km (0.1°)	2003–2025	(McNorton and Di Giuseppe, 2024)

Ignition/ Suppresion	Pasture Fraction	✗	✓ (+/–)	✓ (+/–)	~25 km (0.25°)	2007–2025	(Klein Goldewijk et al., 2010)
	Cropland Fraction	✗	✓ (+/–)	✓ (+/–)	~25 km (0.25°)	2007–2025	(Klein Goldewijk et al., 2010)
	Urban Population	✗	✓ (+/–)	✓ (+/–)	~25 km (0.25°)	2007–2025	(Klein Goldewijk et al., 2010)
	Rural Population	✗	✓ (+/–)	✓ (+/–)	~25 km (0.25°)	2007–2025	(Klein Goldewijk et al., 2010)
	Population Density	✓	✗	✗	~9 km (0.1°)	2005, 2010, 2015, 2020	(Center for International Earth Science Information Network (CIESIN), 2025)
	Road Length	✓	✗	✗	~9 km (0.1°)	2015	(Meijer et al., 2018)
	Cloud-to-ground lightning	✗	✓ (+)	✓ (+)	~25 km (0.25°)	2019-2025	(Qu et al., 2025)
	Lightning	✓	✗	✗	~9 km (0.1°)	2019-2025	(Lopez, 2016)
	Vegetation Type	✓	✗	✗	~9 km (0.1°)	2003-2021	(Boussetta et al., 2021)
	Urban Fraction	✓	✗	✗	~9 km (0.1°)	2010	(McNorton et al., 2023)
	Orography	✓	✗	✗	~9 km (0.1°)	Static	(Boussetta et al., 2021)
Missed Prediction Term		✓	✓	✓	Model-defined	2007–2025	(Barbosa et al., 2025) This study

S4.2 Results

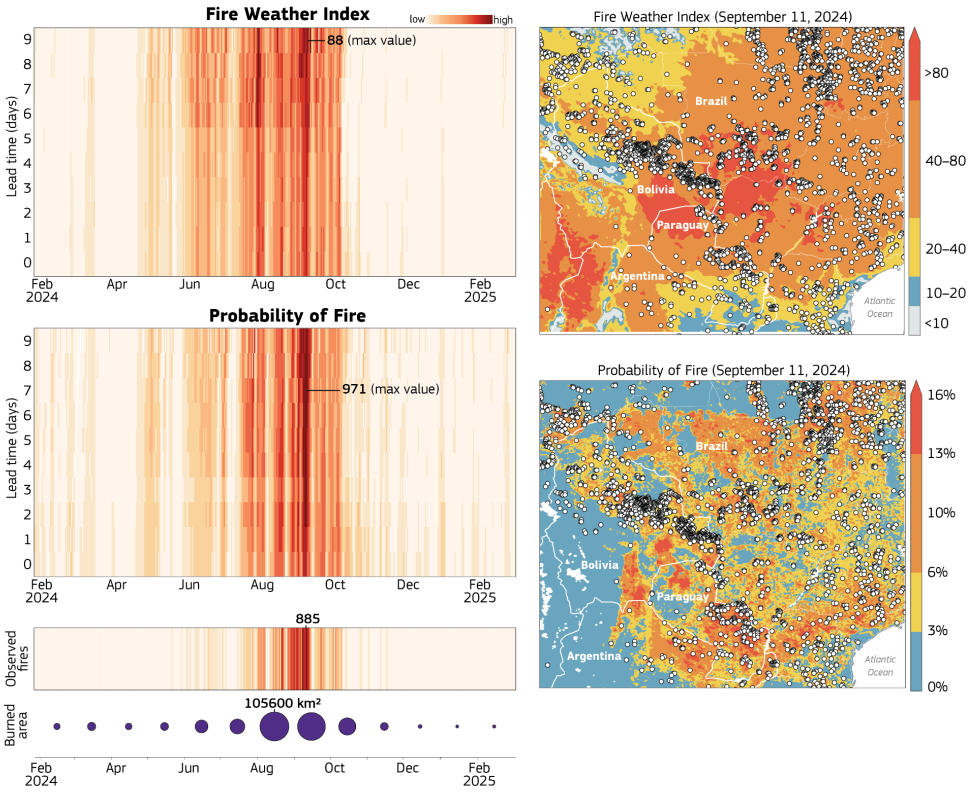

Figure S11: Pantanal and Chiquitano fire forecast (as for **Figure 8 in the main text**). Chicklet plots displaying seamless FWI and POF fire predictions over 10 days forecast. The x-axis corresponds to specific dates throughout the year, while the y-axis denotes either observations or the time leading up to the date when a forecast was generated. The vertical colour coherence allows for quick identification of the time windows of predictability associated to the observed fire activity both provided in terms of number of detected active in a day fires and total BA in a month (circles). The maps represents a snapshot in time at day 0 to allow the comparison of the spatial distribution of the forecasts and the recorded fire activity by MODIS.

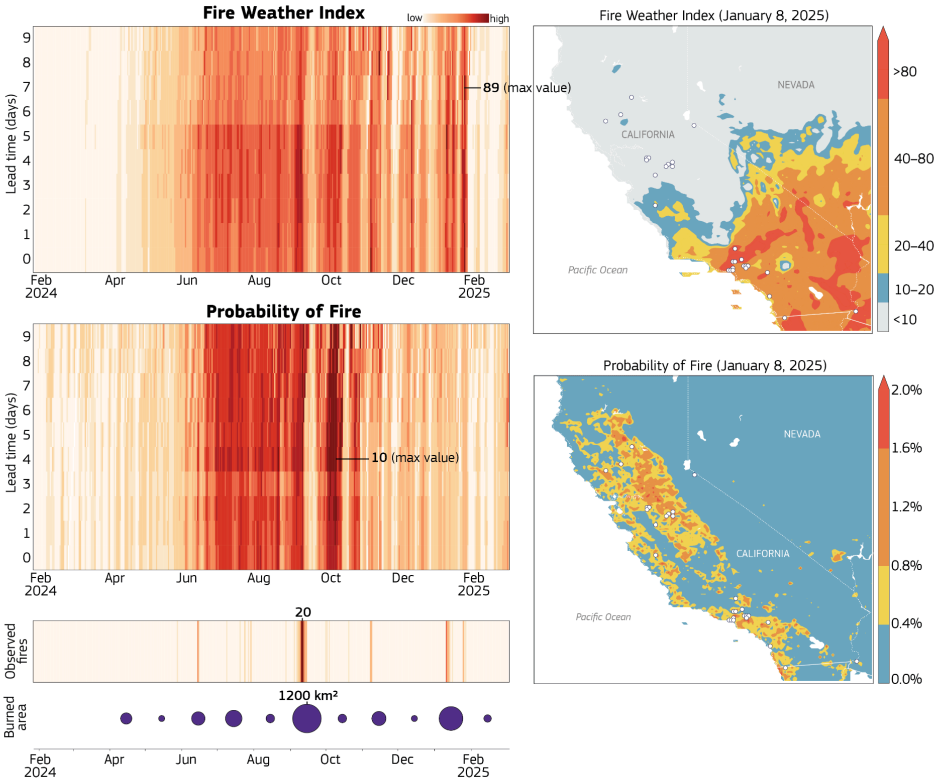

Figure S12: Southern California fire forecast (as for Figure 8 in the main text). Chicklet plots displaying seamless FWI and POF fire predictions over 10 days forecast. The x-axis corresponds to specific dates throughout the year, while the y-axis denotes either observations or the time leading up to the date when a forecast was generated. The vertical colour coherence allows for quick identification of the time windows of predictability associated to the observed fire activity both provided in terms of number of detected active in a day fires and total BA in a month (circles). The maps represents a snapshot in time at day 0 to allow the comparison of the spatial distribution of the forecasts and the recorded fire activity by MODIS.

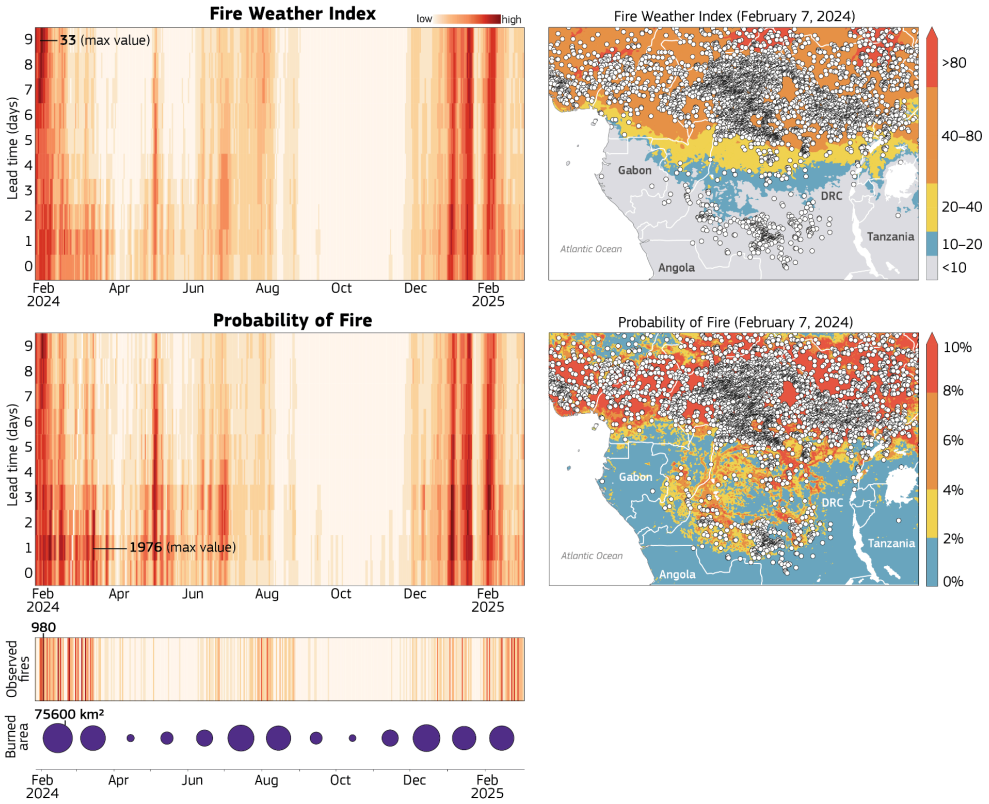

Figure S13: Congo basin fire forecast (as for **Figure 8 in the main text**). Chicklet plots displaying seamless FWI and POF fire predictions over 10 days forecast. The x-axis corresponds to specific dates throughout the year, while the y-axis denotes either observations or the time leading up to the date when a forecast was generated. The vertical colour coherence allows for quick identification of the time windows of predictability associated to the observed fire activity both provided in terms of number of detected active in a day fires and total BA in a month (circles). The maps represents a snapshot in time at day 0 to allow the comparison of the spatial distribution of the forecasts and the recorded fire activity by MODIS.

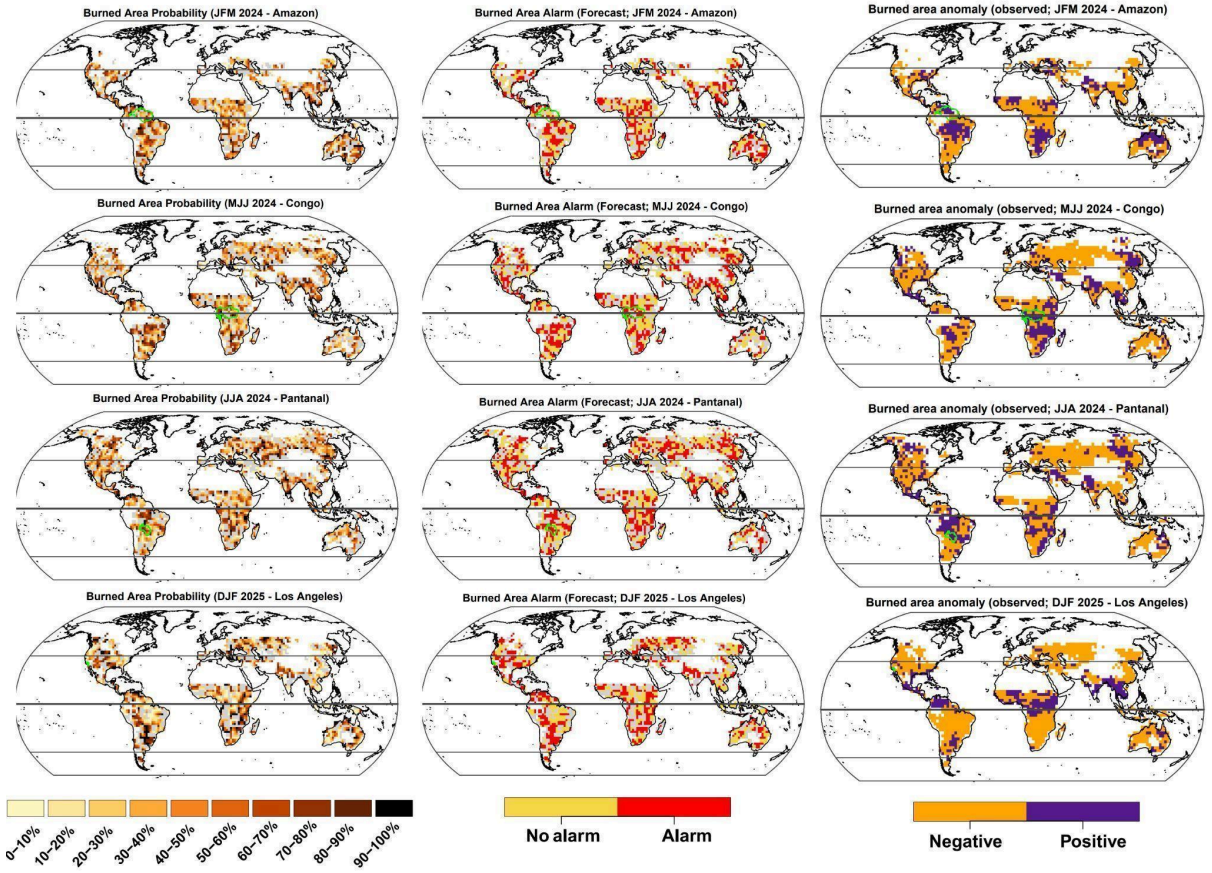

Figure S14. Forecast and observed burned-area anomalies for four seasons: JFM, MJJ and JJA in 2024, and DJF in 2025. Rows correspond to these seasons and are linked respectively to the case-study regions Amazonia, Congo, Pantanal and Los Angeles (highlighted in green). The columns display (i) the probability of a burned-area anomaly occurring (left), (ii) whether the early-warning system was triggered (centre), and (iii) the anomaly that was actually observed (right). Grey shading marks grid points where the climate-fire model is not statistically significant (p-value ≥ 0.01), while white indicates points where seasonal burned area was zero in less than half of the study period (i.e. BA = 0 in fewer than 11 of the 22 years, 2002–2023; see (i.e. BA = 0 in fewer than 11 of the 22 years, 2002–2023; see Torres-Vázquez et al., 2025).

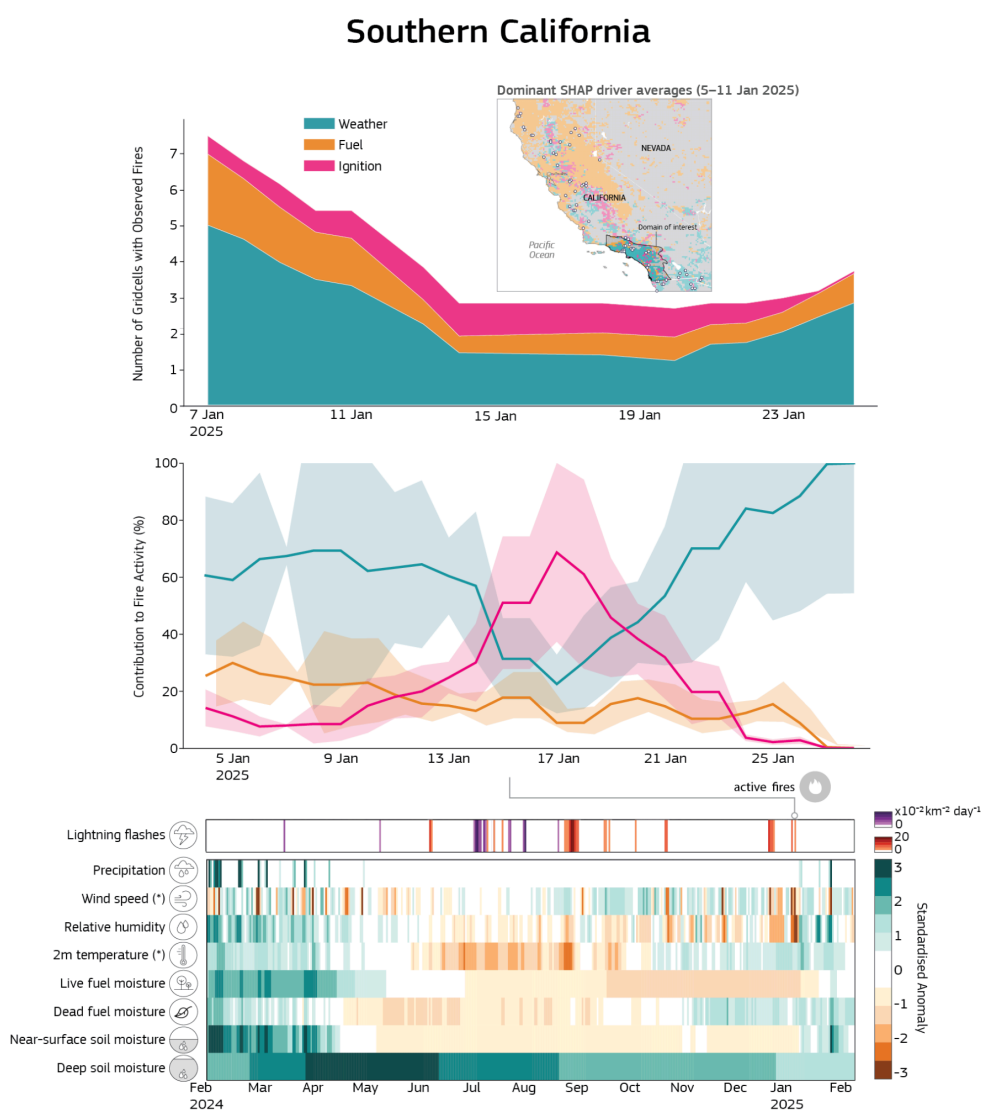

Figure S15: Drivers explaining fire hotspots in Southern California (as for **Figure 10 in the main text**).

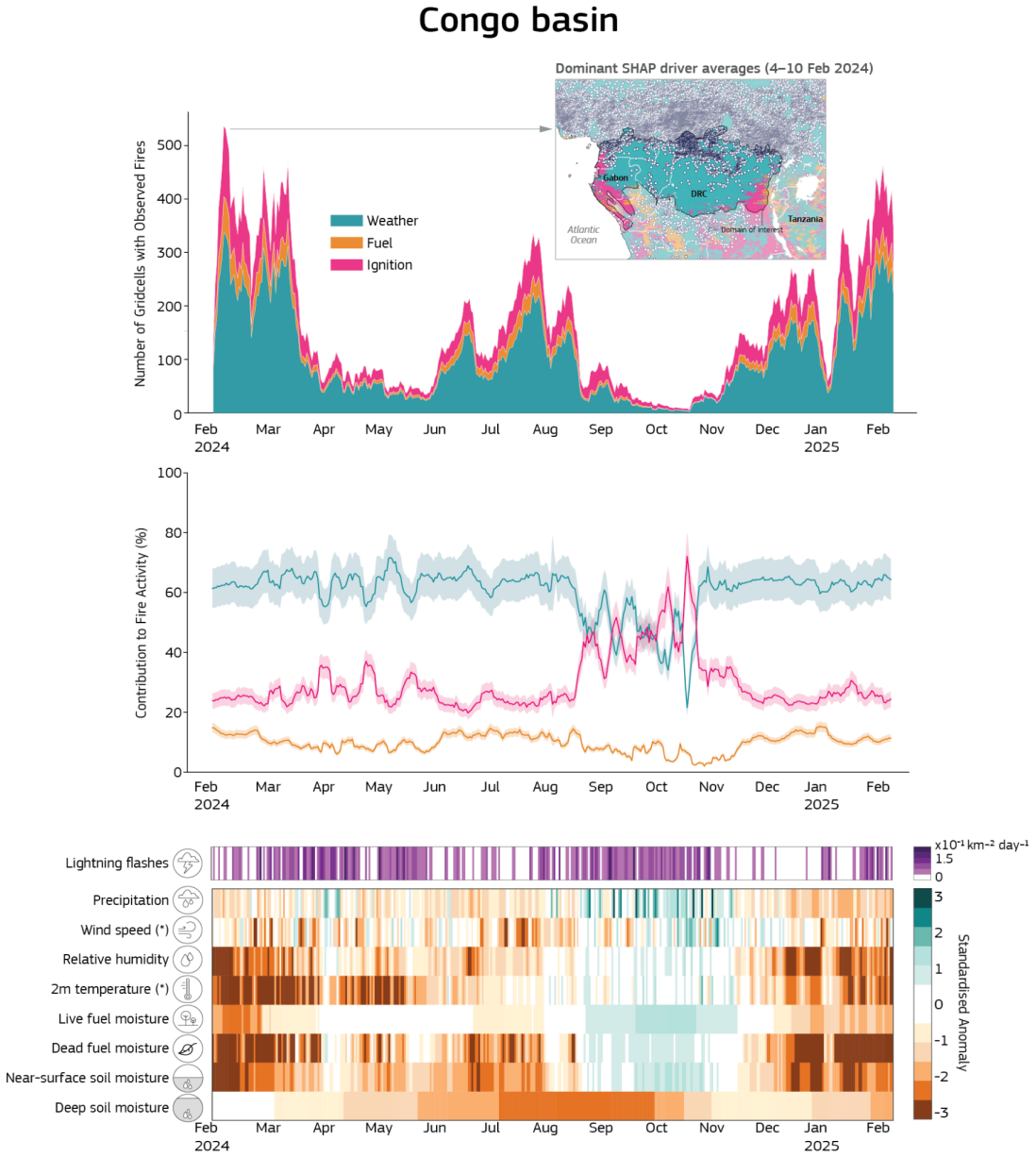

Figure S16: Drivers explaining fire hotspots in the Congo basin (as for **Figure 10 in the main text**).

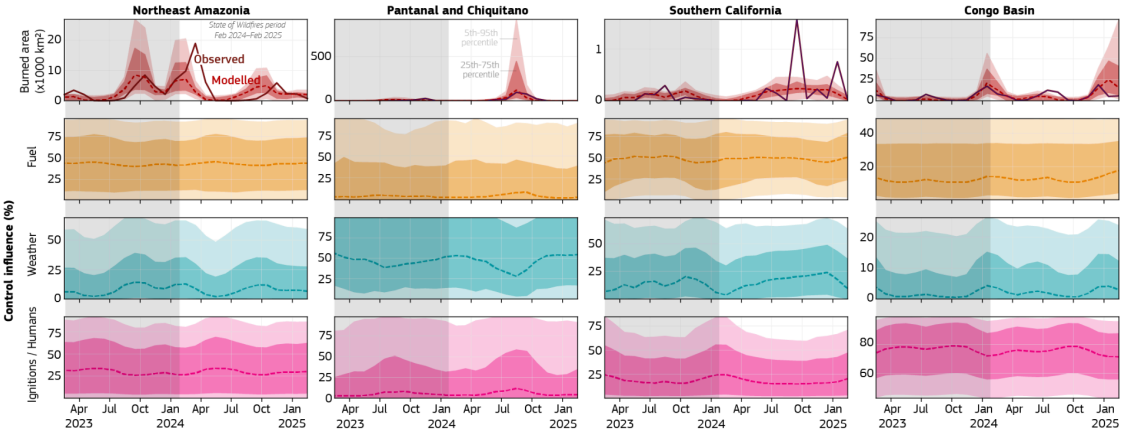

Figure S17. Time series of burned area and key fire drivers for each focus region during 2024. Columns represent different regions; rows show different variables. Top row: Observed burned area (blue) and modelled burned area (red) for each region, with the model median (solid red line), interquartile range (shaded), and 5th–95th percentile range (lighter shading). Second to fourth rows: Modelled contributions from key fire drivers—fuel availability, fire weather, and human/ignition-related factors—with each showing median (solid line), interquartile range (shaded), and 5th–95th percentile range. Together, these panels illustrate the relative influence of climate and human factors on fire activity throughout the year.

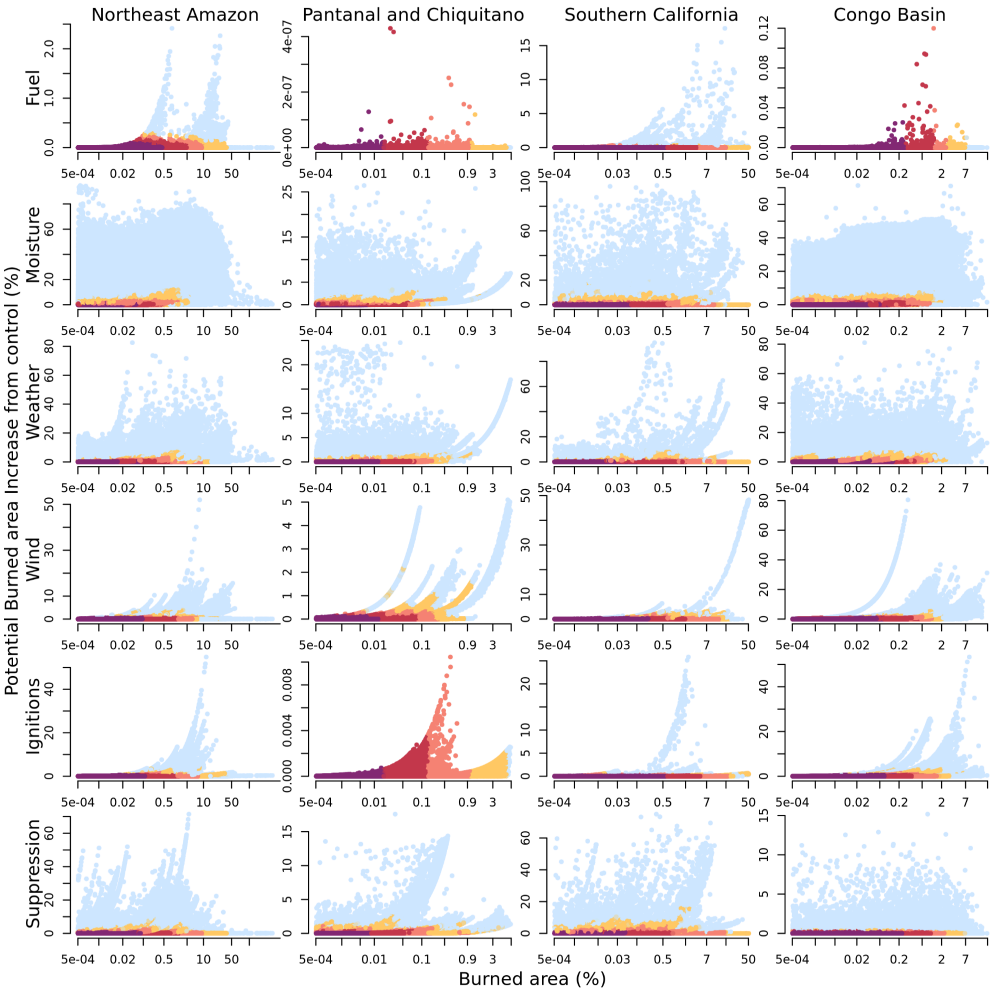

Figure S18. Potential increases in burned area (y-axis) under different fire-controlling factors across varying levels of simulated burned area (x-axis), shown separately by region (columns) and control factor (rows). Results are drawn from the full 5000-member ConFLAME ensemble. Shading indicates the density of grid cells where a given potential increase occurs, with darker areas representing higher density. Each control factor represents a specific constraint on fire activity:

- Fuel: the difference between BA simulated under plentiful fuel loads versus actual fuel loads.
- Moisture: the effect of fuel moisture, comparing perfectly dry to actual moisture conditions.
- Weather: the influence of atmospheric conditions, comparing the most extreme simulated fire weather to observed conditions.
- Wind: the increase in BA expected under maximum wind conditions versus actual winds.
- Ignitions: the difference between saturated ignitions (i.e., unlimited human or natural ignition sources) and observed ignition patterns.
- Suppression: the difference between scenarios with no fire suppression and those reflecting actual suppression efforts.

Together, these estimates illustrate the latent potential for fire spread under different limiting factors, helping to disentangle which constraints most strongly regulate fire activity in each region and at different severity levels.

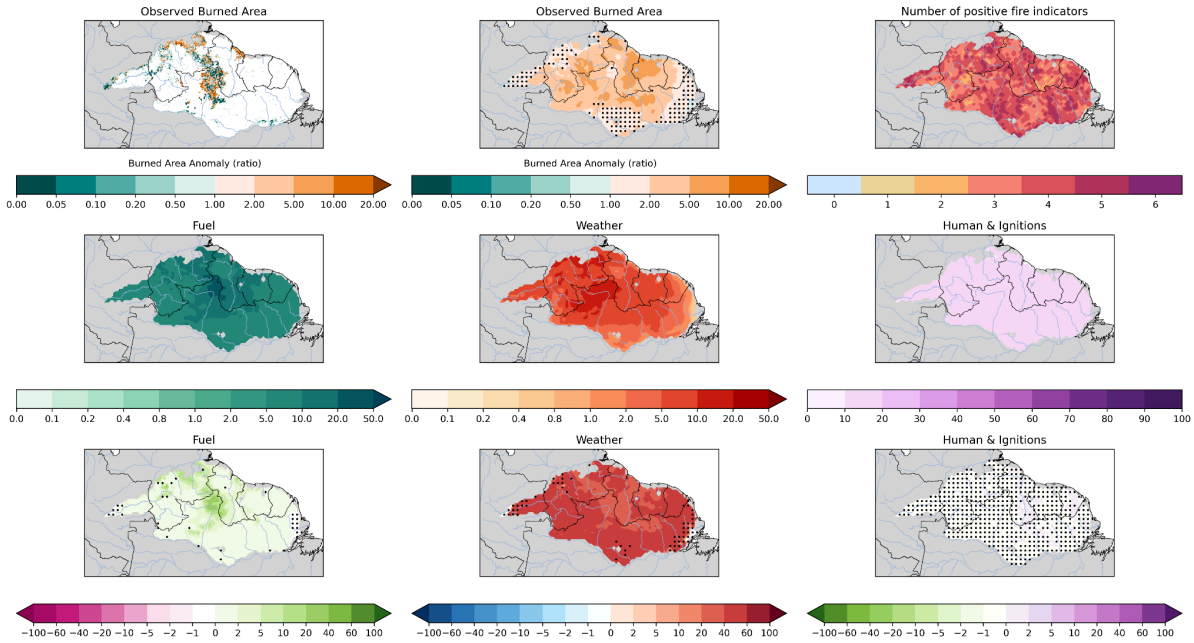

Figure S19 Spatial distribution of burned area and fire driver anomalies for January-March 2024 in Northeastern Amazonia. Top row: Observed burned area anomalies from MCD64A1 (left); ensemble mean burned area anomalies simulated by ConFLAME (middle); and the number of fire-relevant controls (out of seven) showing a positive anomaly during the same period (right). Second row: Mean simulated control strength for each of the three grouped controls, expressed using the "standard limitation" formulation (Kelley et al., 2019), indicating the degree to which each factor constrained or enabled burning. Bottom row: Anomalies in control strength compared to the modelled climatology. Values represent ensemble means across all 4,000 members. Dots on the anomaly maps indicate grid cells with low agreement across ensemble members (<95% agreement in the direction of change), reflecting lower confidence in the sign of the anomaly at those locations.

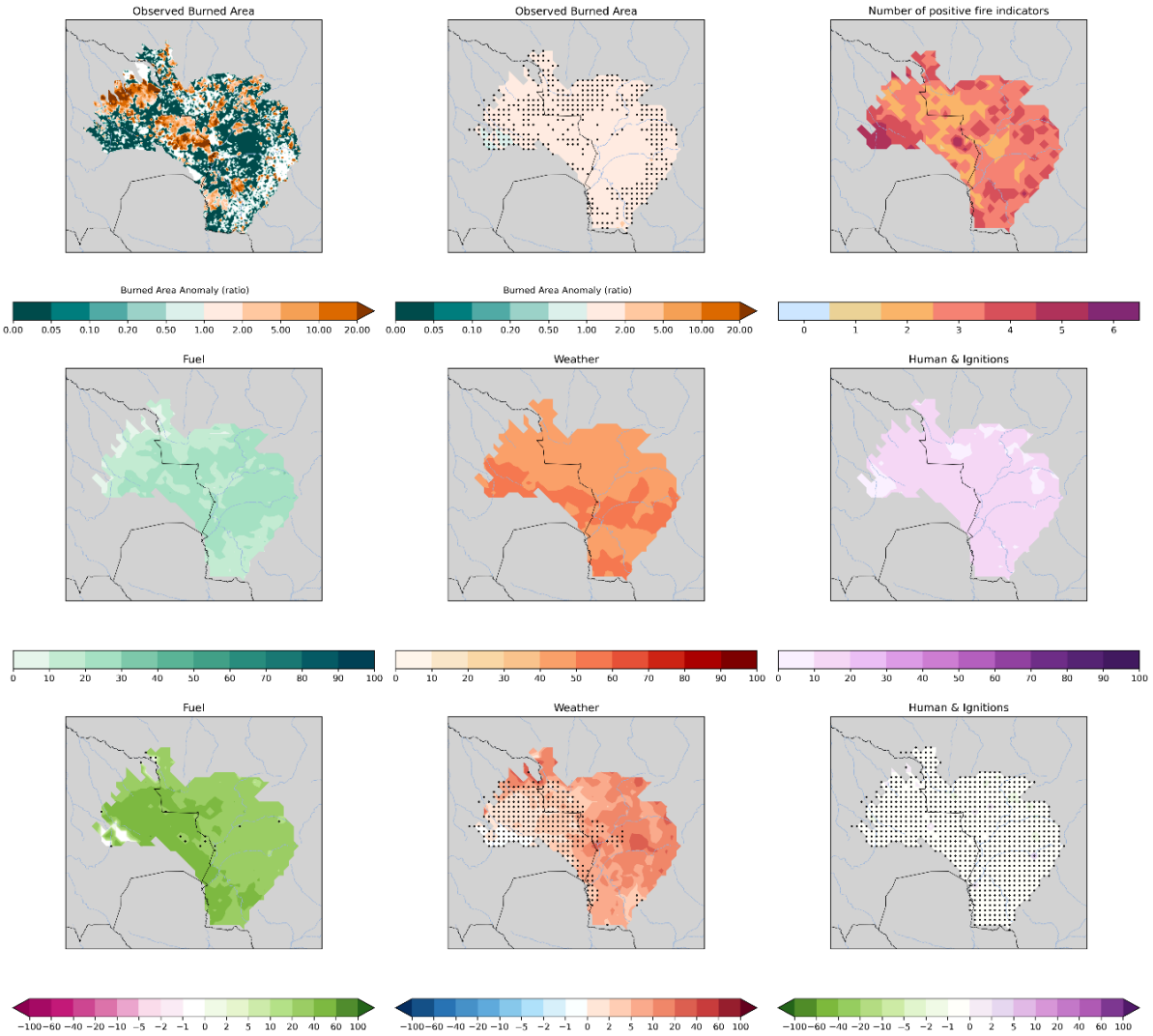

Figure S20 As Figure S19 but for Pantanal & Chiquitano, August and September 2024

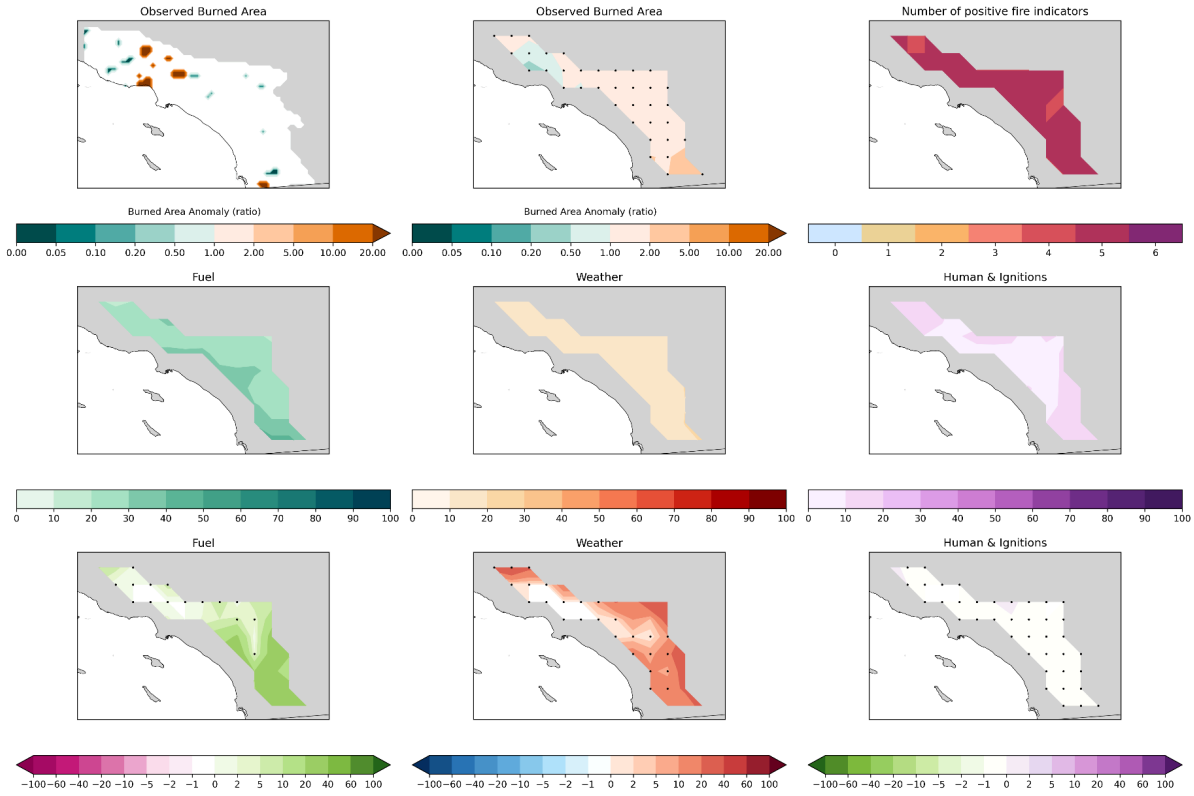

Figure S21 As Figure S19 but for Southern California, January 2025.

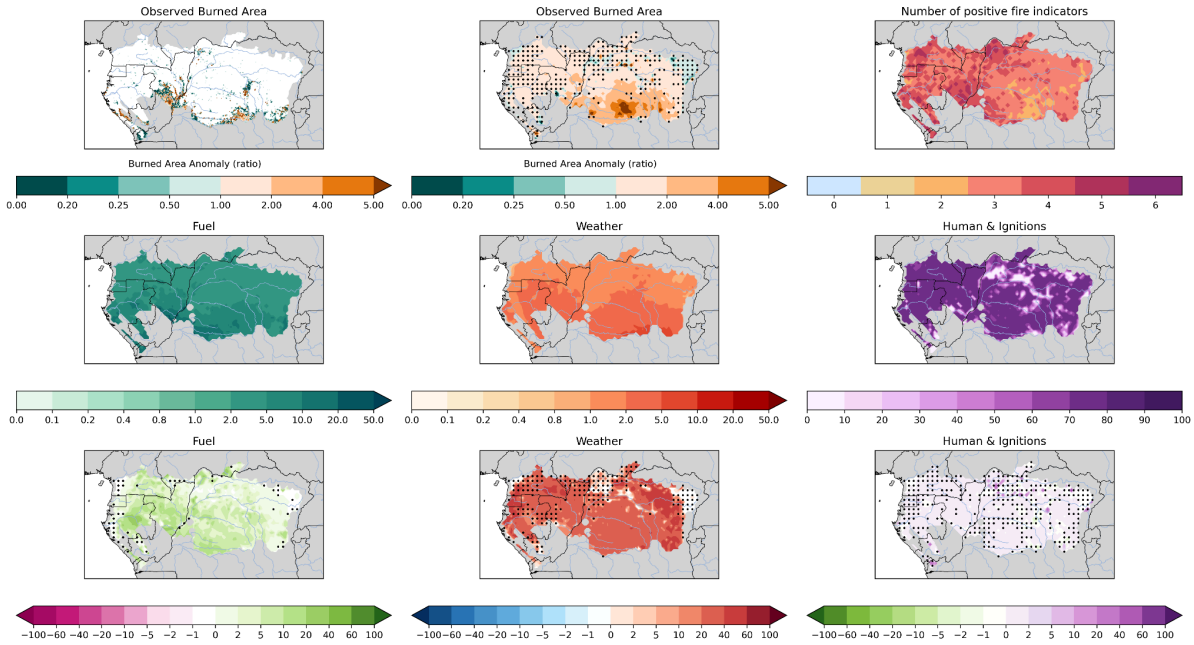

Figure S22 As Figure S4.9 but for Congo Basin, July and August 2024

S5 Supplementary Material for Section 5

S5.1 Methods

Table S2: Guide to different attribution comparisons discussed. Coloured boxes indicate what is accounted for in counterfactual comparisons, which variable is targeted or where we look directly as the event or a longer historic record.

Attribution type	Model	**Factual** vs *counterfactual* data sources	Removed in Counterfactual						Target variable			Target period	
			GHG emissions on climate	Aerosols on climate	Land use on climate	Climate & CO_2 on fuel	Natural climate trends	Humans on fire	Event FWI	Event BA	Background BA	During the event	Historic
Anthropogenic climate Forcing	Canadian FWI	HaDGEM3-A **All** vs *NAT*											
	CanESM5 FWI	*CanESM5* ***2014-2025*** *vs 1850–1859*											
	WWA - sourced from already published material												
	ConFLAME NRT	**ERA5** vs *merged ERA5/HadGEM3-A*											
Total climate forcing	ConFLAME ISIMIP	ISIMIP3a GSWP3 **reanalysis** vs *detrended*											
	FireMIP												
Socio-economic factors	ConFLAME ISIMIP	ISIMIP3a GSWP3 detrended **2003-2019** vs *1901-1917*											
	FireMIP												
All forcings	ConFLAME ISIMIP	ISIMIP3a GSWP3 **reanalysis 2003-2019** vs *detrended 1901-1917*											
	FireMIP												

S5.1.1 Attributing Extremes in Fire Weather during 2024-25 - extended

We applied a bias correction to the 2023 HadGEM3 large ensemble using a linear regression approach, based on comparisons between the model's historical simulations (1960–2013) and the ERA5 reanalysis of fire weather index (FWI). The FWI data were transformed prior to regression to stabilise values at the high end, ensuring extreme fire conditions were accurately captured without distorting the distribution. This correction was anchored to 2023 conditions by extrapolating trends from the historical period to account for recent warming.

Each present-day ensemble member was corrected against all historical ensemble members, producing a large ensemble of bias-adjusted simulations (7875 members in total). This method avoids assumptions about pairwise matching of ensemble members due to the perturbation process used in generating the ensemble.

We then calculated risk ratios (RRs) for extreme fire weather events by comparing the likelihood of exceeding the observed 2023 FWI threshold in the bias-corrected “ALL” (with climate change) and “NAT” (without climate change) simulations. The RR represents how much more likely the event was in today’s climate compared to a world without anthropogenic influence. Uncertainty was assessed using bootstrapping.

Full technical details are provided in last years report supplement section S1.2.3 (Jones et al. 2024b) and Burton et al. (2025).

S5.1.2 Background changes in fire weather this decade

To complement the HadGEM large-ensemble weather simulations, we also use a fully coupled Earth system model approach to assess the changing probability of extreme fire weather events. This method uses the Canadian Earth System Model version 5 (CanESM5 Swart et al., 2019), developed for the sixth phase of Coupled Model Intercomparison Project (CMIP6; Eyring et al., 2016). CanESM5 provides a 50-member ensemble spanning both the historical period (1850–2014) and high-emission future projections (SSP585, through 2100). By drawing on a physically consistent climate model ensemble, this method offers an independent line of evidence for assessing the role of anthropogenic climate change. Unlike the weather-perturbation ensemble, this method evaluates how often events of similar magnitude to those in 2024/25 would have occurred between 2016-2025.

For each focal region and season, we extract the annual maximum of 7-day average FWI for each ensemble member and apply a statistical model (a time-dependent Generalized Extreme Value distribution), as often used in previous attribution studies (Eden et al., 2016, 2018; Krikken et al., 2021; Liu et al., 2022a, 2023, 2022b; Otto et al., 2018; e.g. Schaller et al., 2014; van der Wiel et al., 2017) to estimate how the probability of extreme fire-conducive conditions has changed over time. In this section, we compare the likelihood of these events under pre-industrial conditions (1850–1859) to their likelihood in the recent past (2016–2025). These comparisons are expressed as a **probability ratio (PR)**. For example, a PR of 10 indicates a tenfold increase in the chance of such an event occurring in the modern climate compared to pre-industrial conditions. In this study, we define 'high fire weather' conditions as the percentile rank of extreme Fire Weather Index (FWI) values during the event period, calculated relative to the full ERA5 historical record. For instance, if the event corresponds to the 95th percentile in the observed record, we assign the 95th percentile value from the model simulations as the representative magnitude of the event within the simulations. Confidence intervals for these PRs are estimated using bootstrapping. This approach, again following a similar approach outlined by (Liu et al.,

2022c), allows us to account for uncertainties arising from internal climate variability and limited sample sizes, while leveraging the strength of large ensemble simulations.

While this approach relies on a more generalised representation of climate and fire-relevant processes — and applies a statistical fit to account for sample size limitations — it adds valuable robustness by providing attribution results from an independent model and that assesses FWI occurrence over a longer period. Together with the HanGEM3-A approach, this approach strengthens confidence in the conclusions drawn by offering a diverse and independent line of evidence for the role of climate change in recent fire weather extremes.

S5.1.2.1 Model and Data

We use the Canadian Fire Weather Index (FWI; van Wagner, 1987) calculated from daily ERA5 reanalysis data for 1951–2025, and from the CanESM5 large ensemble simulations for 1850–2100 (Swart et al., 2019). The CanESM5 model was selected due to the availability of a 50-member ensemble under the historical (1850–2014) and SSP5-8.5 scenario (2015–2100), providing sufficient sample size for extreme value analysis.

S5.1.2.2 Statistical Framework

We follow a time-dependent Generalized Extreme Value (GEV) approach (Eden et al., 2016; Liu et al., 2022a, b; Philip et al., 2020; van der Wiel et al., 2017). For each focal region and fire season, we calculate annual maxima of 7-day average FWI from each ensemble member and fit them to a GEV distribution.

The location (μ) and scale (σ) parameters are modelled as linear functions of 4-year smoothed global mean surface temperature (GMST) from the ensemble mean, capturing the externally forced response. The shape parameter (ξ) and the σ/μ ratio are held constant. This yields a time-evolving distribution from which return periods (and hence probabilities) for a fixed event magnitude can be computed across different climate baselines.

S5.1.2.3 Attribution

For attribution, we evaluate the return period of a specific observed 2024 event magnitude (e.g., 7-day FWI max) in:

- A pre-industrial baseline: 1850–1859
- A recent baseline: 2015–2024

We then use the Risk Ratio in **S5.1.1**.

5.1.2.4 Uncertainty

We estimate 90% confidence intervals using a non-parametric moving-block bootstrap with 1,000 replicates (Efron and Tibshirani, 1998; van der Wiel et al., 2017). This preserves autocorrelation in annual maxima sequences and accounts for interannual variability across the ensemble.

5.1.3 Attributing Region-wide Extreme BA during 2024-25 - extended

The near real-time configurations test and training follows the same setup as described in **Section 4**, but excludes the fuel moisture variables, as we do not have counterfactuals available for these variables. We use the same training protocol as outlined in **Section 4.2**. The factual climate is based on ERA5 reanalysis, providing physically consistent and

observation-constrained meteorological conditions for the fire event. The counterfactual climate represents a world without human influence on the climate system. It is created by adjusting ERA5 temperature, maximum temperature, precipitation, dry days, consecutive dry days, humidity, and minimum humidity variables using variable-specific adjustment functions ("deltas"). These deltas are derived from differences between the HadGEM3-A ALL-forcings and natural-forcings simulations described in **Section 5.1.2**, with:

$$\omega(CF) = \omega(ERA5) + \omega(NAT) - \omega(ALL)$$

Where CF is the counterfactual climate, ω is the transformation required to remove data bounds of the specific variable, and φ is the inverse of ω. The following transformations are applied to create counterfactual values for each climate variable:

- Temperature (Mean and Max): $\omega(x) = x$
- Precipitation: $\omega(x) = \log(e^x-1)$
- Windspeed, soil moisture: $\omega(x) = \log(x)$
- Relative Humidity: $\omega(x)=\log(x/(1-x))$

Since relative humidity (RH) is not available directly from ERA5, we will therefore calculate it from 2m temperature (T_s) and 2m dew point temperature (T_d):

$$RH = 100 \times e_d/e_s$$

where e_d is the actual vapour pressure (calculated from the dewpoint temperature) and e_s is the saturation vapour pressure (calculated from the air temperature):

$$e_i = 6.112 \times exp\left(\frac{17.625 \times T_i}{T + 243.04}\right)$$

We perform two types of counterfactual simulations to understand the influence of human-caused climate change: one using all individual members of the HadGEM3-A ensemble, and one using the ensemble mean. The full ensemble captures a wide range of possible weather outcomes and includes natural year-to-year variability, making it a more cautious or conservative estimate of the effect of climate change. The ensemble mean, by contrast, smooths out this variability to isolate the long-term influence of climate forcing, providing a cleaner signal. Since our analysis targets a specific year, the actual role of weather variability should, in theory, matter less. However climate change can interact with this variability in complex, sometimes non-linear ways, thereby making certain extremes more or less likely depending on the background conditions, we don't know exactly where within that range the real-world outcome lies. As a result, the true effect of climate change likely falls somewhere between these two estimates. We therefore report the full ensemble results as our main findings and refer to the ensemble mean where it offers useful additional context or diverges substantially.

We also use an **ISIMIP configuration** of ConFLAME, as used in last year's report. The available data differs from our near real-time setup, so for this configuration we group controls into four categories (**Table S3**):

1. **Fuel load**, represented by total vegetation cover and tree cover.
2. **Fuel moisture**, represented by mean consecutive dry days within each month, the fraction of dry days within the month, daily mean precipitation, mean and maximum monthly temperature, and mean and maximum vapour pressure deficit (VPD).
3. **Ignitions**, represented by climatological lightning, pasture, crop, and population density.
4. **Suppression**, represented by pasture, crop, and population density.
5. **Land use change**, represented by 12 month running mean change in tree, crop, and pasture.

We trained the ConFLAME ISIMIP configuration on observed monthly BA from the MODIS BA product (MCD64A1) during 2003-2019 at 0.5° resolution across the entire region. For model training and for factual, we used Global Soil Wetness Project Phase 3 (GSWP3-W5E5) meteorological forcings, as provided at 0.5° spatial resolution by ISIMIP3a (see Table 5). Land surface information (tree cover and non-tree vegetated cover) was derived from dias corrected JULES-ES-ISIMIP model output (Mathison et al., 2023), which was also driven by GSWP3-W5E5. This model includes dynamic vegetation, accounting for changing vegetation cover in response to climate, growth, competition, and mortality. To avoid double-counting the impact of fire, we disabled the model's interactive vegetation-fire module. The bias in this land surface information is adjusted to the MODIS Vegetation Continuous Fields collection 6.1 remote sensed data (Dimiceli et al., 2015), using a linear scaling approach. This preserves trends between historical and future periods and ensures accurate means and distribution. See **Supplementary Text S2** for details.

S5.1.3.1 Deriving ConFLAME vegetation fraction driving data

In **Sections 5.3.1**, and **6.1.2.2,** we drive ConFLAME with tree and non-tree vegetated cover from the Joint UK Land Environment Simulator Earth System impacts model (JULES-ES) at version 5.5 (Clark et al., 2011; Mathison et al., 2023) driven with GSWP3-W5E5 forcings provided at a 0.5° spatial resolution by ISIMIP3a. These runs are freely available at https://www.isimip.org/impactmodels/details/292/. JULES-ES dynamically models vegetation cover in response to meteorology, hydrology, nitrogen availability, and land use change. JULES-ES has been extensively evaluated against snapshots and site-based measurements of vegetation cover and carbon (Burton et al., 2019, 2022; Clark et al., 2011; Mathison et al., 2023; Sellar et al., 2020). JULES-ES-ISIMIP has previously been used as driving data for ConFLAME to perform future projections (UNEP et al., 2022), though using a previous round of ISIMIP climate forcing (ISIMIP2b). As per (UNEP et al., 2022), vegetation responses to JULES-ES's internal fire model were turned off so as not to double-count the effects of burning.

However, in (UNEP et al., 2022), residual JULES-ES simulated biases in vegetation cover were allowed to persist, increasing the uncertainty range of local vegetation cover and resultant burned area responses. We therefore correct the bias in JULES-ES's vegetation cover using a linear scaling bias adjustment method, implemented using the ibicus software package (Spuler et al., 2024, ibicus).

The method corrects the bias induced by the JULES-ES model rather than the bias of the climate model, assuming that this has been removed by the ISIMIP3BASD method(Lange, 2019). For each surface cover type at each grid cell, the bias adjustment method identifies biases in the mean and variance of the JULES-ES model output relative to MODIS VCF collection 6.0 remotely sensed data (Dimiceli et al., 2015) at this grid cell. These biases in mean and variance are then removed from the surface information output from JULES-ES driven by climate models over the historical (1994-2014) and future (2015-2099) period, ensuring that the resulting model output is still bounded by [0, 1]. This bias adjustment method preserves the trend in mean and variance. While a trend-preserving empirical quantile mapping was used in the State of Wildfires 2023/24 publication, further analysis showed that, given the limited amount of observational data, this simpler method performs equally well while requiring fewer assumptions and parameters to fit, leading to an overall more robust bias adjustment.

The results were evaluated in terms of the ability of the bias correction method to reduce the model bias over the historical period, as well as preserve the trend between the future and historical periods. It was found that the method corrects the bias well over the historical period for most regions, variables and grid cells in both the mean and 80th percentile at each

grid cell. The mean trend between the future and historical period is preserved by definition, but also quantile trends in most regions and grid cells are well preserved.

To demonstrate the evaluation conducted, **Figure S27** shows the results for tree cover over the Amazon region. The plots for the remaining regions, including tree and no-tree cover, can be found in a notebook https://github.com/jakobwes/State-of-Wildfires---Bias-Adjustment. Investigating the time series of average tree cover over the region, we find that the correction method reduces the bias over the historical period and matches the future period to the historical period (**Figure S27**a). The cumulative distribution functions of average tree cover merged over all spatial locations in observations and the model matches better after bias adjustment (**Figure S27b**). They do not match perfectly, and we note that this is a non-calibrated aspect that we do not expect to have zero bias, but that is important to evaluate. Furthermore, we find that the improvement in both mean and 80th percentile holds across the region (**Figure S27c**). The trend between future and historical periods is preserved for the majority of grid-cells, with the absolute change in trend being close to zero for most grid-cells.

S5.1.4 FireMIP

For the multi-model ensemble we use simulations from the ISIMIP3a fire sector, as published in (Burton & Lampe et al. 2024). The 7 models reporting BA for ISIMIP3a are shown in **Table S3**. The methodology follows the ISIMIP3a Impacts Attribution protocol, as outlined in (Mengel et al., 2021), where the factual historical simulations are driven with GSWP3-W5E5 reanalysis data, and the counterfactual simulations are the same historical data which has been detrended via quantile mapping (Mengel et al., 2021).

As outlined in (Hantson et al., 2016), the spread in the absolute BA is large amongst the observations, models and regions and therefore a normalised relative anomaly (RA) rather than absolute BA is used for the analysis. To calculate the RA in present day BA, we subtract the counterfactual mean, and divide by the counterfactual mean. By comparing both factual and counterfactual experiments to the counterfactual mean, we are looking at the fractional increase in BA driven by climate change compared to a baseline without climate change. Based on model performance by AR6 region, a region-specific weighting is also applied following (Knutti et al., 2017). The weighting is based on the model's distance to the observed BA temporal RA using both FireCCI5.1 and GFED5, measured using NME as per Kelley et al. (2013). To measure the uncertainty, random noise is generated and scaled by the climatological RMSE of each model. This noise is then added to the modelled relative anomaly, this process is repeated 1000 times. Then, bootstrapping is applied to the monthly regional BA RA (now with noise added in) according to the weight for each model. Uncertainty is calculated by taking the 2.5-97.5th percentile of the resultant histogram. All results are reported as P50 [P2.5, P97.5]. The methods are explained in full in (Burton & Lampe et al. 2024).

Table S3: FireMIP Models used for attributing median burned area. Table reproduced from (Burton & Lampe et al. 2024)

Model		**CLASSIC**	**INFERNO**	**LPJ-GUESS-SIMFIRE-BLAZE**	**LPJ-GUESS-SPITFIRE**	**ORCHIDEE-MICT-SPITFIRE**	**SSiB4/ TRIFFID**	**VISIT**
Fire Model		CLASSIC	INFERNO	SIMFIRE	SPITFIRE	SPITFIRE	Li	After (Thonicke et al., 2008))
Land / Vegetation		CLASSIC	JULES	LPJ-GUESS	LPJ-GUESS	ORCHIDEE	SSiB	VISIT
Dynamic Veg	**Physiology**	Yes	Yes, via TRIFFID	Yes	Yes	Yes	Yes, via TRIFFID	Yes
	LAI	Yes	Yes, via TRIFFID	Yes	Yes	Yes	Yes	Yes
	Bio-geography	No	Yes, via TRIFFID	Yes	Yes	Yes	Yes	No
Nitrogen Cycle		Yes	Yes	Yes	Yes	No	Yes	Yes, but C-N coupling is limited
No. PFTs		9	13	17	17	19	7	33 (biome types)
No. Soil Layers		20	4	2	2	11	3	2
Fuel		Vegetation and litter	Vegetation & top soil layer as proxy for litter	Vegetation, litter	Litter	Vegetation and litter	Vegetation and litter	Litter
Ignitions	**Natural**	Prescribed lightning	Prescribed lightning	SIMFIRE describes annual BA + fire-climatology -> daily BA used as Fire-Probability	Prescribed lightning	Prescribed lightning	Prescribed lightning	Probabilistic based on fuel wetness
	Anthropogenic	Prescribed population density	Prescribed Population density	SIMFIRE includes suppression by humans	Prescribed population density	Prescribed population density	Prescribed population density	No

Suppression	Prescribed population density	Crops, population density	Crops (100%), prescribed population density (Hyde3.1)	Crops, population density	Prescribed population density, crops	Prescribed population density and GDP	Low fuel load
Spread	Wind speed and soil moisture	None	Daily BA (no explicit spread)	Rothermel equations including wind speed, tree fraction, grass fraction, fuel moisture, fuel load and characteristics	wind speed, tree fraction, grass fraction, fuel moisture, fuel load	Wind speed and soil moisture	None
Model inputs	SW & LW radiation, precipitation, air temperature, specific humidity, wind speed, atmospheric pressure, population density, lightning	SW & LW radiation, precipitation, air temperature, specific humidity, wind speed, population density, lightning	SW radiation, precipitation, air temperature (mean, min, max), relative humidity, wind speed	SW radiation, precipitation, air temperature, specific humidity, wind speed, atmospheric pressure, population density, lightning	SW & LW radiation, precipitation, air temperature, specific humidity, wind speed, atmospheric pressure, PFT map, population density	SW & LW radiation, precipitation, air temperature, specific humidity, wind speed, atmospheric pressure, population density, and GDP, peat map, land cover change	Air temperature, precipitation, air vapor pressure, cloudiness, wind
Resolution	1 deg	0.5 deg	0.5 deg	0.5 deg	0.5 deg	0.5 deg	0.5 deg
References	(Melton et al., 2019)	(Burton et al., 2019, 2020; Mangeon et al., 2016)	(Knorr et al., 2014; Rabin et al., 2017; Smith et al., 2014)	(Lehsten et al., 2009; Rabin et al., 2017; Smith et al., 2014; Thonicke et al., 2010)	(Yue et al., 2014, 2015)	(Huang et al., 2020, 2021; Hugelius et al., 2013; Li et al., 2012, 2013)	(Ito, 2019)

S5.2 Results

S5.2.1 Background changes in fire weather this decade

S5.2.1.1 Northeast Amazonia

Area/Time: *All region/Jan–Mar 2024*
Variable: *Fire Weather Index*
Attribution Type: *Anthropogenic climate forcing*
Includes: *Changes in climate since Pre-Industrial*

To understand longer-term trends, we estimate how global warming has changed the average likelihood of extreme fire weather over the past decade. Using a statistical fit to the CanESM5 model ensemble, we find that fire weather conditions like those seen in 2024 have become 1.9 times more likely on average since pre-industrial times, with a 95% confidence range of [1.5, 53.3].

While this method gives less event-specific resolution, it supports the conclusion that climate change has increased the background risk of extreme fire weather in the region over the last 10 years reinforcing the HadGEM-based result.

S5.2.1.4 Congo Basin

Area/Time: *All region/Jun-Aug 2014-2025*
Variable: *Fire Weather Index*
Attribution Type: *Anthropogenic climate forcing*
Includes: *Changes in climate since Pre-Industrial*

Using the CanESM5 ensemble, we find that fire weather conditions similar to those observed in July–August 2024 were 1.3 times more likely due to climate change ([0.7, 1.8], 95% CI) over the last decade. While more uncertain than the HadGEM3-A analysis, the findings are not inconsistent: both show a positive central estimate. The difference likely reflects the broader decadable sampling of the CanESM5 method or as well as differences in the underlying model systems. However, both methods suggest that climate change has increased the likelihood of fire-conducive weather in the Congo Basin.

S5.2.2 Region-wide extreme BA during 2024-25.

S5.2.2.1 Northeast Amazonia
Time: *Jan-Mar 2003-2019*
Variable: *Burned Area*
Attribution Type: *Total climate change*
Includes: *All anthropogenic and natural trends in climate*

We also assessed the influence of total climate forcing on the frequency of fire activity in the Northeast Amazonia for all January-March during 2002-2019. The likelihood of a climate-driven increase in regional burned area (BA) during these ~2 decades was just 56% (**Figure 14**), indicating that any long-term trend remains highly uncertain. The central amplification factor was 1.17, with a 90% confidence range of 0.88 to 1.15 (**Table 6**), encompassing the possibility of no change. In contrast to the direct attribution of the 2024 fire season, this analysis shows no clear signal that total climate forcing increased overall BA

during this earlier period. A similar picture emerges for sub-regional extremes, with a likelihood of an increase due to climate forcing was 70%, just meeting the IPCC threshold for being considered likely. The amplification factor was modest-1.02, with a 90% range of 0.94 to 1.13-indicating that while climate may have played a role in enhancing the most intense burning, its influence was relatively small and uncertain during this timeframe.

Together, these results suggest that while anthropogenic climate change had a strong and detectable impact on the 2024 fire season, similar effects were not consistently evident in the decades prior. The relatively low upper bounds on amplification, particularly for sub-regional extremes, imply that large increases in anomalous fire activity were not widespread prior to 2020. This interpretation aligns with earlier research (Kelley et al., 2019) showing only a weak meteorological contribution to elevated burning in the southern parts of the region during the large fire anomalies in 2019.

However, it is important to note that the analysis ends in 2019, excluding a series of major droughts and fire anomalies since 2020. These recent years have shown increasingly frequent and widespread extremes, suggesting that the climate signal may now be strengthening. This is consistent with last year's report, which analysed a Western Amazonia region just southwest of this one. There, long-term trends similarly suggested only marginal increases in sub-regional extremes from 2002–2019, while the risk ratios for specific fire weather events were extremely high. A longer observational window that includes the last five years would help better evaluate whether a persistent shift is emerging.

Time: *Jan-Mar 2003-2019*
Variable: *Burned Area*
Attribution Type: *Socioeconomic forcing*
Includes: *Population density, land use and land cover change*

For sub-regional extremes, the likelihood that socioeconomic factors increased BA was only slightly higher at 62%. The central Amplification Factor was 1.01, with a narrow range of 0.96 to 1.10, indicating only minimal influence. This suggests that in the most fire-affected locations, socioeconomic drivers alone did not strongly amplify the extent of burning during this timeframe. Together, these findings point to a limited or unclear role of socioeconomic change in driving extreme fire activity across the Northeast Amazonia between 2002 and 2019.

Time: *Jan-Mar 2003-2019*
Variable: *Burned Area*
Attribution Type: *All forcing*
Includes: *All anthropogenic and natural trends in climate, population density, land use and land cover change*

We also assessed the combined effect of total forcing, which includes all long-term changes in climate (anthropogenic and natural), land use, land cover, and population density,on burned area (BA). For regional totals, the likelihood that total forcing increased BA was just 47% (**Figure 14**), with a median amplification factor of 0.99 and a 90% confidence interval of 0.81 to 1.47 (**Table 6**). This result indicates no clear signal that the combined effects of climate and socioeconomic change had a net impact on fire activity across the region during this two-decade period. For sub-regional extremes,the grid cells with the highest BA in each season, the likelihood of an increase was slightly higher at 62% (**Figure 14**), with a central amplification of 1.01 and a wider confidence interval of 0.96 to 5.1 (**Table 6**). While this suggests that some influence of combined human and climatic drivers on extreme BA cannot be ruled out, the signal remains modest and uncertain overall.

Together, these findings imply that, even when considering all major sources of long-term change in climate and land use together, there is insufficient evidence to attribute a consistent trend in BA or its extremes across the region for 2002–2019. The relatively wide range for the sub-regional extremes, compared to regional totals, highlights a possibility that landscape modification or localised climate feedbacks could have amplified fire activity in specific hotspots, but the model does not provide enough resolution to identify or confirm such patterns.

S5.2.2.2 Pantanal and Chiquitano

Time: *Aug-Sep 2003-2019*
Variable: *Burned Area*
Attribution Type: *Total climate change*
Includes: *All anthropogenic and natural trends in climate*

Over the longer-term 2003–2019 period, our analysis suggests that it was virtually certain that total (99%; **Figure 14**) that climate change very likely increased the likelihood of fire events with comparable burned area to August–September 2024 in the Pantanal & Chiquitano region. The median likely amplification factor greater than 100 [90% confidence range of 4.92 >100] (**Table 6**). This suggests that a substantial portion - and possibly the vast majority, of the burned area associated with 2024-like events is attributable to long-term anthropogenic changes in the climate system. The sub-regional attribution signal is consistent with the regional-scale result, which also shows >99% likelihood of an increase (**Figure 14**), with an amplification factor >100 [2.72 to >100] (**Table 6**). While both estimates exhibit wide uncertainty ranges, their overlapping confidence intervals point to a consistent climate signal rather than a statistically clear difference in impact strength between regional and sub-regional scales.

This analysis provides additional confidence in the role of anthropogenic climate change by situating the 2024-type fire conditions within the broader distribution of fire-weather years over the past two decades. By extending the analysis beyond the specific year of 2024, it helps to identify a persistent fingerprint of climate forcing in driving elevated fire risk.

By drawing on multiple years of climate and fire conditions, this longer-term approach increases the sample size available for evaluating the likelihood of 2024-like fire events. This may help separate the structural influence of climate forcing more clearly than near-real-time (NRT) event-based attribution. Further analyses comparing NRT and multi-year setups could help explore whether recent variability has masked or amplified long-term trends in fire likelihood.

Time: *Aug-Sep 2002-2019*
Variable: *Burned Area*
Attribution Type: *All forcing*
Includes: *All anthropogenic and natural trends in climate, population density, land use and land cover change*

When assessing the combined influence of all anthropogenic and natural forcings, we find limited attribution power for 2024-like events in the Pantanal and Chiquitano region. At the regional scale, the likelihood that all forcings increased burned area is 61%, with an amplification factor (AF) of 1.05 [0.26–64.3]. This wide uncertainty range suggests that internal variability and counteracting drivers may obscure the net effect of all forcings. For sub-regional extremes, confidence is slightly higher: 84% likelihood, with an AF of 1.00 [0.68–12.16]. This points to a potential increase in burned area, though again with considerable uncertainty.

While these results do not offer conclusive evidence of a net anthropogenic effect, they underscore the complexity of attributing fire outcomes to the combined influence of climate and human activity. The limited confidence in these findings highlights the need to improve methodologies capable of capturing interactions and feedbacks between land use, climate, and fire, particularly in regions such as Pantanal and Chiquitano, where these relationships are highly complex. Future reports should move beyond treating climate and socioeconomic drivers in isolation. As interactive and compounding effects become more likely, attribution frameworks that separate human and climate influences risk overlooking critical synergies that are most relevant for effective policy and risk management.

S5.2.2.3 Southern California

Time: *Jan 2003-2019*
Variable: *Burned Area*
Attribution Type: *Total climate change*
Includes: *All anthropogenic and natural trends in climate*

There is limited evidence from this framework that total climate change increased the likelihood of January 2025-like regional burned area in Southern California during the 2003–2019 period. The likelihood of an increase is estimated at 63% (**Figure 14**) with an amplification factor (AF) of 1.07 [0.68–2.83] (**Table 6**), suggesting that total climate change could have played a role, but the model does not provide a confident answer either way. This large range of uncertainty partially stems from the small geographic size of the region, which limits signal-to-noise ratios in long-term attribution frameworks. A similar issue was observed for Greece in last year's report (Jones et al., 2024b), where a confident climate signal was also absent in long-term regional attribution, despite strong evidence emerging from event-specific analysis. Interestingly, while the long-term climate signal here is weak, the near-real-time (NRT) attribution for the 2025 event itself shows a much stronger likelihood of anthropogenic influence, suggesting that climate signals may emerge more clearly during specific extremes than across broader multi-year variability.

As the amount of burned area in January in Southern California is historically nominal given that this is the traditional wet season when flammability is low, some of the elevated uncertainty may stem from local calibration. Likewise, these were principally wind-driven fires due to synoptic-mesoscale features with Santa Ana downslope winds whose features are poorly resolved in the coarse reanalysis data used here. Climate projections show a weak attenuation of the frequency of Santa Ana winds with anthropogenic climate change (Guzman-Morales and Gershunov, 2019; Hawkins et al., 2022), but also an extension of critically dry fuels into winter due to delayed onset of winter precipitation (Goss et al., 2020). The degree to which these two factors alongside the direct thermal influence of climate change on fuel desiccation altered the odds of such extremes requires additional analysis and may not be realized through the approaches used here.

Time: *Jan 2002-2019*
Variable: *Burned Area*
Attribution Type: *All forcing*
Includes: *All anthropogenic and natural trends in climate, population density, land use and land cover change*

There is no clear signal for the impact of all forcing for January 2025-like burned area in Southern California during 2002–2019. The likelihood of an increase is estimated at 55%, with an amplification factor of 1.05 [0.26–64.26], nearly identical to the socioeconomic-only

result. This further highlights the challenge of drawing confident conclusions in small regions with limited signal.

S2.2.2.4 Congo Basin

Time: *Jun-Aug 2024*
Variable: *Burned Area*
Attribution Type: *Total climate change*
Includes: *All anthropogenic and natural trends in climate*

Total climate change likely increased the amount of burned area in areas with the height levels of burning, though with limited confidence in the size of this effect. The likelihood of an increase was estimated at 75%, with an amplification factor (AF) of 1.29 [0.96–3.32]. This implies that while a contribution from climate change is more likely than not, the possibility of little to no effect cannot be ruled out. The risk ratio was 1.8, suggesting that events of this severity were nearly twice as likely under current climate conditions than they would have been in a pre-industrial climate.

Time: *Jun-Aug 2024*
Variable: *Burned Area*
Attribution Type: *All forcing*
Includes: *All anthropogenic and natural trends in climate, population density, land use and land cover change*

For the region as a whole, the likelihood of all human and climate forcing increased burning was 55%, with an amplification factor (AF) of 1.01 [0.86–1.42], indicating no clear signal. In the areas most severely affected by fire, the likelihood rose slightly to 63%, with an AF of 1.06 [0.73–4.44]. While this suggests that the combined effect of all forcings could have contributed to the sub-regional extremes, the wide range and low confidence highlight the challenge of attributing fire outcomes in regions where both data and model constraints remain significant.

S5.2.3 Sub-regional extreme burned area during 2024-25

S5.2.3.1 Northeast Amazonia

Area/Time: *Sub-regional extremes/Jan-Mar 2024*
Variable: *Burned Area*
Attribution Type: *Anthropogenic climate forcing*
Includes: *Greenhouse gases, aerosols, and land-use change effects on climate*

Anthropogenic climate forcing also very likely caused increased burned area (BA) in the sub-regional extremes with a likelihood of 96% (**Figure 14; Table 6**). The amplification factor in these areas was smaller than for the region as a whole: fires in these high-BA zones were on average 1.17 times larger, with a 90% confidence range of 1.01 to 5.13. This means that anthropogenic climate forcing likely contributed to increased burning in these areas, though the amplification was more modest than across the broader region. The risk ratio was 2.2, indicating that fire seasons with this spatial pattern of extreme burning are now more than twice as likely due to climate change.

This difference between regional and sub-regional extremes is consistent with earlier findings in **Section 4**, which showed that climate-driven weather anomalies - more directly linked to the influences considered in our attribution, increased the potential for burning across much of the region, while fuel conditions (fuel load and moisture) shaped the location

and timing of the most severe burning. The moderate amplification factor in the highest-BA grid cells likely reflects the local interplay between fire weather and fuel constraints, where factors such as fuel limitations or ignition variability may have restricted how much additional burning occurred, even under climate driven more fire conducive weather conditions.

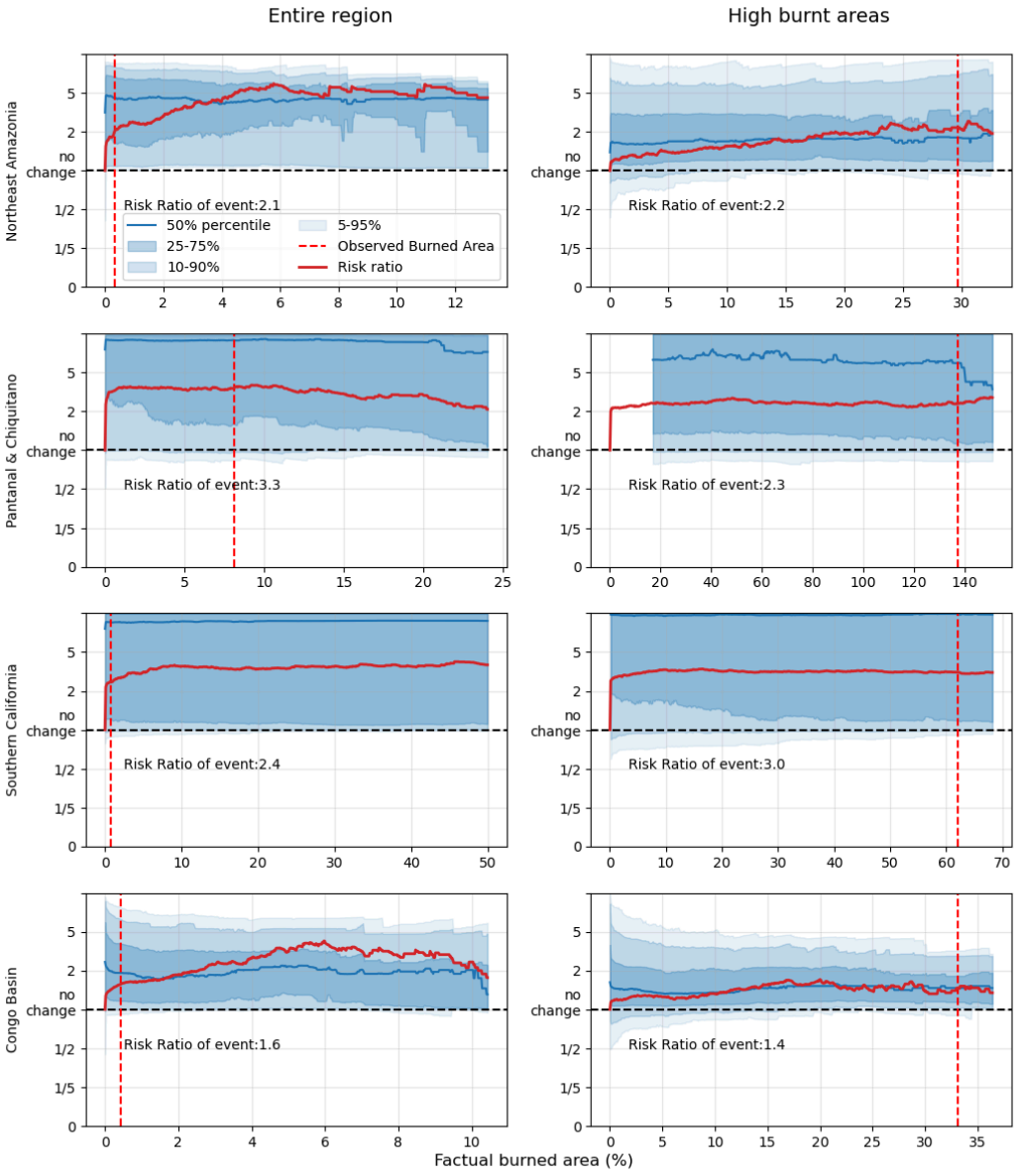

Figure S23 Risk ratio and amplification factor for different levels of total (left) and sub-regional extreme (right) burned area, simulated using ConFLAME-NRT for each region (rows). Percentile ranges for the amplification factor are taken across ensemble members. The red dashed vertical line indicates observed levels of burned area, for which the corresponding risk ratio is reported in each panel.

S5.2.3.2 Pantanal and Chiquitano

Area/Time: *Sub-regional extremes/Aug-Sep 2024*
Variable: *Burned Area*
Attribution Type: *Anthropogenic climate forcing*
Includes: *Greenhouse gases, aerosols, and land-use change effects on climate*

Anthropogenic climate forcing was very likely to have increased BA for the sub-region with the highest burned areas in August-September 2024, with a 90% likelihood of increased burned area in the factual simulations compared to the counterfactual (**Figure 14**). The amplification factor (AF) was 1.91, albeit with a wide uncertainty range [0.98–>100] (**Table 6**), suggesting that while the median influence was lower than for regional totals, very large increases in burned area due to climate change cannot be ruled out. A similar likelihood of increase and upper bound was found when using ensemble-mean meteorology for the counterfactual.

The risk ratio for these sub-regional extremes was 2.3 (**Table 6**), indicating more than twice the likelihood of observing similar extreme burned area under current anthropogenic conditions relative to a natural climate.

As with Northeast Amazonia, the anthropogenic influence appears less pronounced for the most severely affected areas than for the region overall. This could reflect local fire–moisture–fuel feedbacks limiting amplification where BA was already high, or shifts in fire-prone zones expanding regional totals without intensifying extremes. Further investigation into local factors such as wetlands and fuel constraints will be key to understanding why the climate signal appears weaker in the areas that burn most. One possible explanation is that wetlands and other moisture-rich ecosystems may help buffer fire activity, even as climate conditions change. Another contributing factor could be land use in these extreme fire areas. For example, fire suppression in human-managed landscapes may interact with climate drivers in ways that reduce the strength of attribution signals.

S2.2.2.2 Southern California

Area/Time: *Sub-regional extremes/Aug-Sep 2024*
Variable: *Burned Area*
Attribution Type: *Anthropogenic climate forcing*
Includes: *Greenhouse gases, aerosols, and land-use change effects on climate*

Due to the relatively small size of the Southern California study region, the identified sub-regional extremes correspond to a single model grid cell thus limiting the ability to capture nuances of the distinct fire regimes and mesoscale factors associated with Santa Ana winds (Kolden and Abatzoglou, 2018). As the attribution results are qualitatively similar to those for the full region for all comparisons (Table 6), we do not discuss a separate analysis of sub-regional extremes here.

S5.2.4 Background Changes in Burned Area this Century - all forcings

S5.2.4.1 Northeast Amazonia

Area/Period: *All region/2003-2019*
Variable: *Background Burned Area*
Attribution Type: *All forcing*
Includes: *All anthropogenic and natural trends in climate, population density, land use and land cover change*

When both climate and socioeconomic forcings are considered together, their effects largely offset one another, leading to a small and uncertain net change in BA of +1% [-6%, +9%]. In this region, we observe that the effects of climate change and socio-economic factors on BA have approximately counteracted to produce no clear overall change in background levels of BA this century.

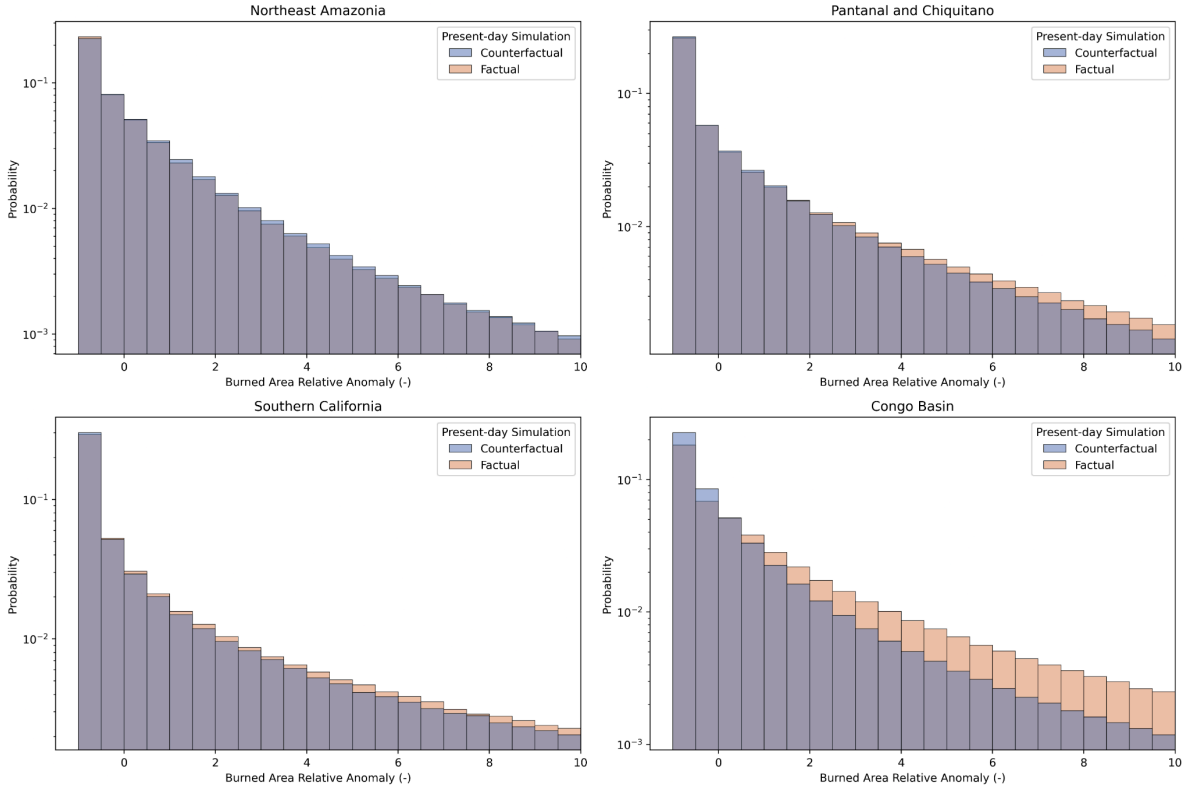

Figure S24: Change in median BA due to total climate forcing from FireMIP. Present day BA (2003-2019) for factual (historical forcing, orange) and counterfactual (detrended climate, blue). Probability is shown on a log scale.

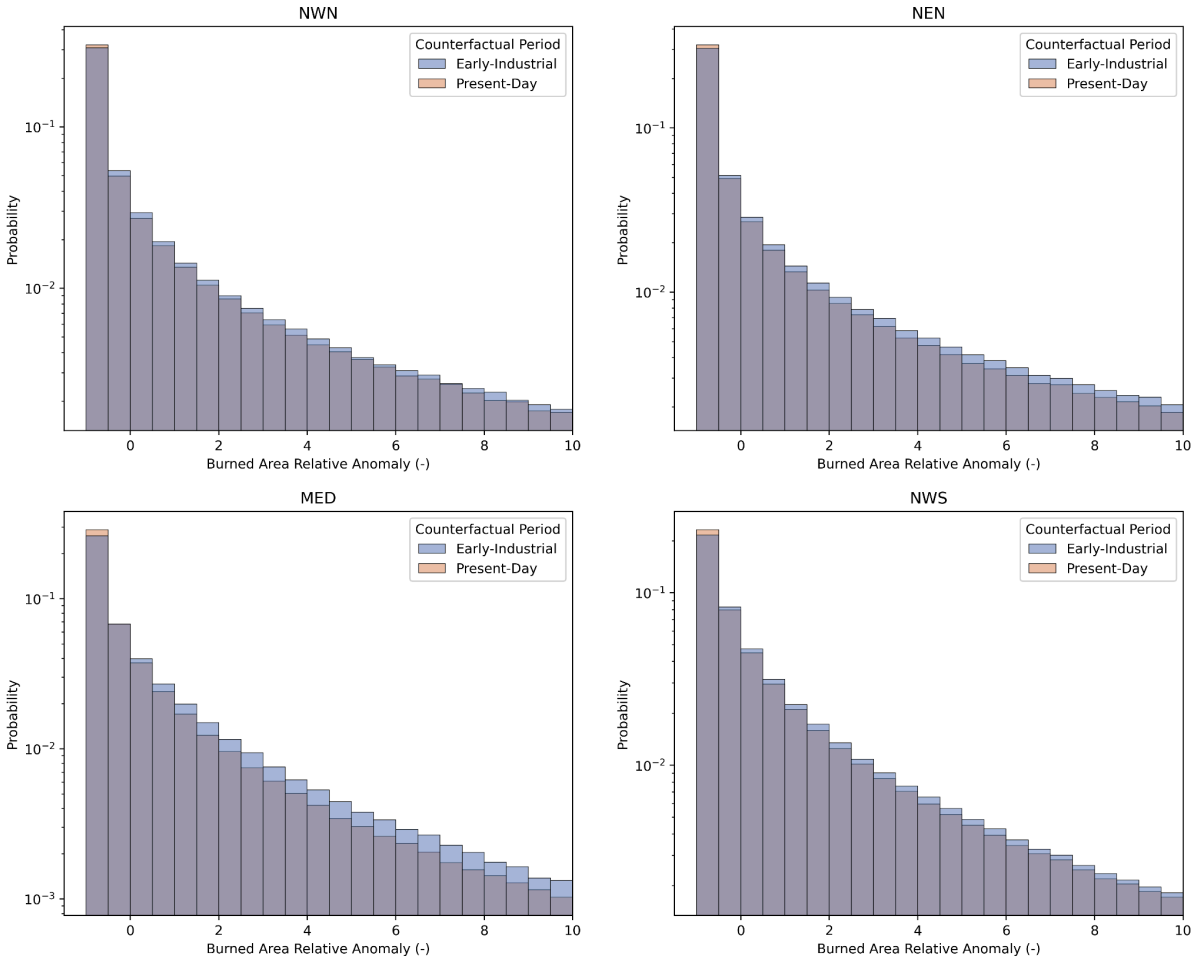

Figure S25: Change in median BA anomaly due to socioeconomic factors (population and land-use change) from FireMIP. Present day BA (2003-2019) for counterfactual (detrended climate, orange) compared to early-industrial (1901-1917) in the counterfactual (detrended climate, blue), for AR6 regions. Top row: North West North America (NWN, LEFT) and North East North America NEN (RIGHT). Bottom row: Mediterranean (MED, LEFT), and North West South America (NWS, RIGHT). Probability is shown on a log scale.

S5.2.4.2 Pantanal and Chiquitano

Area/Period: *All region/2003-2019*
Variable: *Background Burned Area*
Attribution Type: *All forcing*
Includes: *All anthropogenic and natural trends in climate, population density, land use and land cover change*

When considering the combined effects of climate change and socioeconomic drivers, we estimate a net change in background BA at +3% [-2%, 9%]. This modest and uncertain increase likely reflects offsetting influences, where climate-driven increases in fire activity have been partially counteracted by human-driven factors such as land management, suppression practices, or landscape fragmentation. While the net change is close to zero, the underlying drivers may still be highly active in opposing directions, a dynamic that warrants further investigation to support more effective fire policy and adaptation planning.

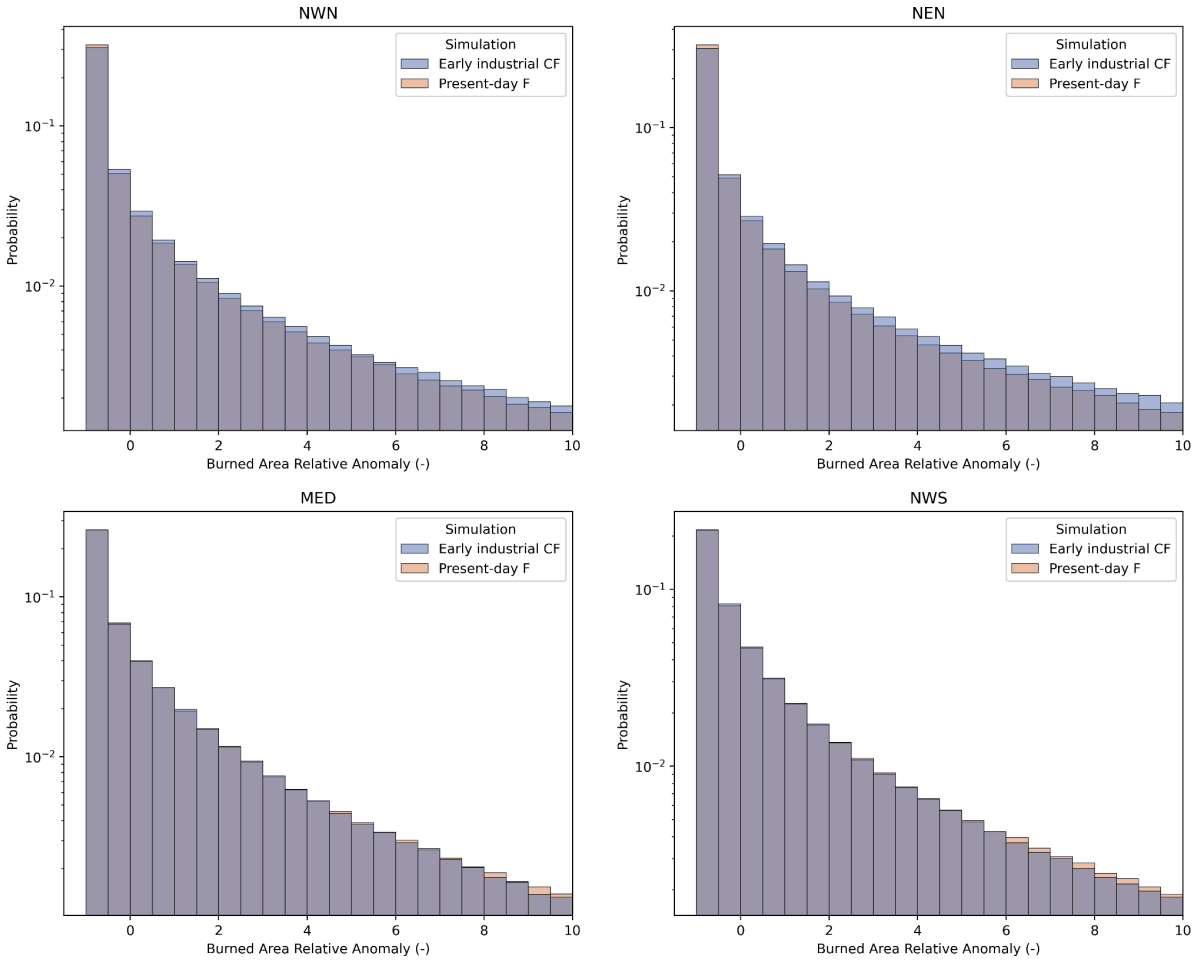

Figure S26: Change in median BA anomaly due to all forcing (climate change and socioeconomic factors) from FireMIP. Present day BA (2003-2019) for factual (historical forcing, orange) compared to early-industrial (1901-1917) in the counterfactual (detrended climate, blue), for AR6 regions. Top row: North West North America (NWN, LEFT) and North East North America NEN (RIGHT). Bottom row: Mediterranean (MED, LEFT), and North West South America (NWS, RIGHT). Probability is shown on a log scale.

S5.2.4.3 Congo Basin

Area/Period: *All region/Jun-Aug 2024*
Variable: *Background Burned Area*
Attribution Type: *All forcing*
Includes: *All anthropogenic and natural trends in climate, population density, land use and land cover change*
When accounting for all anthropogenic and natural trends (i.e. climate change, population dynamics, and land use change) we estimate that total background burned area in the Congo Basin increased by 25% [18%, 33%] over the 2003-2019 period compared to pre-industrial conditions. This result reflects the net outcome of competing influences: while socioeconomic factors appear to have reduced fire activity (as noted in the previous section), climate change has likely increased the underlying fire risk, particularly through changes in temperature, rainfall patterns, and vegetation dynamics.

The net increase in background fire activity does not necessarily imply more fire during extreme years, but it does suggest that the baseline fire environment is shifting. Over time, this could reduce the threshold for extreme events to occur or make recovery between fire seasons more difficult.

S6 Supplementary Material for Section 6

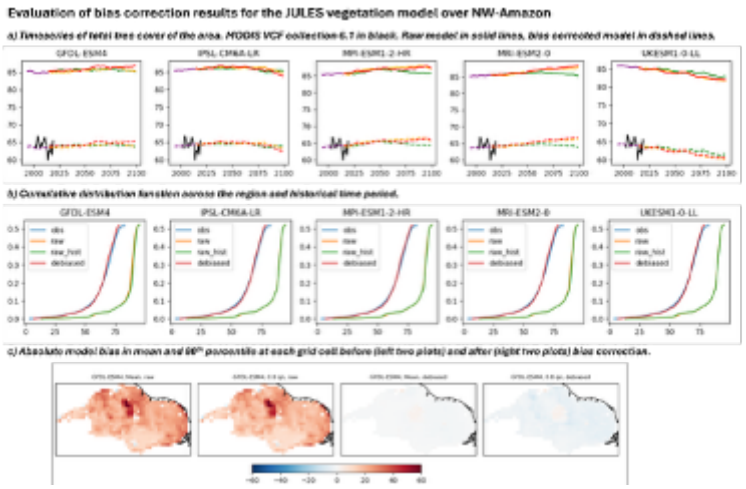

Figure S27: Evaluation of the JULES vegetation model bias adjustment for tree cover over the Amazon region. a) Time series of tree cover over the area (in percent) for different climate models, both with historical and scenario runs, raw model in solid lines, bias corrected models in dashed lines and MODIS VCF in black. b) Cumulative distribution function of tree cover values across region and historical time period for different climate models for observations (blue), raw models (orange), raw historical models (green) debiased models (red). c) Absolute model bias in mean and 80th percentile for the GFDL-ESM4 climate model before (left two plots) and after bias adjustment (right two plots).

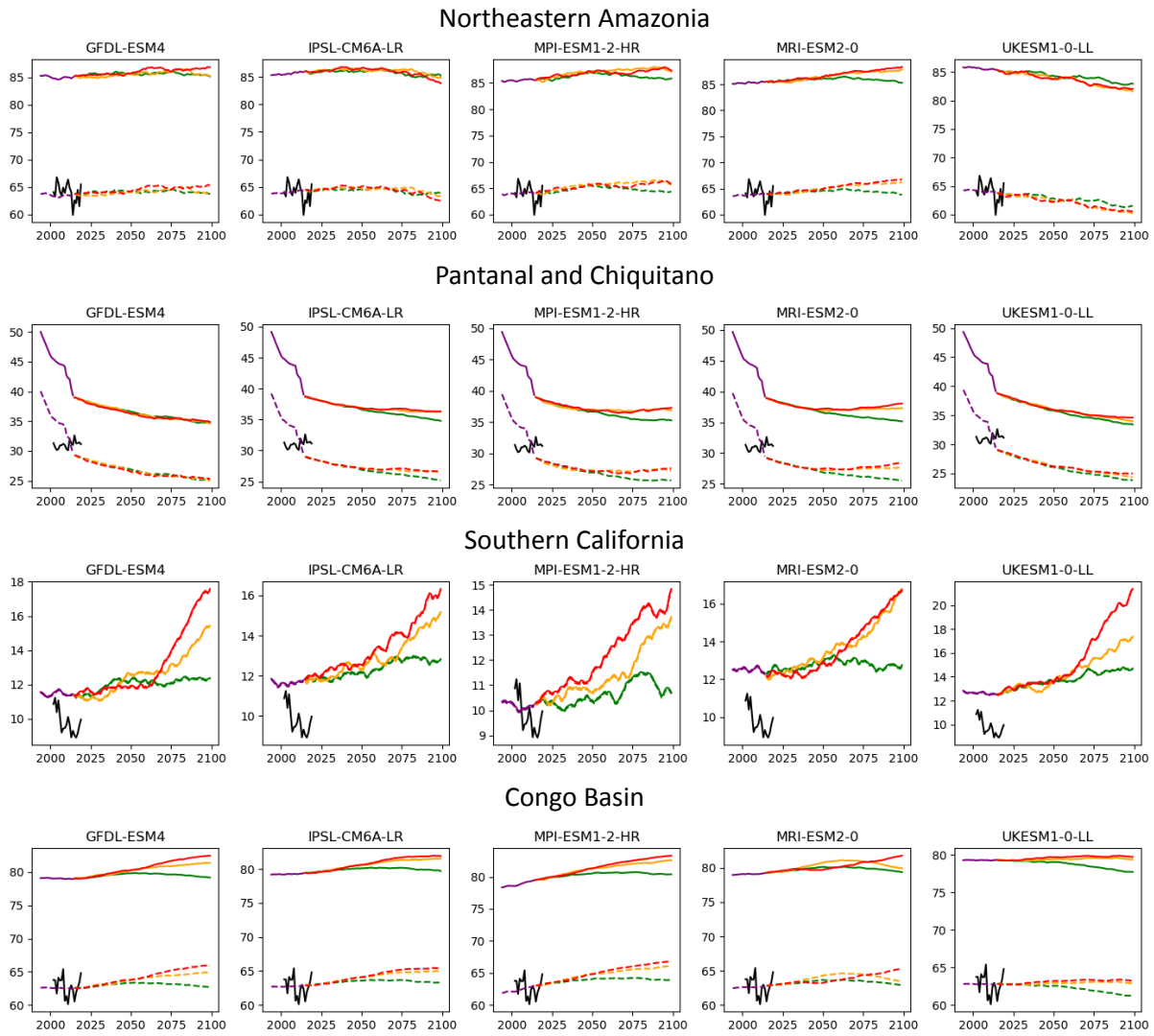

Figure S28: Time series of tree cover over each focal region for different climate models, both with historical and future scenario runs, raw model in solid lines, bias corrected models in dashed lines and MODIS VCF in black. Note that for Southern California, bias and none-bias corrected time series overlap one another.

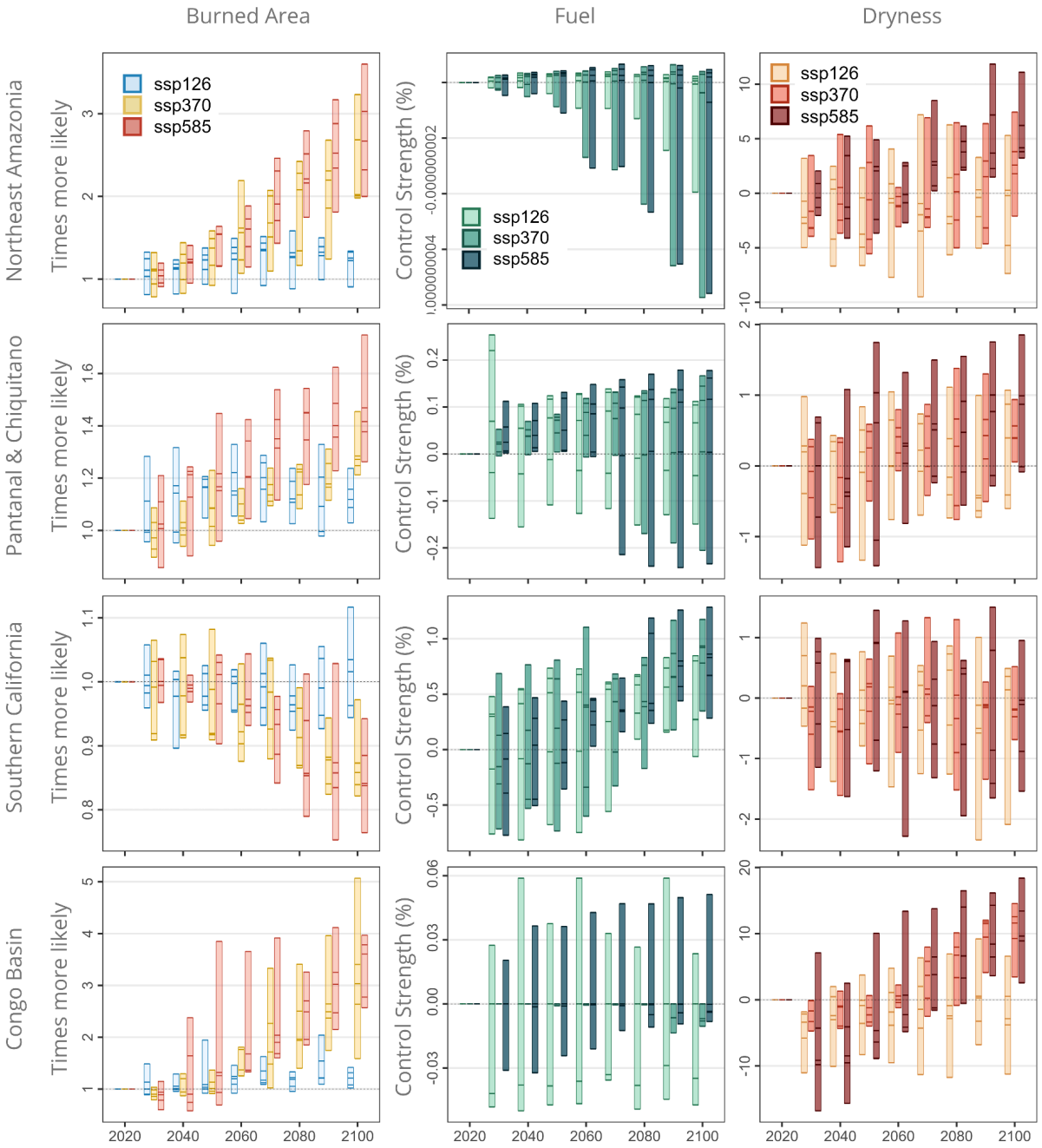

Figure S29: As Figure 18, but for the regions with the highest burned area (at the 95 percentile of burning).

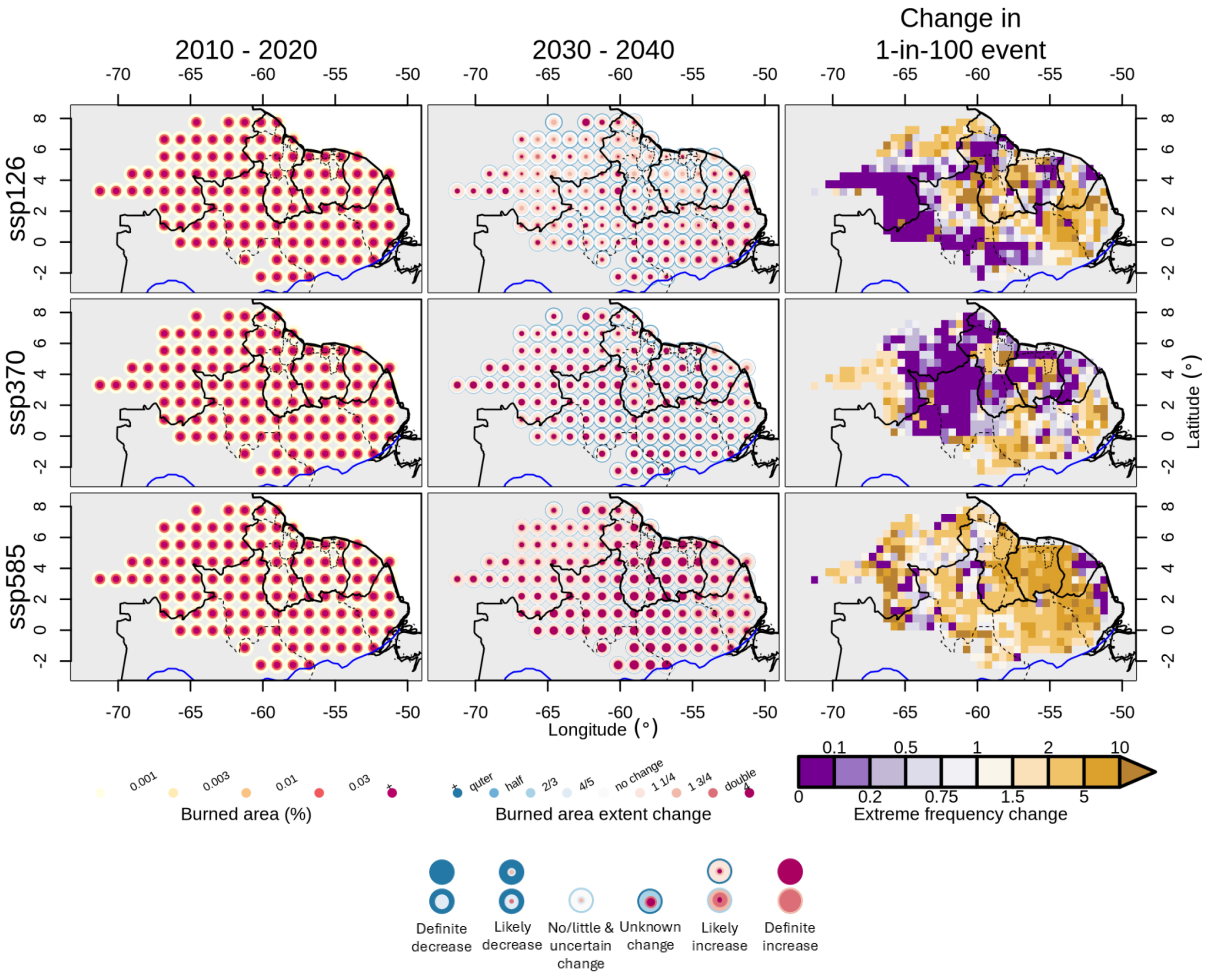

Figure S30: Projected changes in January-March 2024 BA over Northeast Amazonia by 2030–2040 under three SSP scenarios, with BA simulated by ConFLAME. **(Left)** Average JFM BA fraction (%) for 2010–2020. **(Middle)** Relative change in JFM BA extent projected for 2030–2040 period, expressed as a multiplier of 2010–2020 values. **(Right)** Increased (or decreased) frequency in the 2030s period of a 1-in-100 year event defined for the period 2010–2020, expressed as a multiplier of 2010–2020 values. In the left column, the size of the dot in each grid cell indicates the likelihood (larger = higher likelihood) of a BA fraction being greater than the threshold indicated by the coloured dot (see legend at the base). Likewise, in the middle column the size of the dot varies with likelihood that the BA fraction exceeds the threshold indicated by the coloured dot (see legend at the base). For example, a large pale orange dot in the left column indicates a high likelihood of the BA fraction exceeding 0.03%, whereas a small dark red dot indicates a small (but non-zero) likelihood of the BA fraction exceeding 0.03%+.

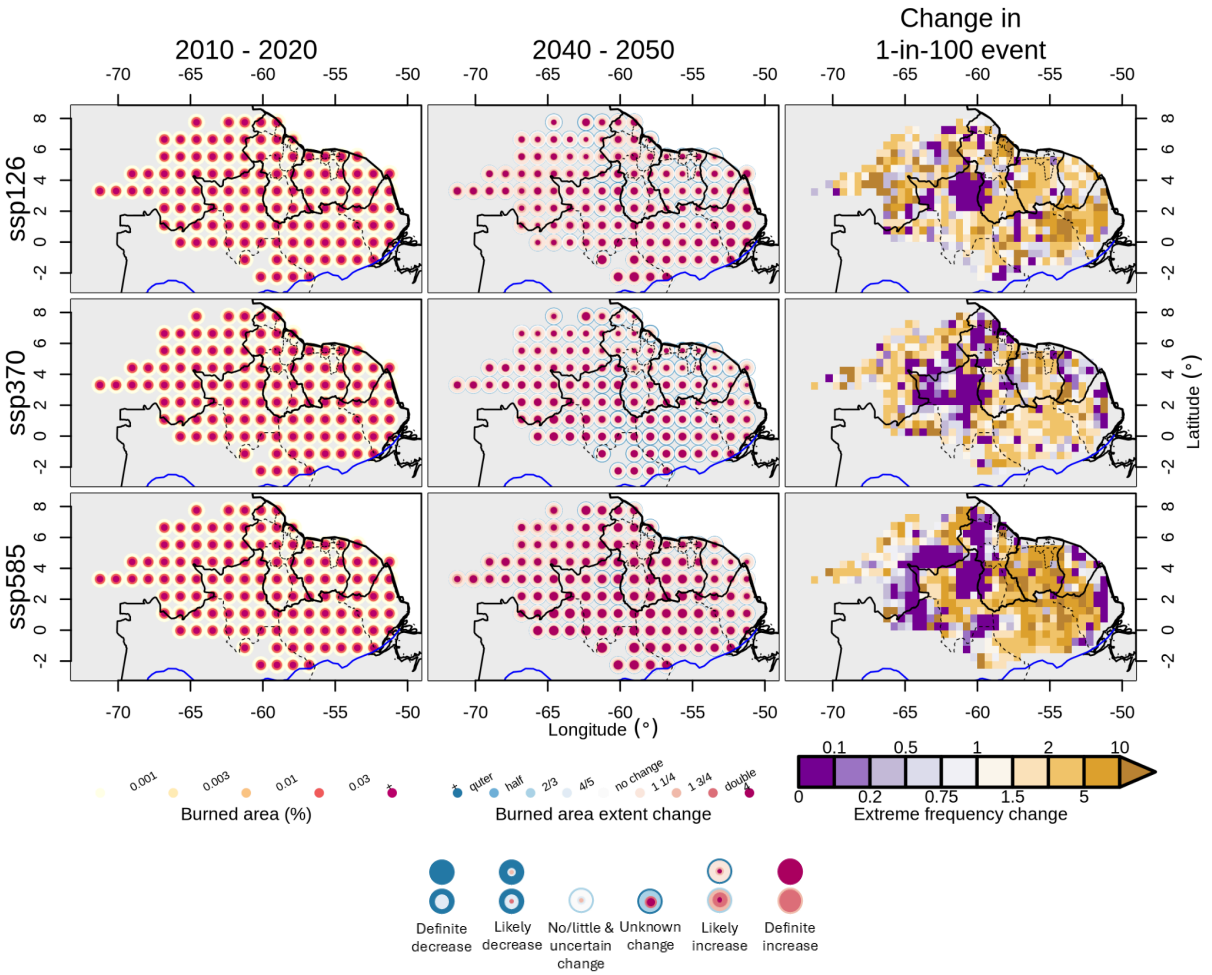

Figure S31: Same as **Figure S30** for 2040s.

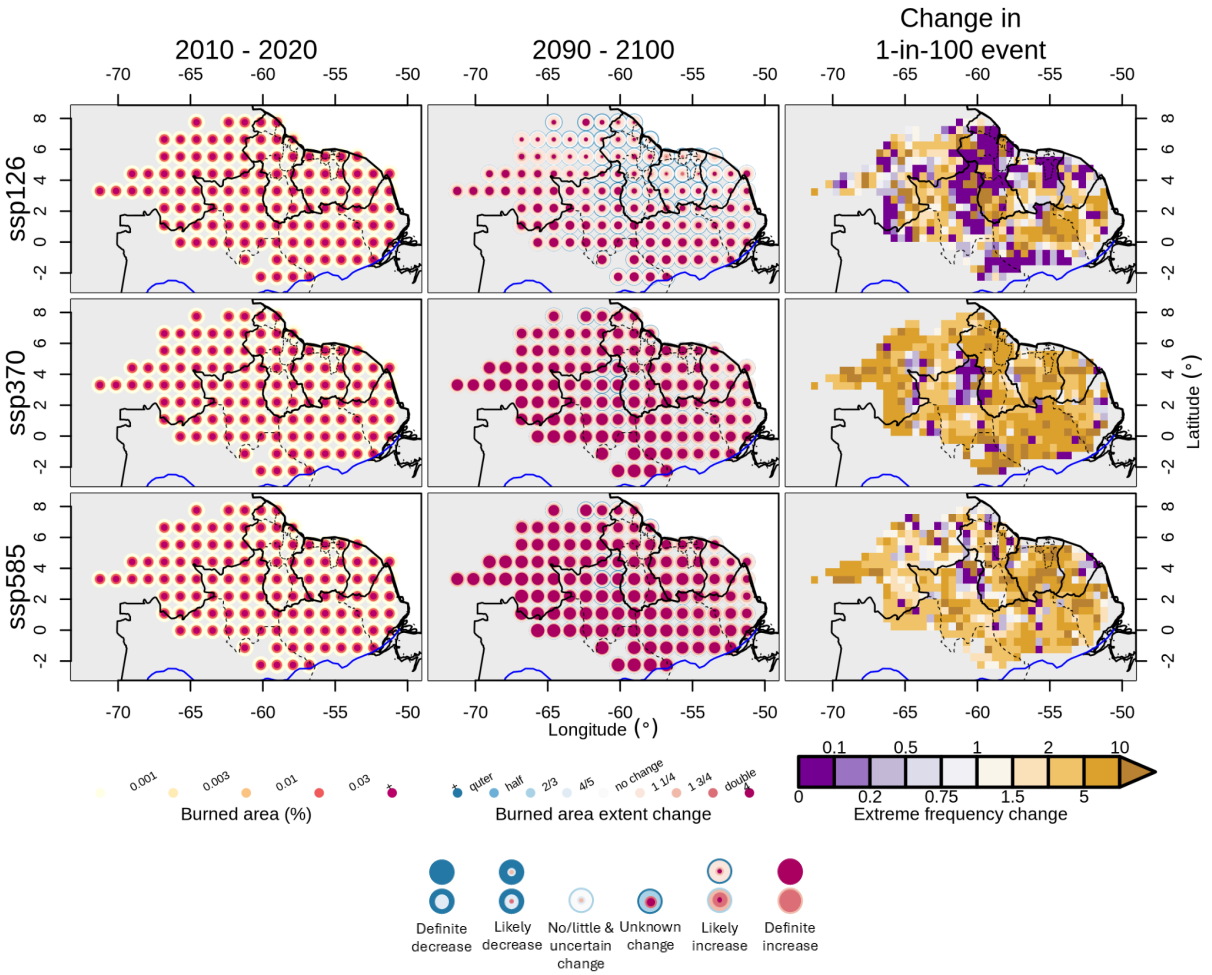

Figure S32: Same as **Figure S30** for 2090s.

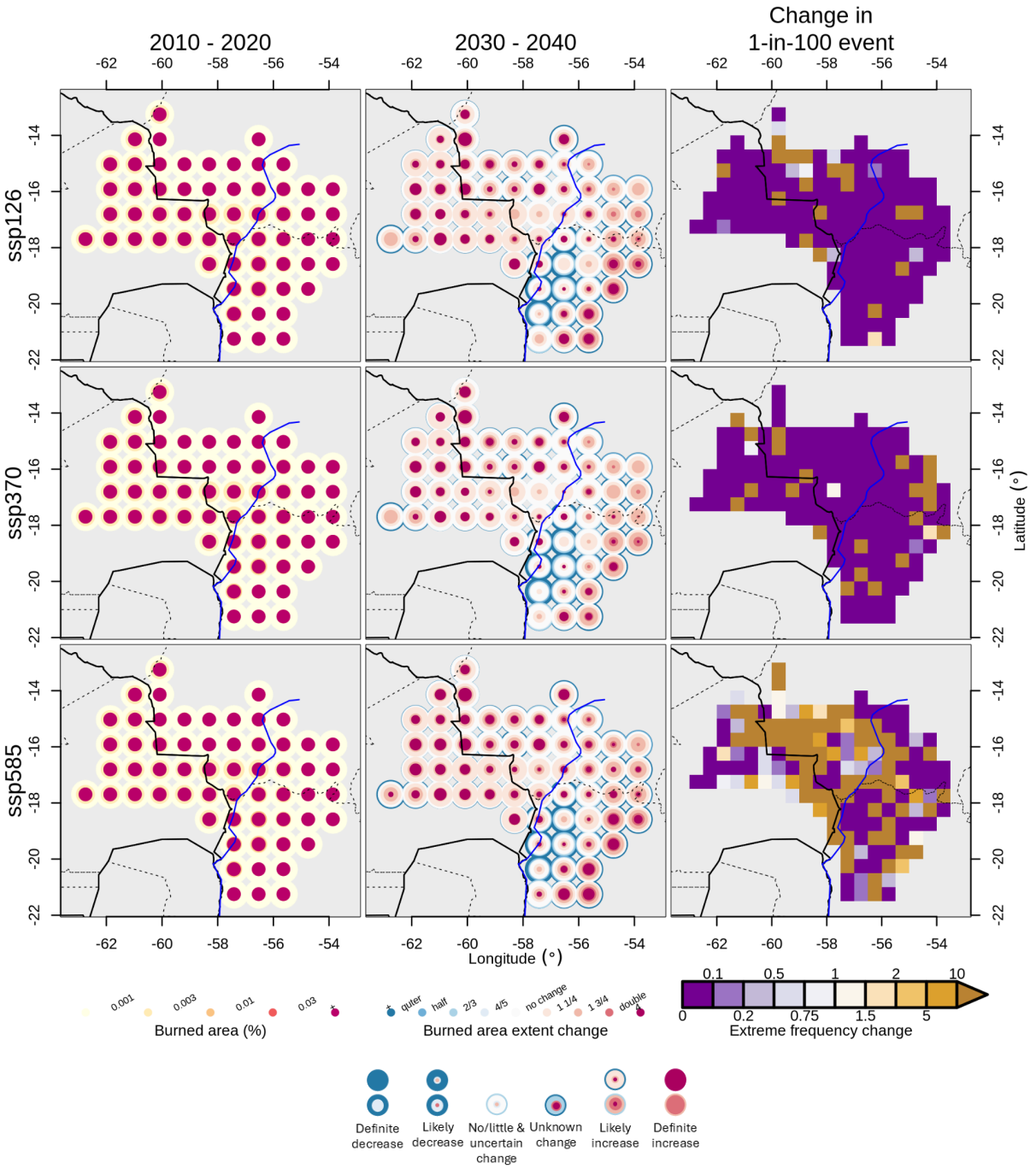

Figure S33: Same as **Figure S30** for August-September 2024, Pantanal and Chiquitano

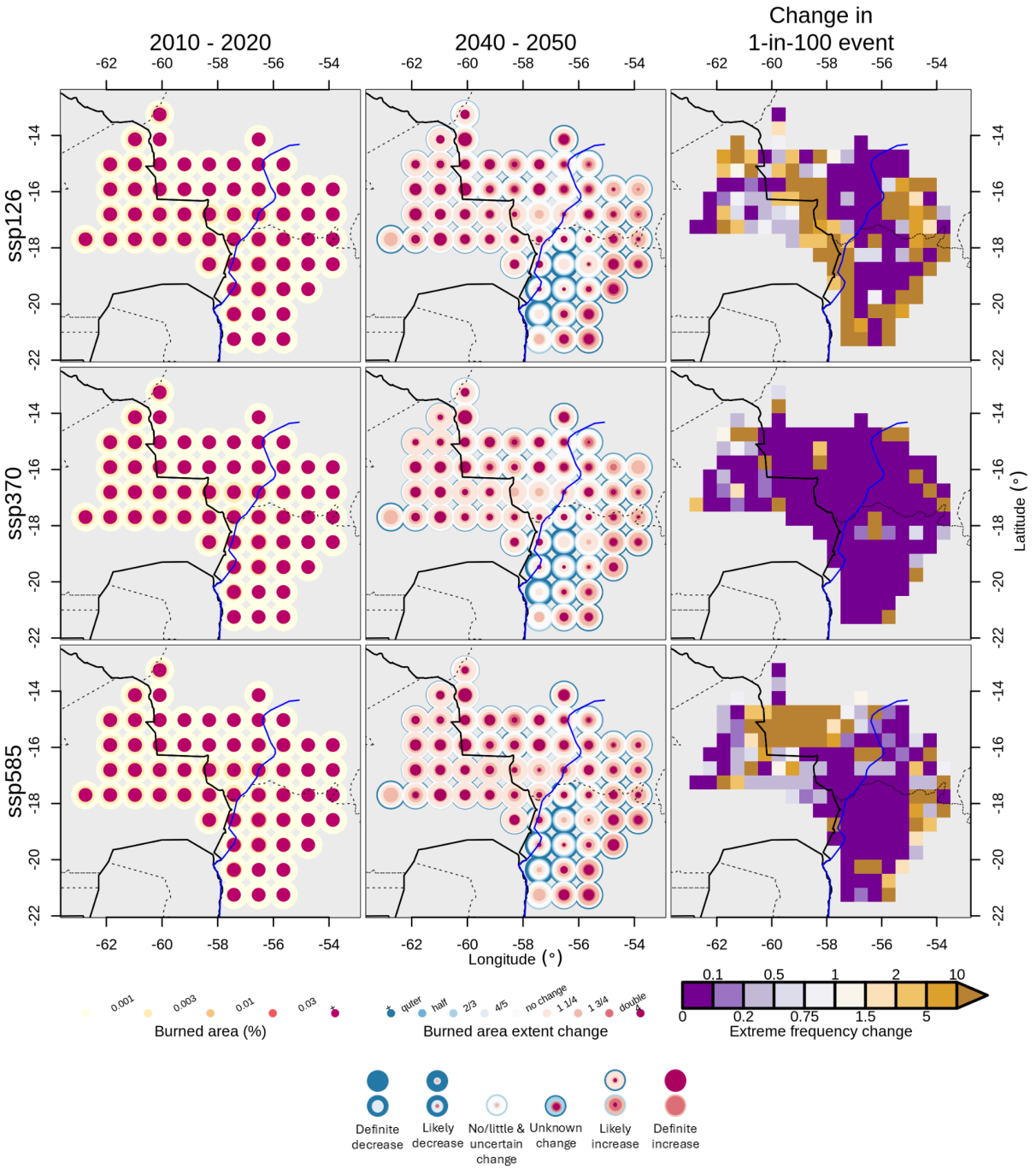

Figure S34: Same as **Figure S30** for 2040s.

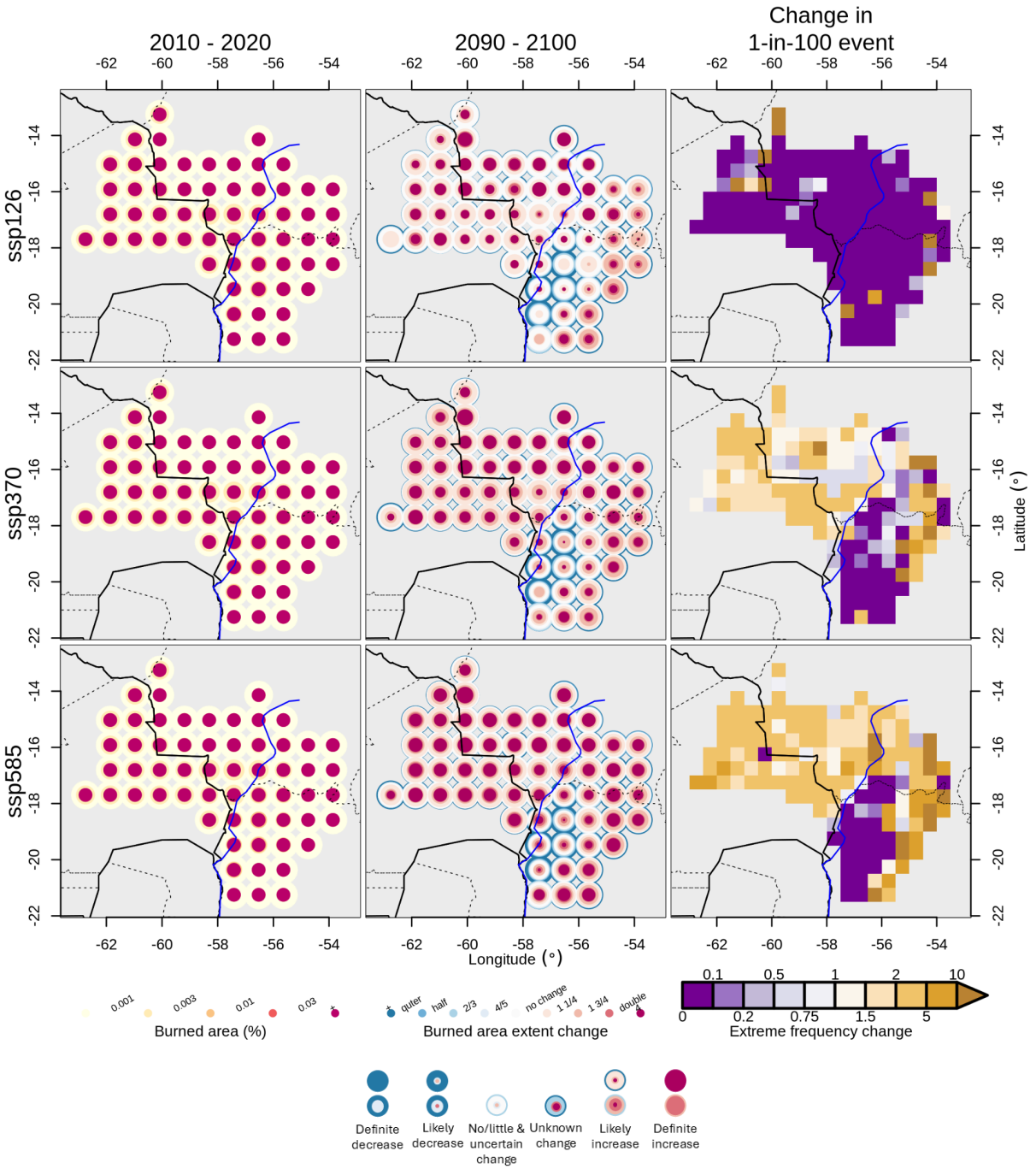

Figure S35: Same as **Figure S30** for 2090s.

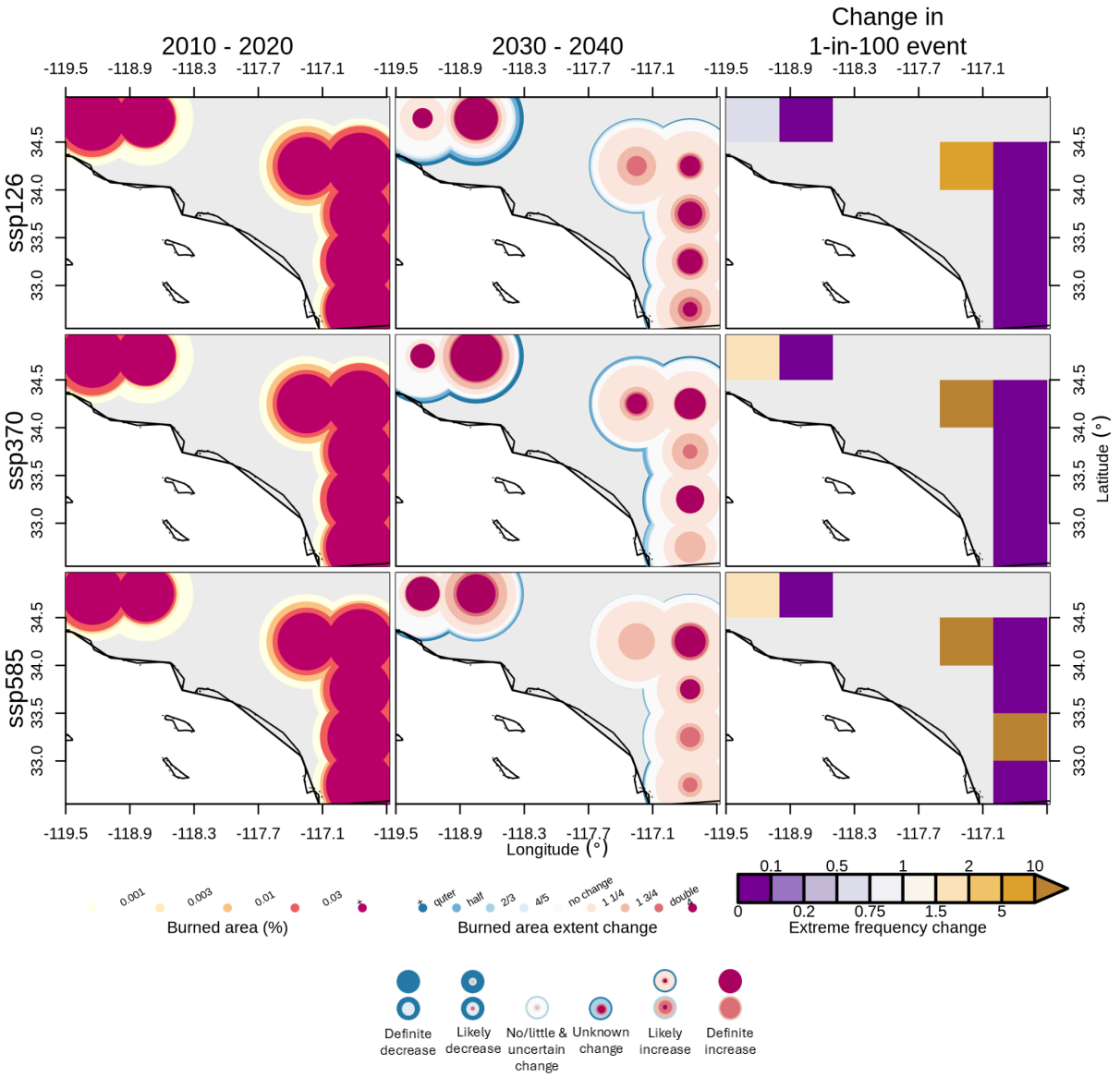

Figure S36: Same as **Figure S30** for July 2025, Southern California

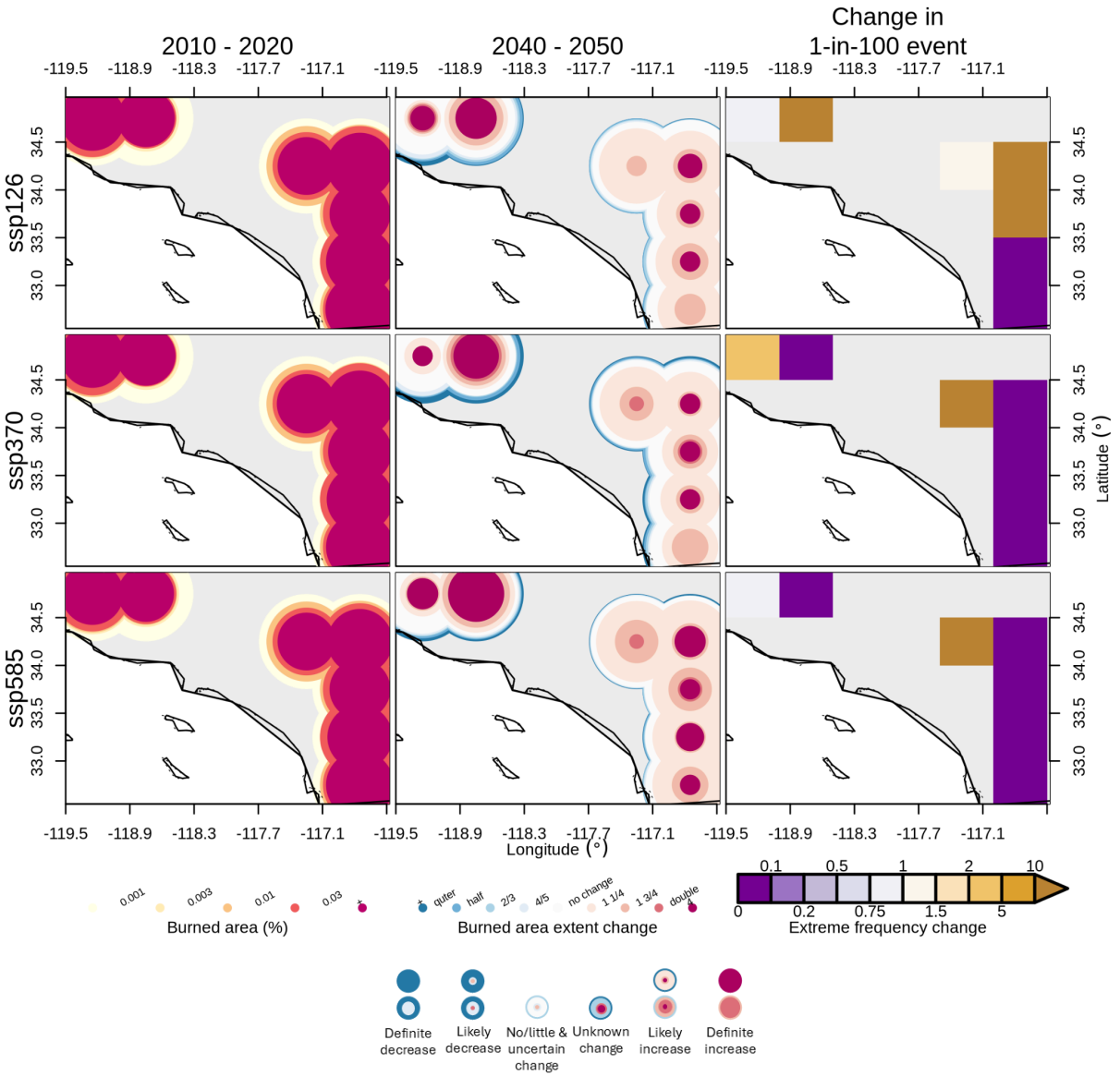

Figure S37: Same as **Figure S36** for 2040s.

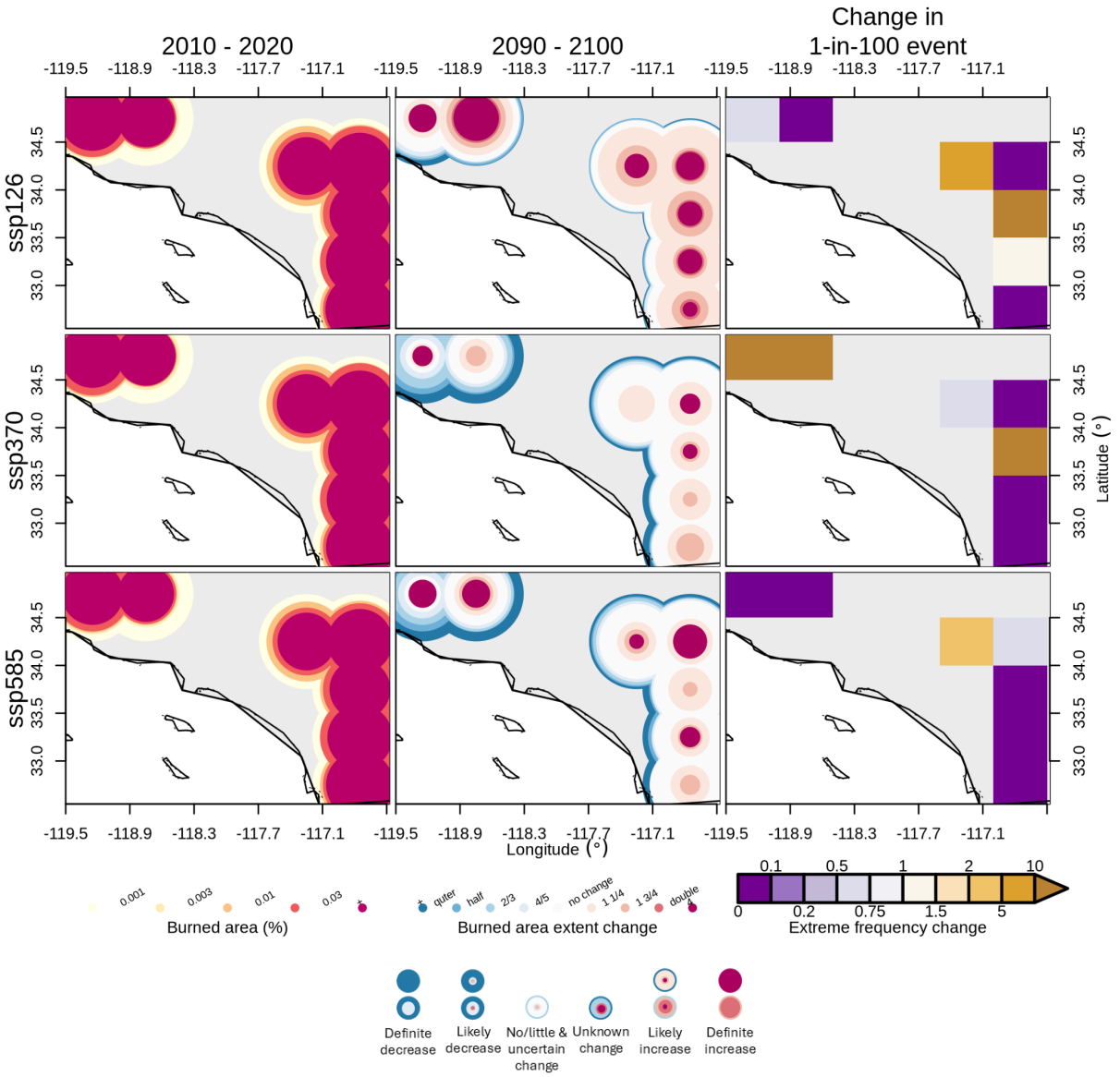

Figure S38: Same as **Figure S36** for 2090s.

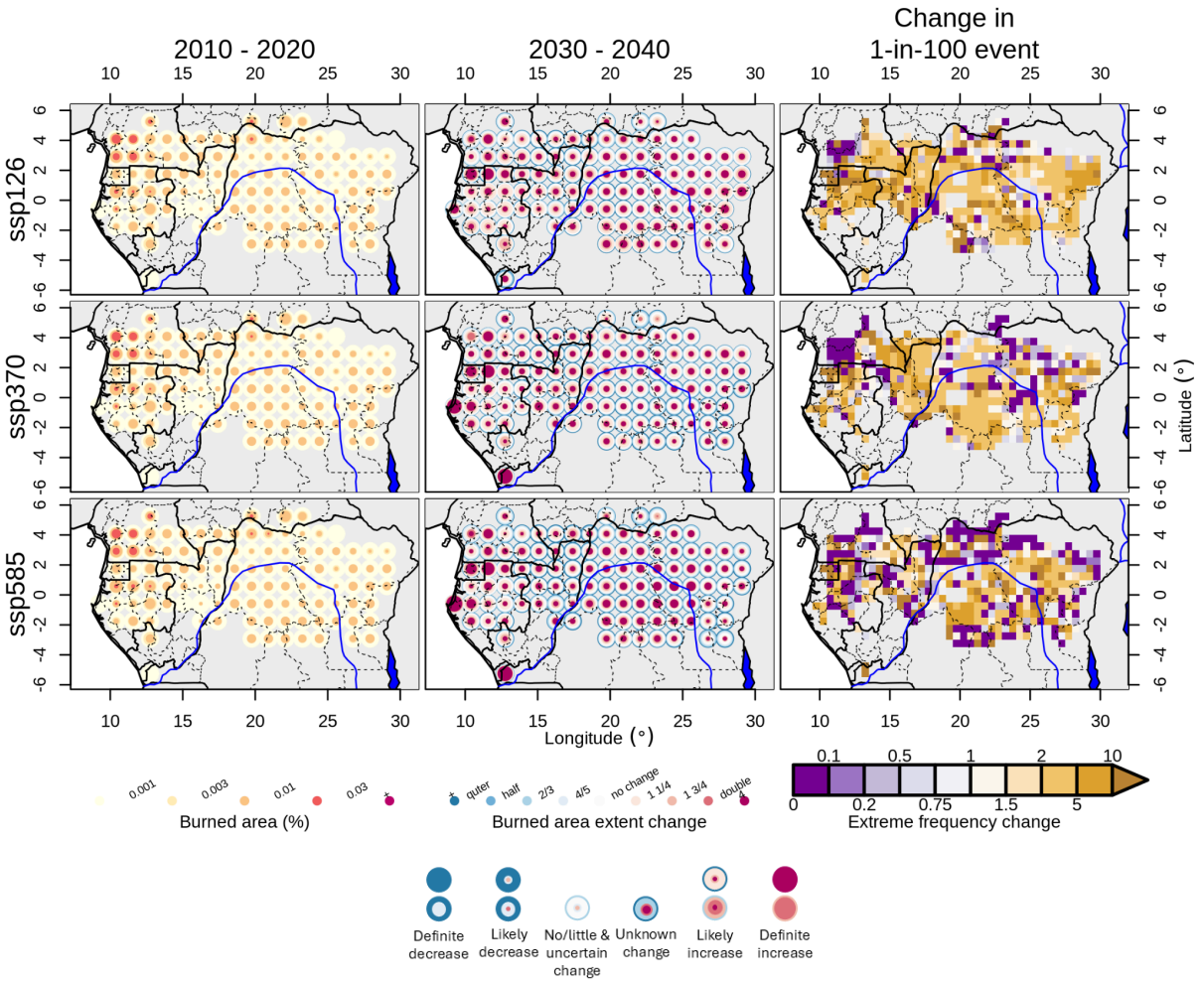

Figure S39: Same as **Figure S30** for July, August 2025, Congo Basin

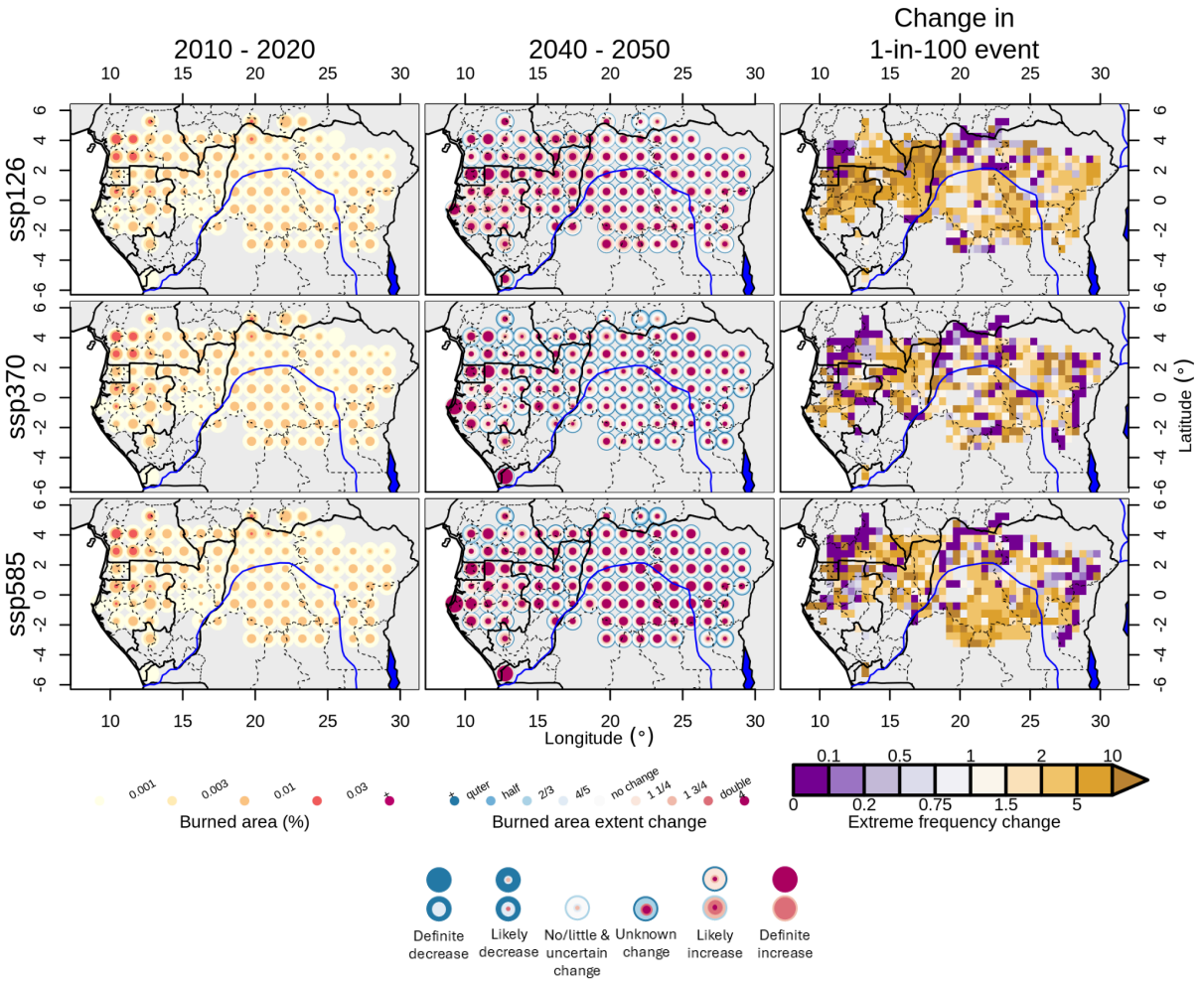

Figure S40: Same as **Figure S39** for 2040s.

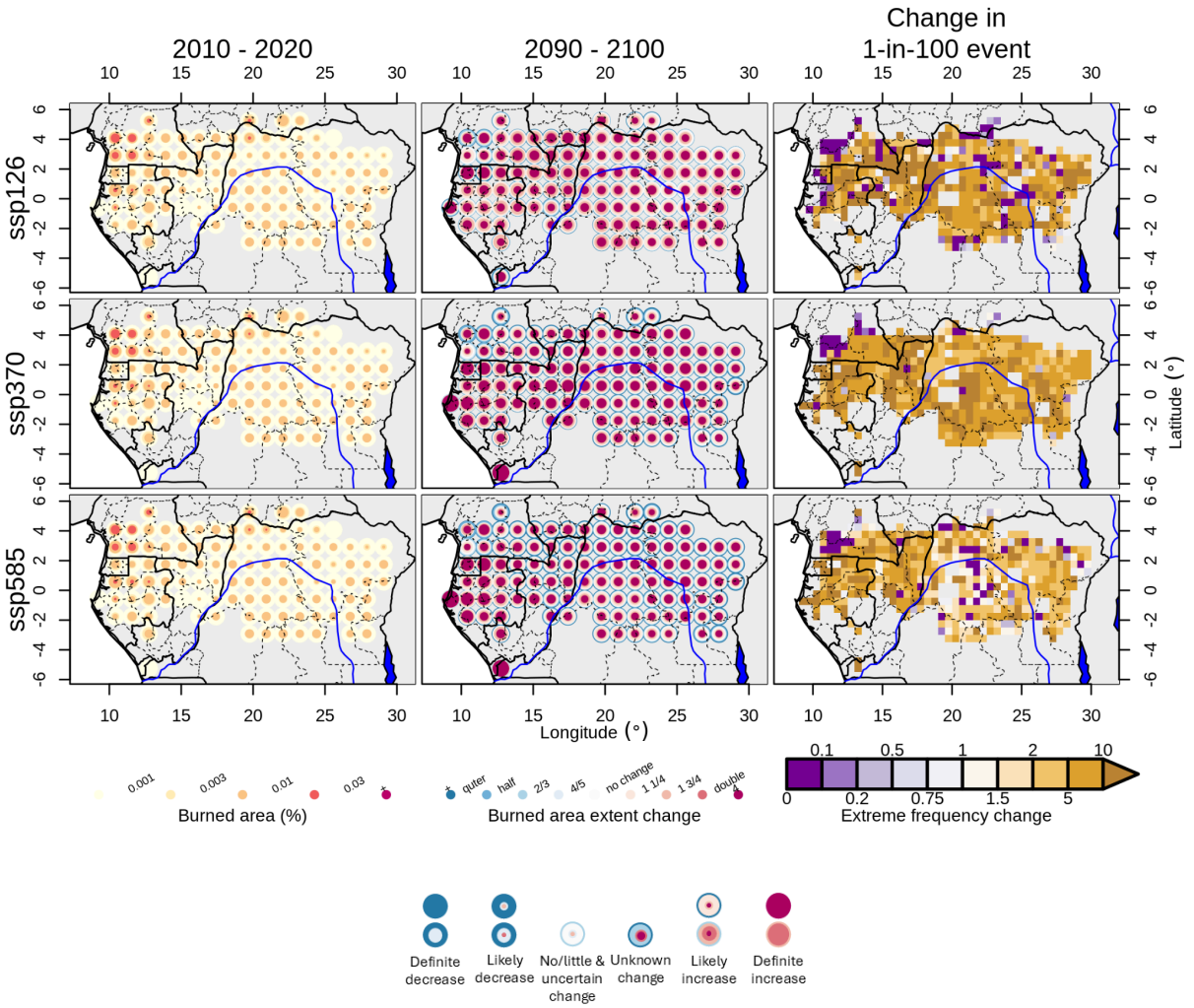

Figure S41: Same as **Figure S39** for 2090s.

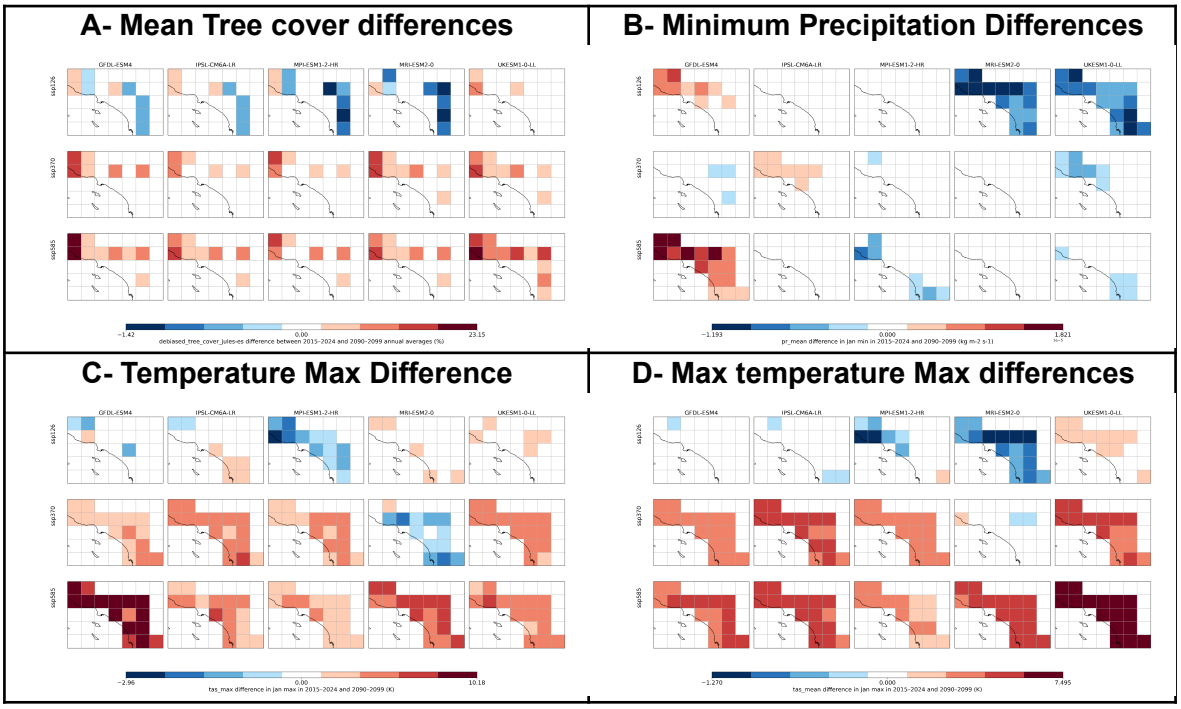

Figure S42 Future projections of key bioclimate drivers of fire for Southern California, expressed as difference 2090s vs 2020s. Panels show (A) mean tree cover differences, (B) minimum precipitation differences, (C) mean maximum temperature differences, and (D) maximum temperature extremes differences.

S6.3 ConFLAME evaluation

We evaluated the performance of bias-corrected ISIMIP3b climate model data against ERA5 reanalysis in estimating the likelihood of extreme burned area (BA) events across four focal regions.

S6.3.1 Northeast Amazonia:

For the baseline period 2010–2020, reanalysis-based estimates indicate a 0.073% annual probability of experiencing a BA extent comparable to January–March 2024 (Table 7). GCM-based estimates yield a slightly higher likelihood of 0.12%. Although bias correction reduced some discrepancies, differences between GCM and reanalysis data persist.

S6.3.2 Pantanal–Chiquitano:

GCM-based estimates suggest a higher present-day likelihood of August–September 2024-level BA (0.08–0.10% annually) than reanalysis data (0.19%). However, for the most impacted areas (top 5% of grid cells), GCMs and reanalysis align more closely, both indicating a very low annual probability of 0.01–0.03%.

S6.3.3 Southern California:

During 2010–2020, the annual likelihood of a 2025-scale regional fire event is estimated at 0.38% from reanalysis and 0.34% from bias-corrected GCMs. In the top 5% most affected grid cells, these estimates are slightly lower (0.27% and 0.24%, respectively). This close agreement highlights the effectiveness of bias correction in aligning model projections with observations, supporting confidence in future risk assessments.

S6.3.4 Basin:

Bias-corrected GCMs closely replicate reanalysis estimates for July 2024-scale fire events, with annual likelihoods of 0.16–0.19% (GCMs) and 0.17% (reanalysis). For the most severely affected areas, both data sources agree on an annual likelihood near 0.01%, indicating strong model fidelity to observed fire risk patterns.

S8 Supplementary Material for Appendix A

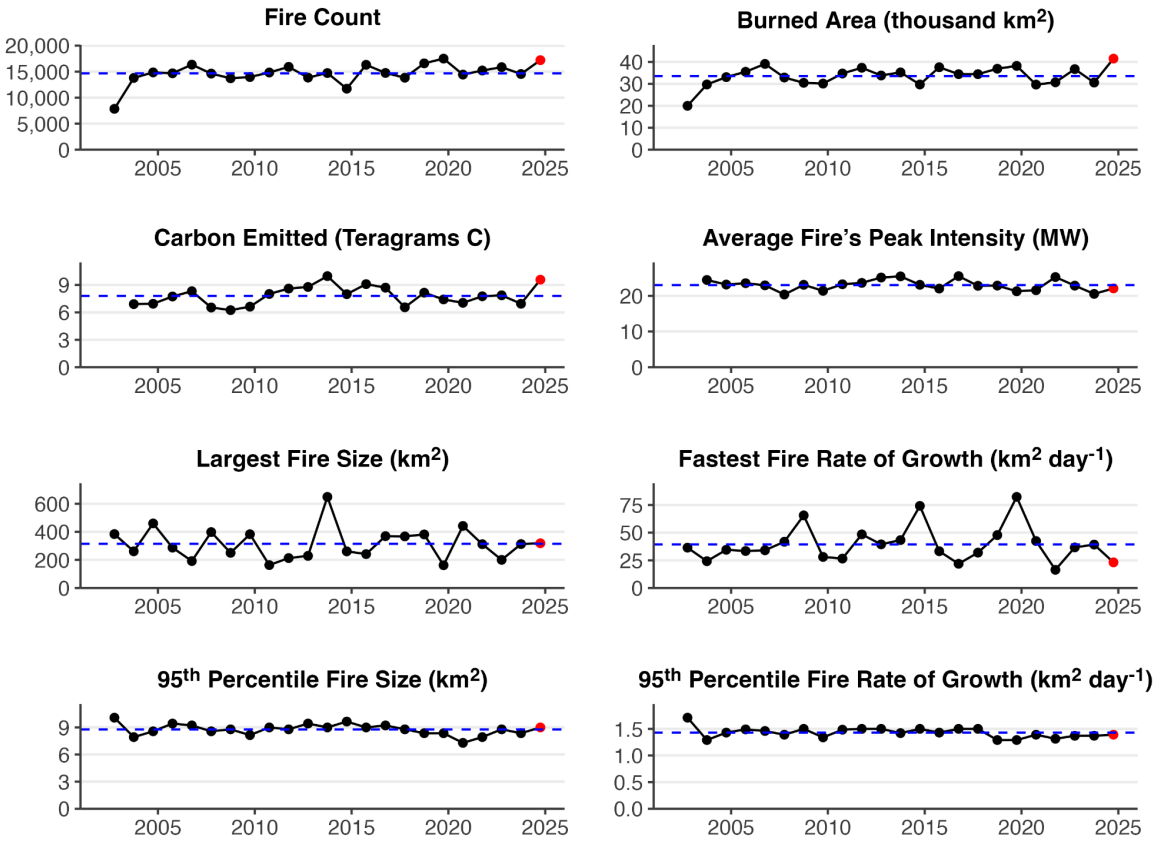

Figure S43: Summary of the 2024-2025 fire season in the Republic of the Congo. Time series show annual fire count, BA, C emissions totals within the region, as well as the average fire's peak fire intensity (95th percentile value of fire radiative power within fire perimeters), the 95th percentile fire size, fastest daily rate of growth, and 95th percentile fire daily rate of growth. Black dots show annual values prior to the latest fire season, red dots the values during the latest fire season, and blue dashed lines the average values across all fire seasons.

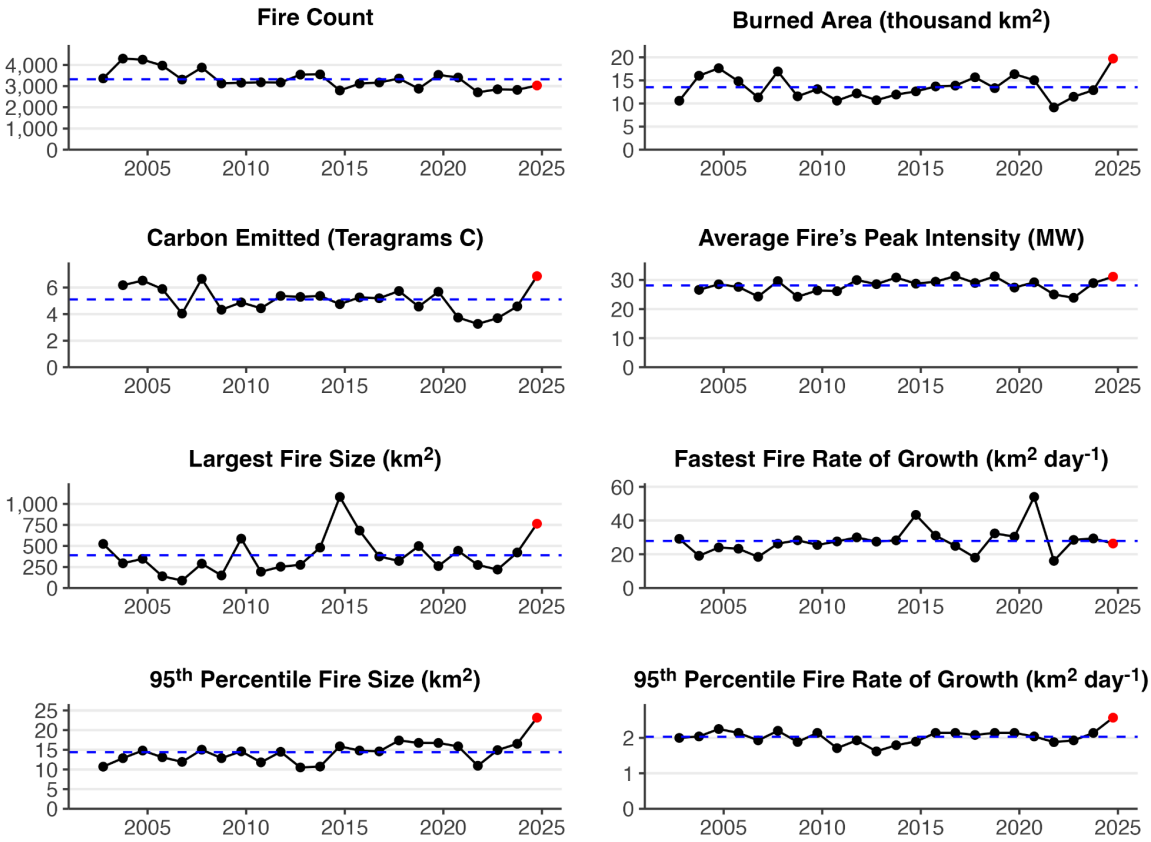

Figure S44: Summary of the 2024-2025 fire season in Huíla, Angola, as in Figure A1.

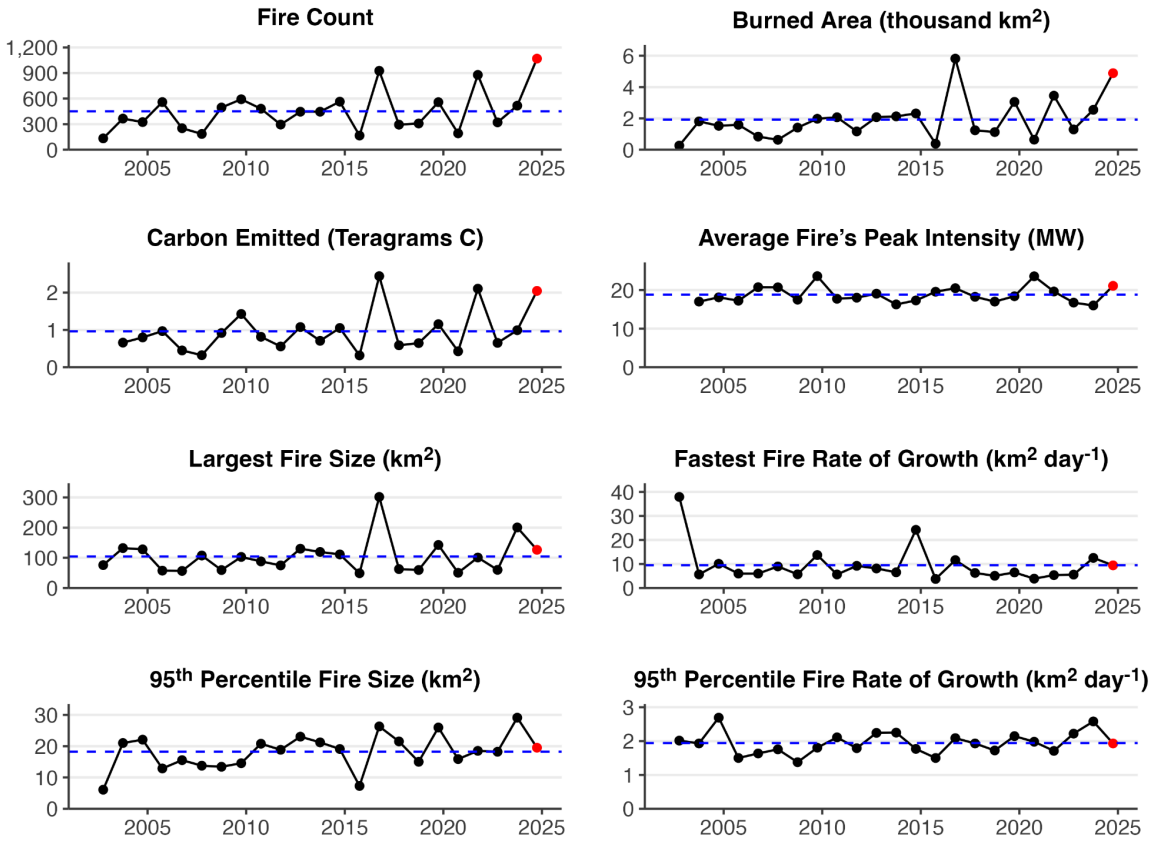

Figure S45: Summary of the 2024-2025 fire season in Nepal, as in Figure A1.

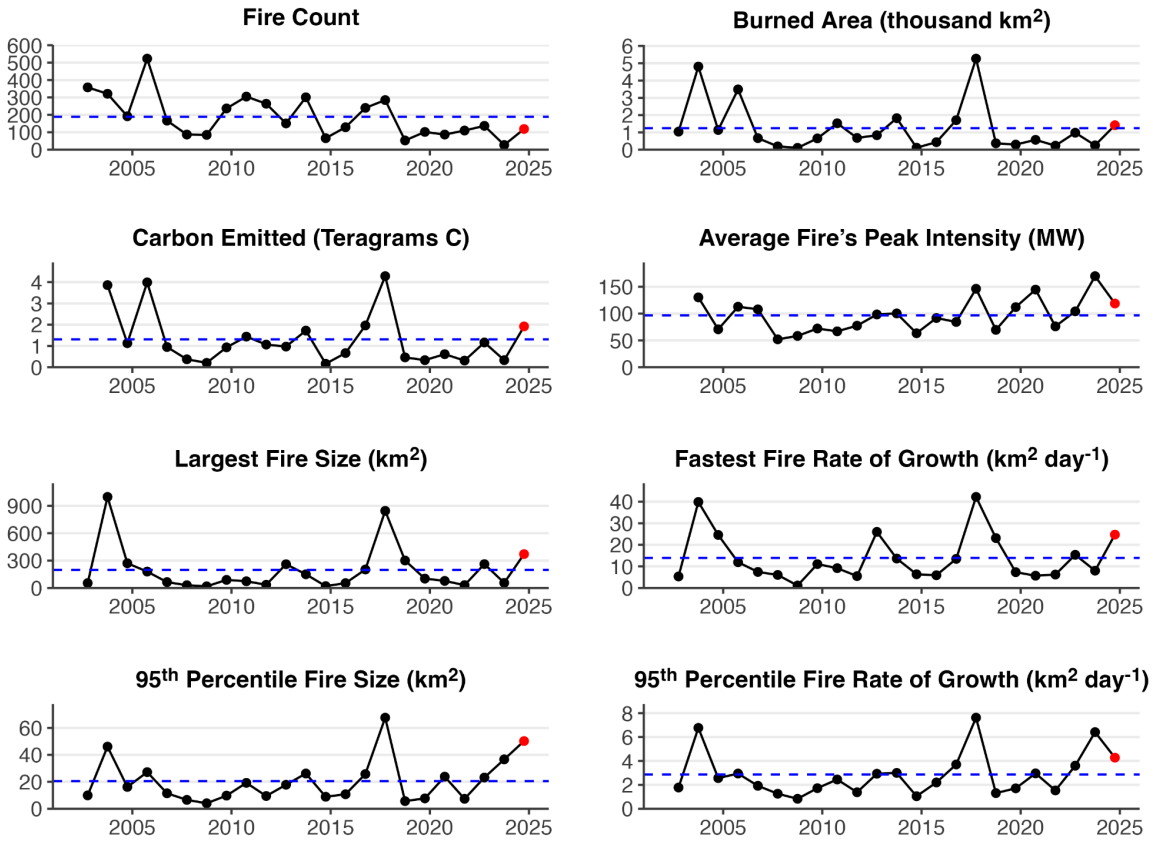

Figure S46: Summary of the 2024-2025 fire season in Portugal, as in Figure A1.

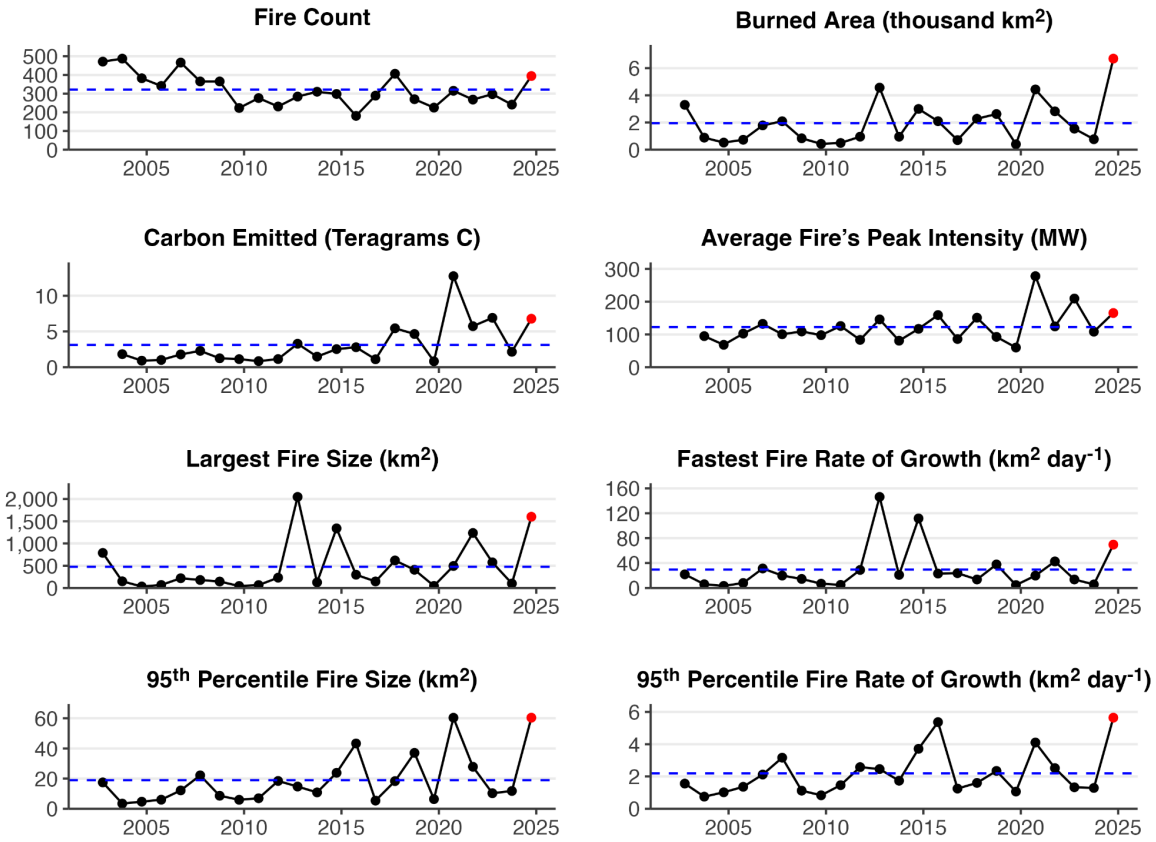

Figure S47: Summary of the 2024-2025 fire season in Oregon, USA, as in Figure A1.

S9 Supplementary Material: Extended Model evaluation

S9.1 ConFLAME evaluation - driver assessment

We evaluate the performance of ConFLAME following the Bayesian attribution model evaluation framework introduced by Barbosa et al. (2025) and applied in last year's report. The aim of this evaluation is to ensure that the posterior distribution adequately represents the observed fire record in each case-study region, a necessary precondition for robust attribution.
Specifically, we test two criteria:

1. Coverage of observations – the observed burned area (BA) should fall within the posterior uncertainty range (5th–95th percentiles) of the model simulations.

2. Lack of systematic bias – observed values should not cluster consistently at one edge of the posterior distribution. An unbiased model will show observations distributed around the median posterior, with an expected average rank position of ~0.5.

We present three diagnostic panels for each region:

- Top row: Annual mean BA for December–February in observations, and the 5th and 95th percentiles of the posterior simulations, to assess spatial coverage of the observed distribution.

- Middle row: (i) scatter of observed BA versus its likelihood under the posterior (where high observed BA should have high likelihood, >0.9, if extremes are well represented); (ii) spatial maps of the 5th and 95th percentiles of likelihood across all months.

- Bottom row: (i) scatter of observed versus simulated BA, with posterior uncertainty shown as vertical ranges (5th, interquartile, and 95th percentiles); (ii) map of the average rank position of observations within the posterior (ideal ≈0.5); and (iii) map of the probability that deviations from 0.5 are statistically significant, indicating bias.

Equations for the likelihood and rank-position diagnostics are given in Barbosa et al. (2025).

We use the same model configuration outlined in **Section 4.1.2** and **Supplementary Section 4.1.2**. Due to constraints on the time period of available data, we performed training and evaluation over 2019-2026, with 50% of grid cells used for training and 50% for evaluation.

S9.1.1 Northeast Amazonia

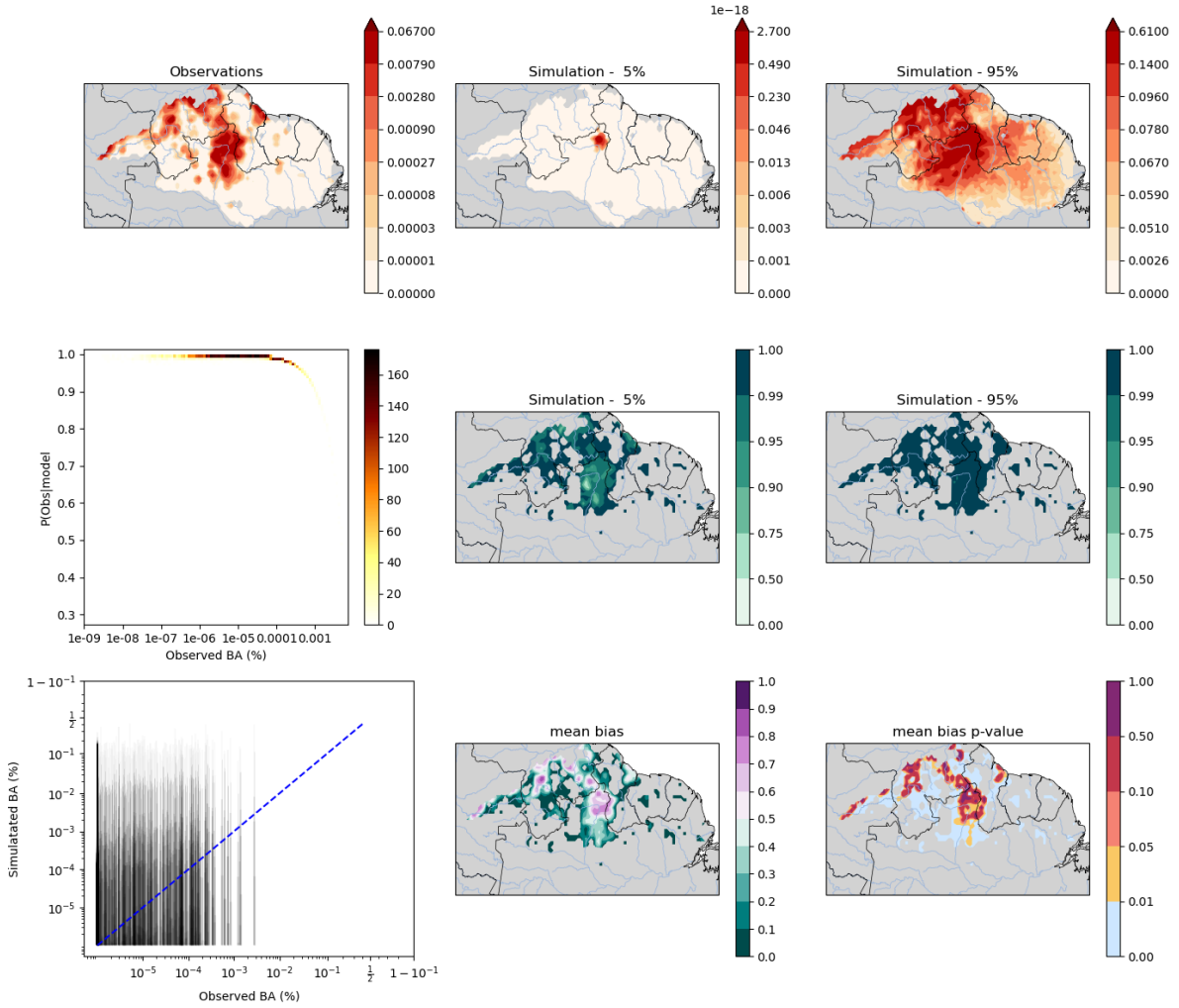

Figure S48: Posterior evaluation diagnostics for ConFLAME in Northeastern Amazonia. Each panel shows three sets of diagnostics. Top row: Observed annual average BA for Focal Months (left), compared to the 5th (middle) and 95th (right) percentiles of simulated BA. Middle row: Scatterplot of observed BA (x-axis) versus likelihood of observations under the posterior (y-axis), where high observed BA should correspond to high likelihood values; spatial maps of the 5th (middle) and 95th (right) percentiles of observation likelihood across all months. Bottom row: Scatterplot of observed BA (x-axis) versus posterior-simulated BA (y-axis), with vertical ranges representing the 5th percentile, interquartile range, and 95th percentile; a map of the average posterior rank position of observations (ideal ≈0.5); and a map of the significance of deviations from 0.5, indicating where bias may be present.
The observed burned area (BA) during January–March is concentrated mainly in the northern Amazonian savannas and in the transitional dry-forest zone to the north of the region, with a mean monthly BA of approximately 0.067 (fractional area burned). The posterior ensemble from the model reproduces these core burning regions well, although it extends elevated BA slightly into more forested areas along the Brazil–Venezuela border. This spatial shift corresponds to locations where satellite observations likely underestimate BA because of persistent cloud cover and tree-canopy interference.

Following the evaluation approach of Barbosa et al. (2025), we assess both the coverage of the observed values by the posterior and the lack of systematic bias in their placement within it. Across Northeastern Amazonia, the posterior shows high consistency with observations: the probability of the observed value given the model, P(Obs | Model), exceeds 0.95 for nearly all grid cells. Observed BA values fall comfortably within the posterior uncertainty range, including for the most extreme events, with the top 10 % of observed BAs aligned, on average, with the 79th percentile of the posterior distribution. This demonstrates that the model captures both the spatial pattern and magnitude of historical extremes, providing a strong basis for subsequent attribution analysis in this region.

S9.3.2 Pantanal and Chiquitano

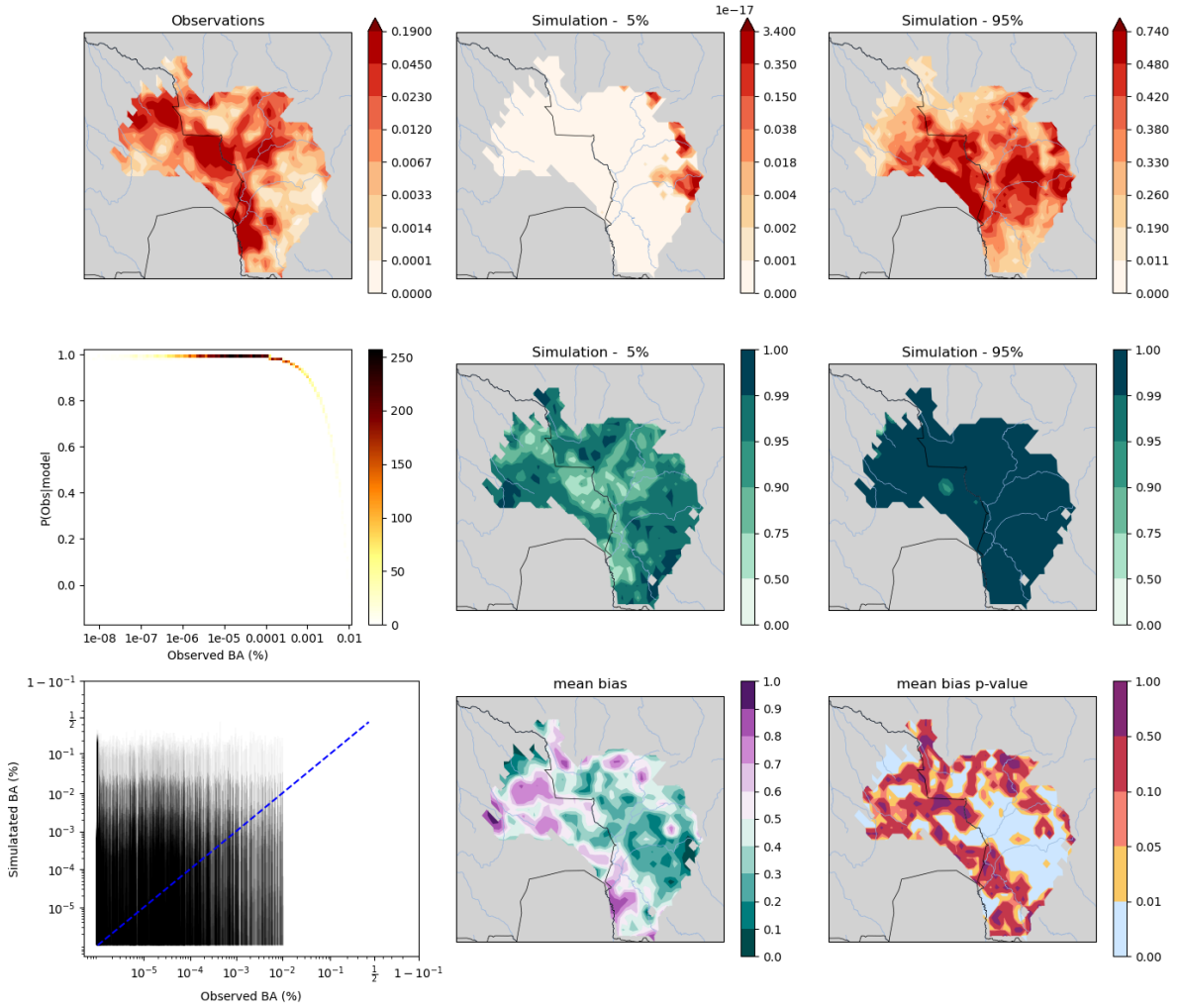

Figure S49: Observed burned area (BA) peaks across the Bolivian dry forests of the Chiquitano region, with extensive burning also evident in the adjacent Brazilian Pantanal wetlands. The model reproduces this broad spatial pattern within its posterior, though it does so primarily through a wide uncertainty range. Some mismatches remain in the wetlands and southern Chiquitano areas, where observed burning is less strongly expressed in the posterior mean. Nevertheless, the observed BA consistently falls within the posterior range, indicating that the model adequately represents historical variability even in these more heterogeneous landscapes.

Across most of the region, the probability of the observed value given the model, P(Obs | Model), remains high (typically >0.85), though it dips below 0.75 for some months in wetter or more topographically complex areas. The most extreme observations also lie within the posterior, averaging at the 87th percentile, suggesting a modest regional underestimation of absolute BA magnitudes, but with the relative ranking of years and locations well captured (as shown by the observed–simulated scatter). Together, these results indicate that while the posterior is broad, it successfully captures the spatial and interannual structure of fire activity required for robust attribution analysis.

S9.3.3 Southern California

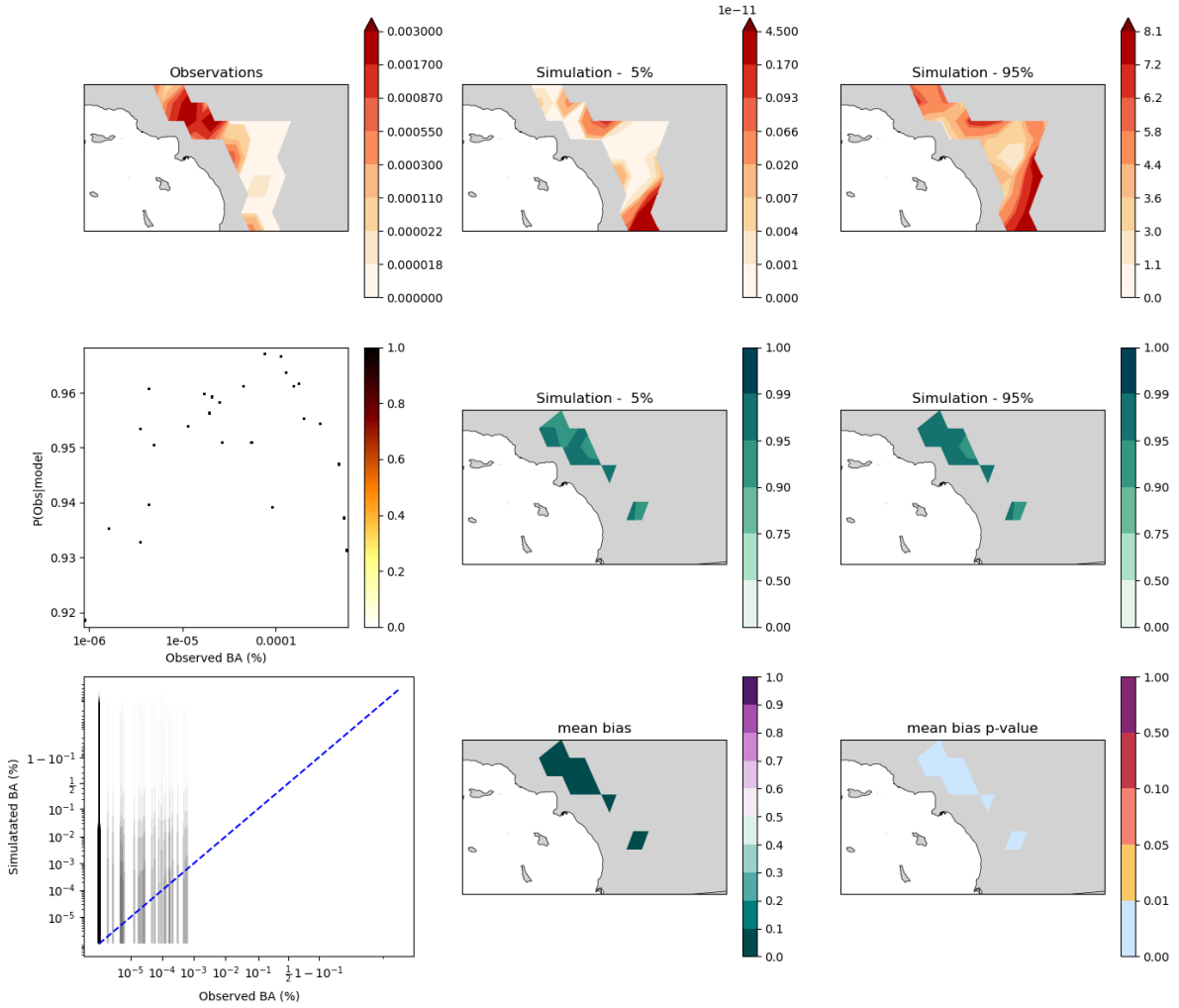

Figure S50: The 2025 Los Angeles fires produced the highest burned area (BA) observation in the record, concentrated in the northern part of the region, where the 10-year mean BA reached ~0.3%. The model posterior captures this hotspot, but also indicates that, given the training data, elevated BA is plausible in the southern portion of the region. Posterior uncertainty ranges are wide in both sub-regions, spanning from negligible burning to values of 1–10% BA. Despite this spread, the probability of the observed values under the posterior, P(Obs|Model), is very high (>0.92) across the region. Observations fall predominantly within the central mass of the posterior distributions, though with a slight tendency toward underestimation at the upper extreme (observations align, on average, with the 60th

percentile of the posterior for the most extreme events, i.e. 99–100% quantiles). This mild bias remains within acceptable limits according to the criteria of Barbosa et al. (2025), supporting the conclusion that the posterior adequately represents both the central tendency and extreme tail of the observed distribution in Southern California.

S9.3.4 Congo Basin

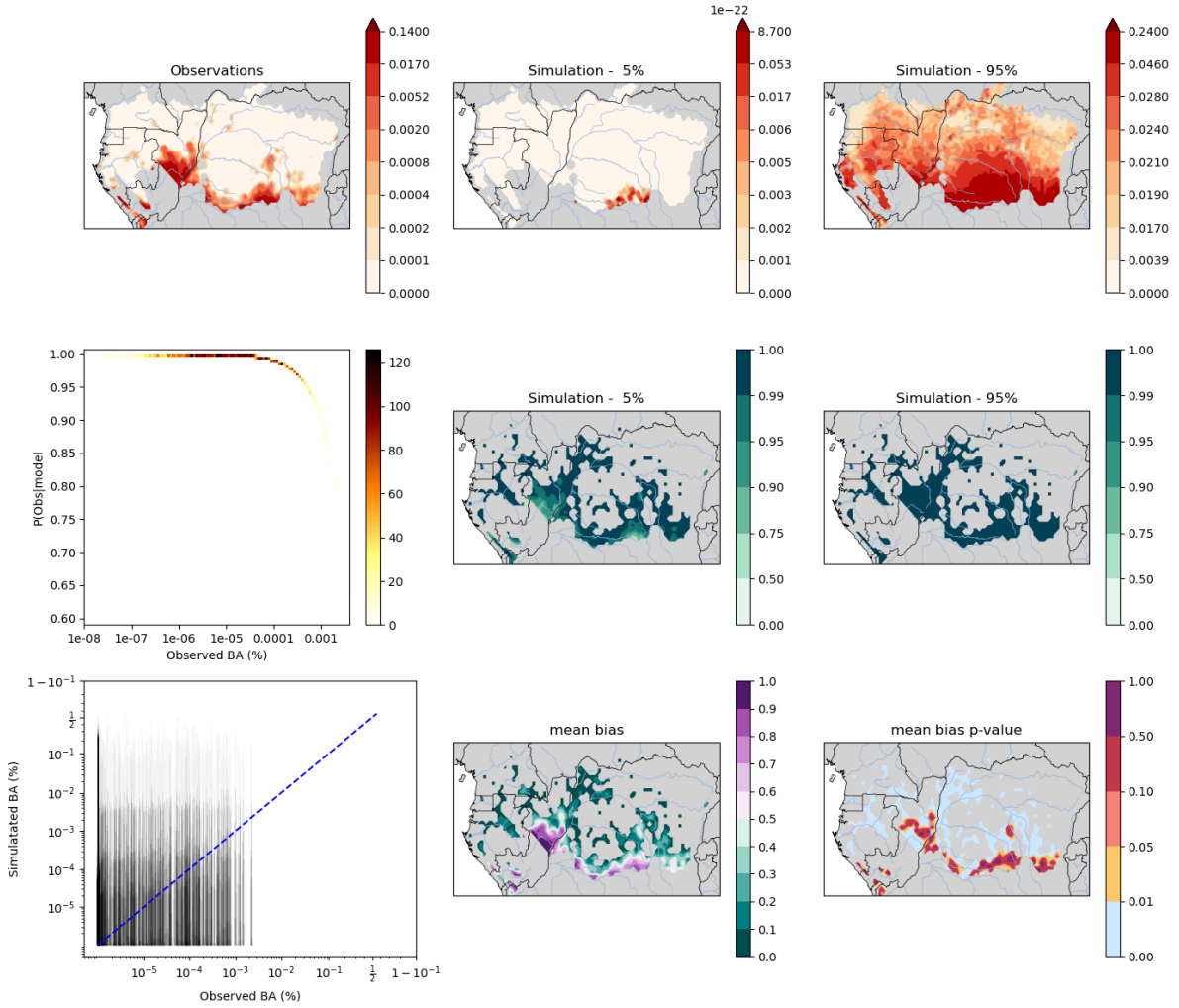

Figure S51: Observed burned area (BA) is concentrated toward the southern margin of the basin, spanning both Congos and extending westward toward the Atlantic coast. This region corresponds to the drier savanna–forest mosaic that experiences seasonal burning, contrasting with the largely unburned central rainforest core. The model's posterior reproduces this spatial pattern well, indicating strong sensitivity to the same climatic and vegetation gradients that shape observed fire activity. It also suggests that burning may extend slightly further into forested areas, consistent with regions where satellite observations are known to underestimate low-intensity or short-lived fires beneath partial canopy cover.

Across nearly the entire region, the probability of the observed value given the model, P(Obs | Model), exceeds 0.9, indicating excellent agreement between simulated and observed burned area magnitudes. Observations consistently fall within the simulated posterior range, including at higher burned area levels. The most extreme observed events (top 10%) occur, on average, at the 82nd percentile of the posterior, suggesting a modest underestimation of the highest-intensity burning. Nonetheless, the posterior captures both the spatial gradients and interannual variability in burned area across the southern Congo Basin, supporting its suitability for attribution analysis.

S9.2 ConFLAME evaluation - Near Real Time

S9.2.1 HadGEM3-A vs ERA5 meteorology

In this section we present a basic evaluation of the model's performance against ERA5 reanalysis for the physical input variables to the FWI. As the FWI methodology requires a bias correction of the FWI itself, rather than of the input variables, we focus here on assessing the basic physical behaviour of and relationship between those variables. Figures S48- S55 present time series for a number of recent years followed by details of the seasonal cycle over 2024. From these we are able to qualitatively assess the behaviour over these timescales to that in reanalysis, compare any obvious anthropogenic responses to the response to only natural climate forcings and note any clear biases.

Temperature variables typically possess better model performance than those related to precipitation, humidity and wind. For all regions we see that daily mean and maximum temperature possess similar magnitude of variability, absolute values and presence of obvious trends to ERA5. The Amazon and Congo regions see model daily means that are warm biased while daily maximum temperatures are essentially unbiased in all regions, at the relevant part of the seasonal cycle, which is useful for FWI as maximum temperature is the relevant input variable. Temperature is the only variable with significant trends that are obvious over the short period depicted (Congo) but we see that the model captures these, as well as the lack of such in other regions.

For each region the model captures the phasing of the seasonal cycle in precipitation, despite clear biases in magnitude of extremes of the monthly mean. Daily mean surface wind also possess seasonality with features that are captured by the model, generally with high biases. RH anomalies appear to possess both significantly different magnitude of variability and seasonality in more than one region. Together with temperature however these suggest that the appropriate physical relationships between the input variables is present in the model and that the basic meteorology relevant to fire weather events is acceptable.

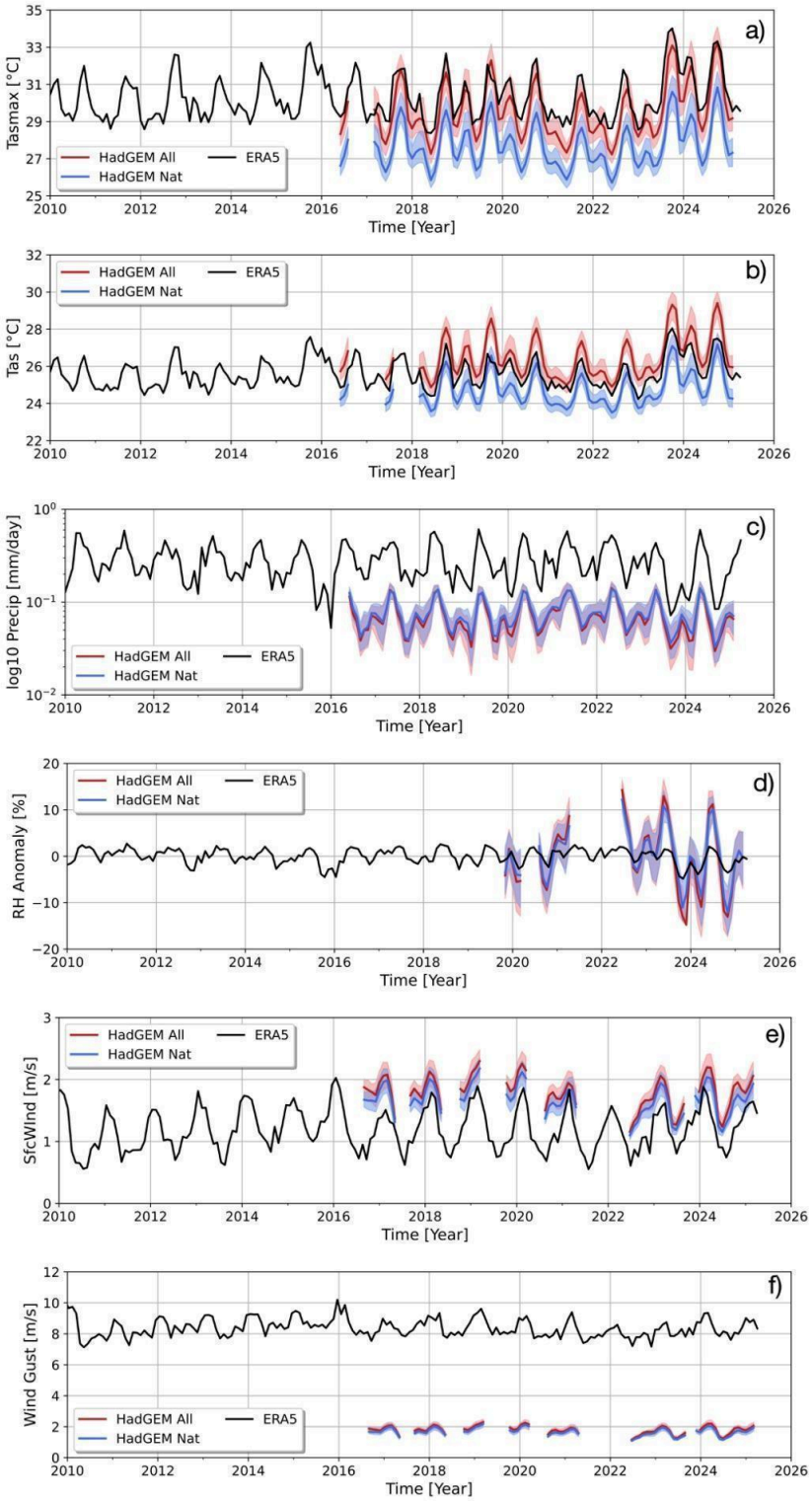

Figure S52: January 2010 to April 2025 time series of individual component variables of the FWI from HadGEM (red: all forcing scenario, blue: natural forcing scenario) compared to ERA5 reanalysis (black) over northeast Amazonia region. We show monthly mean a) daily maximum temperature, b) temperature, c) total precipitation, d) relative humidity, e) wind speed as well as f) wind gusts. Shading represents the 5th-95th percentile confidence interval.

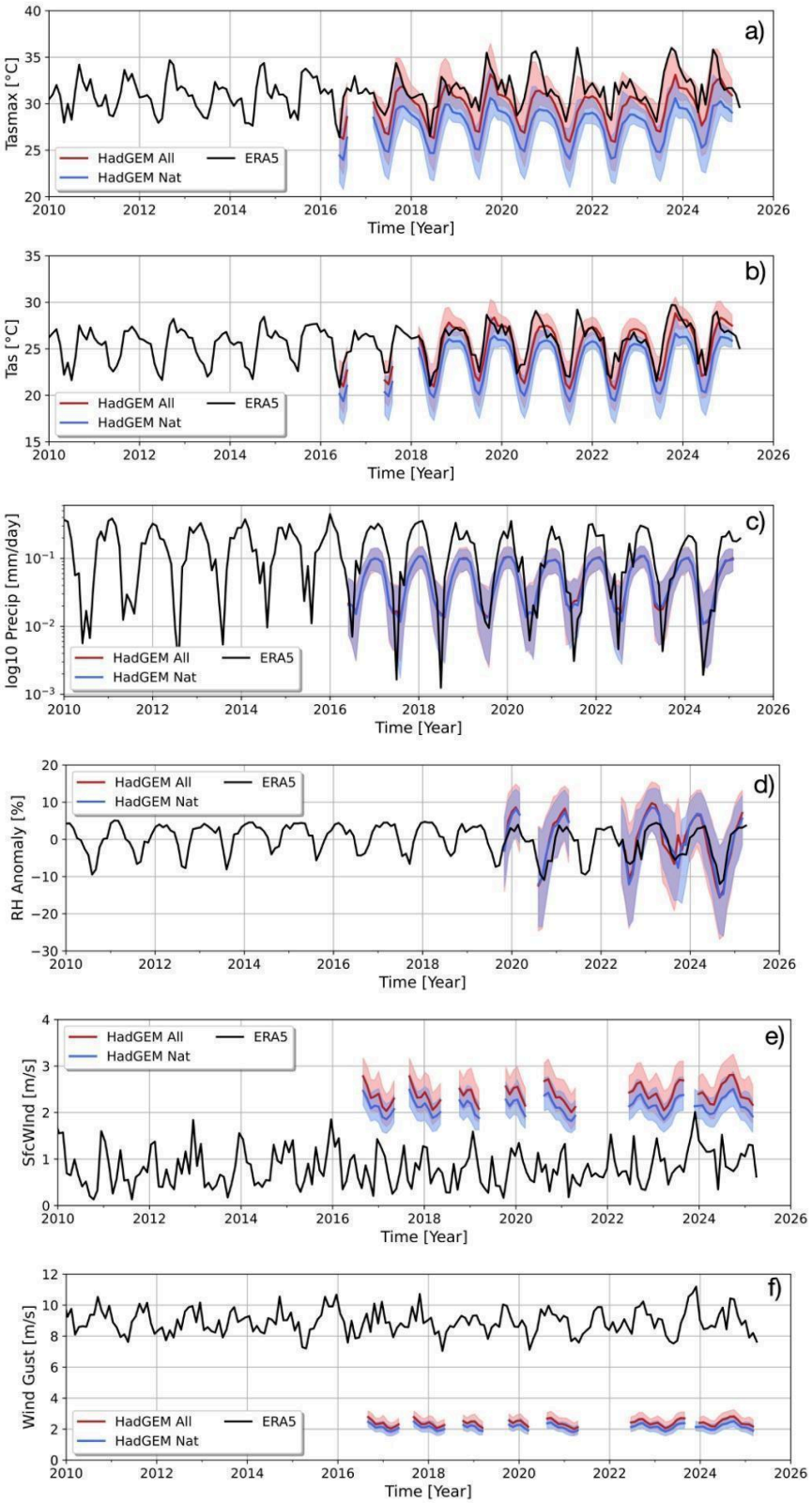

Figure S53: Same as in figure S52, but for the Pantanal-Chiquitano.

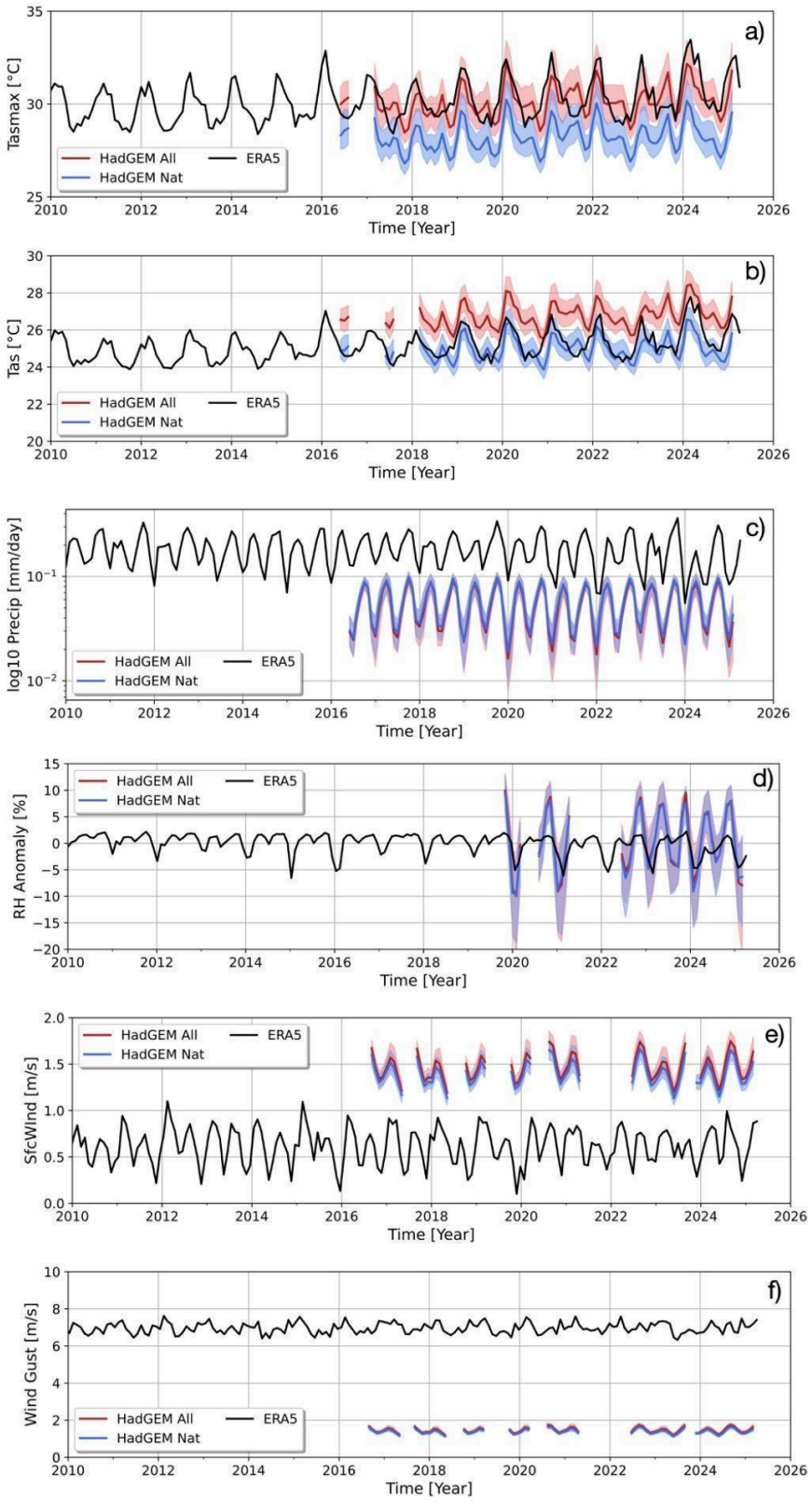

Figure S54: Same as in figure S52, but for the Congo Basin.

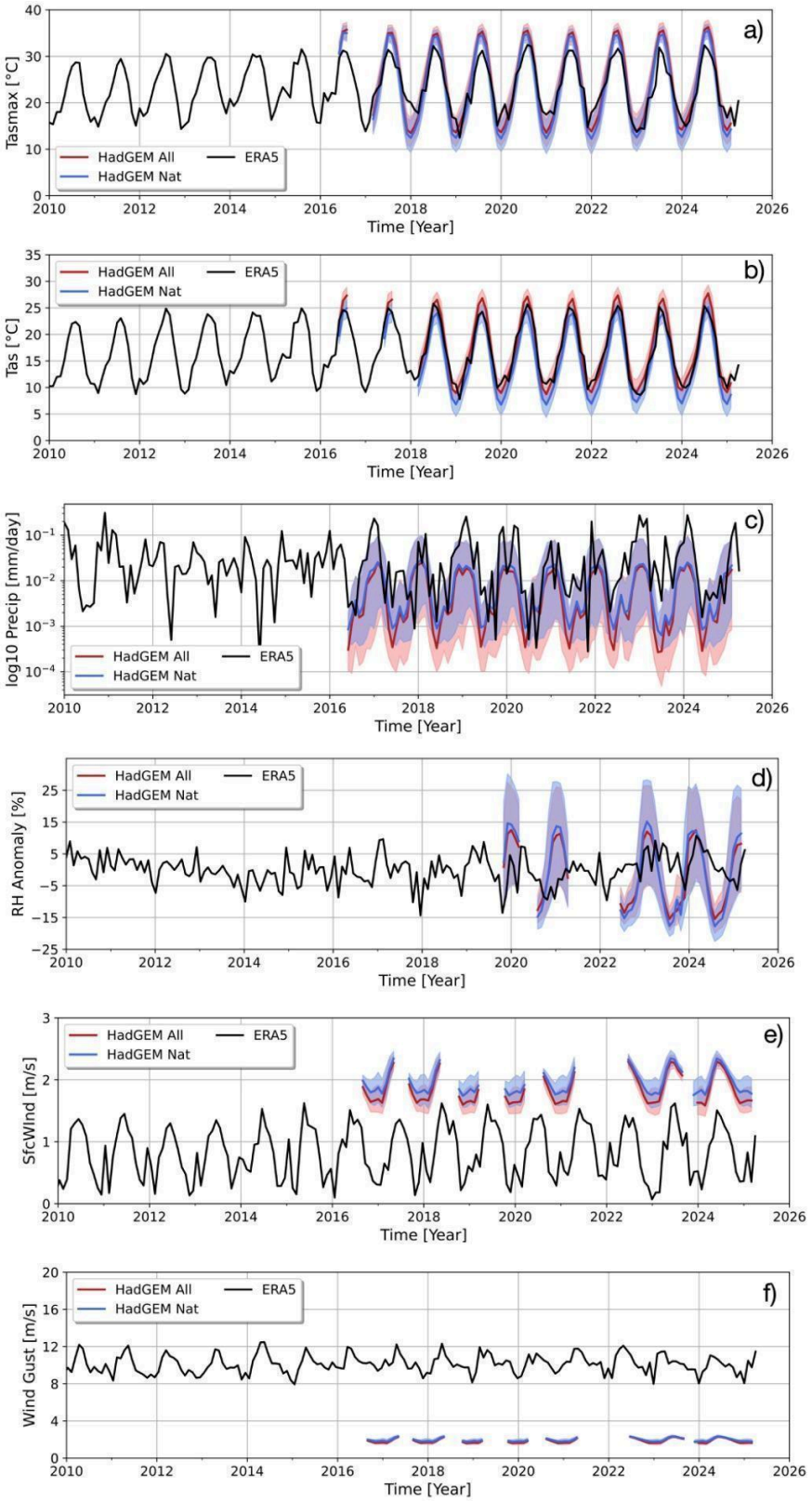

Figure S55: Same as in figure S52, but for the Souther California region.

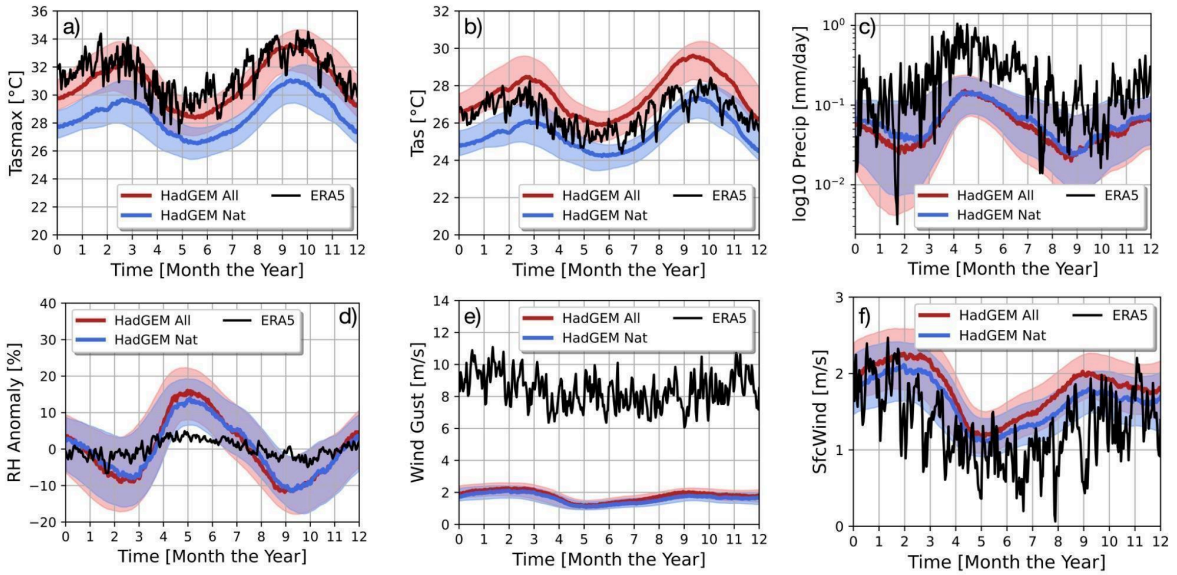

Figure S56: Seasonal cycle of individual component variables of the FWI from HadGEM (red: all forcing scenario, blue: natural forcing scenario) compared to ERA5 reanalysis (black) across 2024 over the northeast Amazonia region. We show daily a) maximum temperature, b) mean temperature, c) total precipitation, d) relative humidity, e) wind gusts as well as f) mean wind speed. Shading represents the 5th-95th percentile confidence interval.

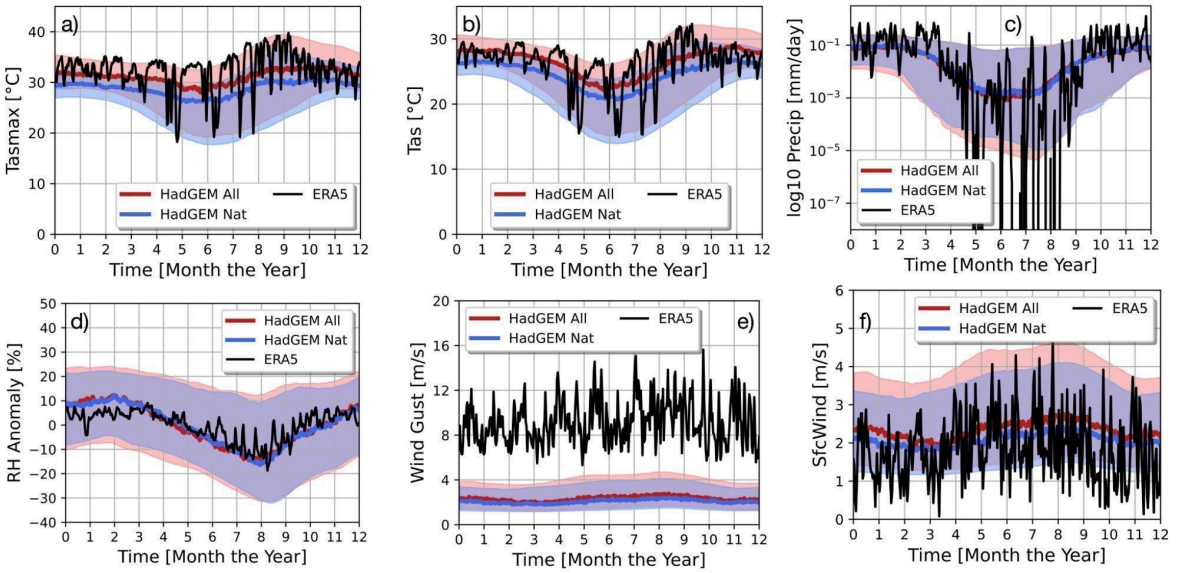

Figure S57: Same as in figure S56, but for the Pantanal-Chiquitano.

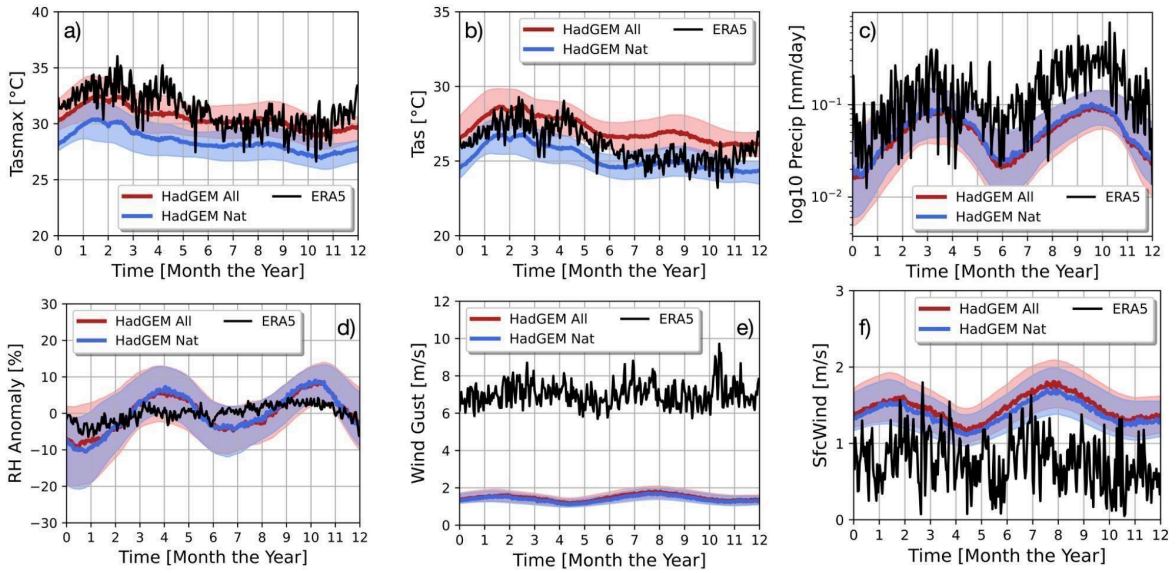

Figure S58: Same as in figure S52, but for the Congo Basin.

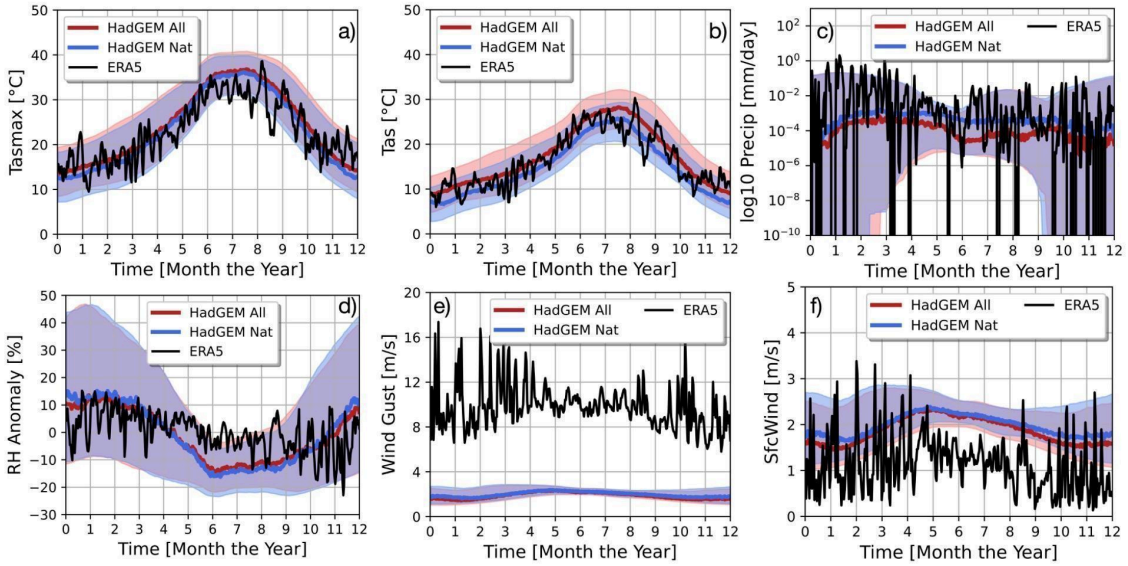

Figure S59: Same as in figure S56, but for the Southern California egion.

S9.2.2 ConFLAME evaluation - Near Real Time

Here, we apply the same evaluation method and protocol described in **Supplementary Section 4.3**, but using the Near Real-Time (NRT) configuration outlined in **Section 9.1**

S9.2.2.1 Northeast Amazonia

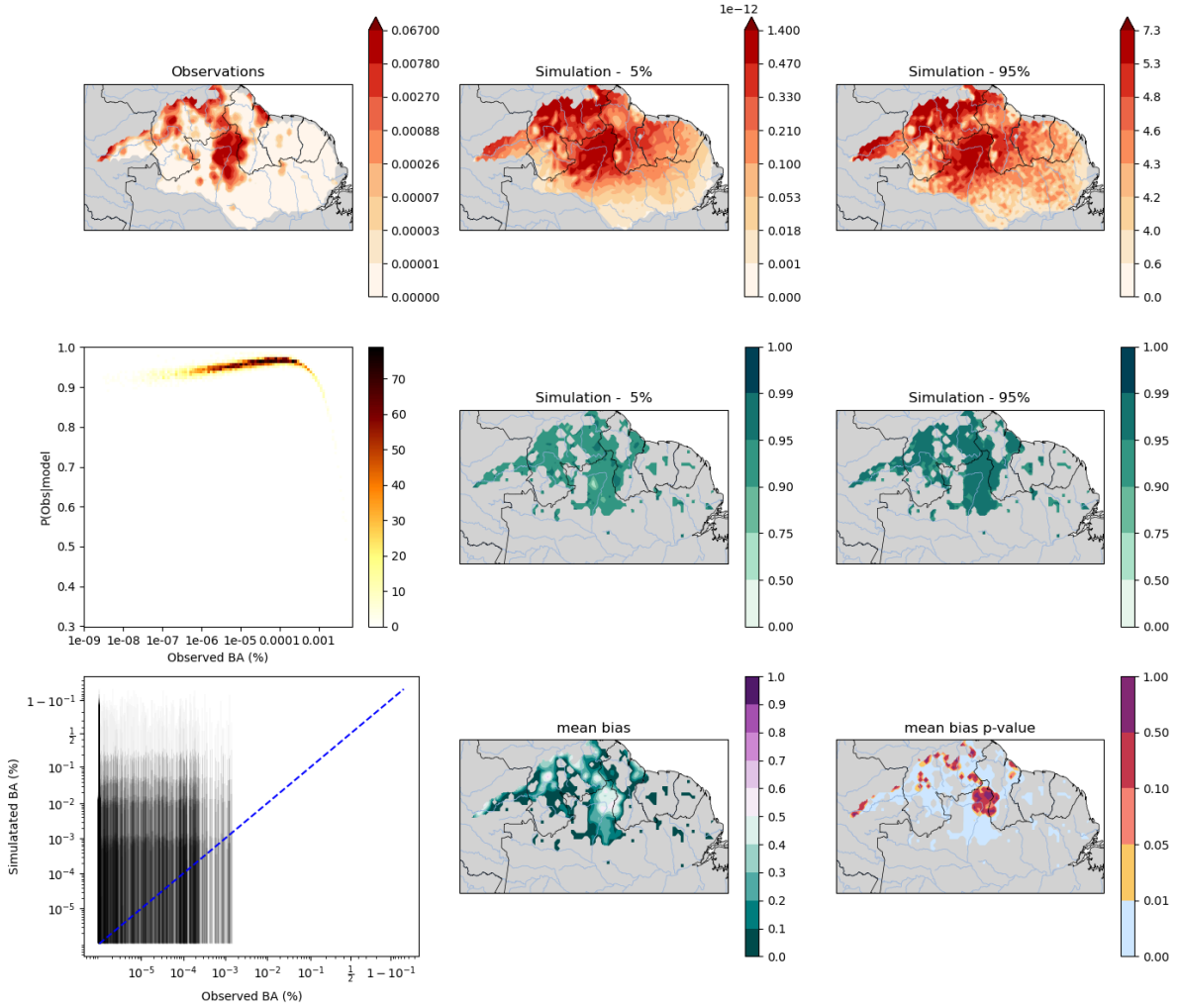

Figure S60: Although fuel moisture data were not included in this setup, the model produces a posterior distribution largely consistent with the driver-based configuration described in **Supplementary Section 9.1.1.** Some differences are evident, particularly a tendency to simulate slightly higher burned area in forested regions where this is not observed. Importantly, for attribution of extreme events in policy-relevant areas under climate change, the model captures high-end burned area values more accurately in this configuration. The top 10 % of observed burned areas correspond to approximately the 48th percentile of the posterior, and the top 5 % to around the 54th percentile, indicating a largely unbiased model performance for simulating extremes.

S9.2.2.2 Pantanal and Chiquitano

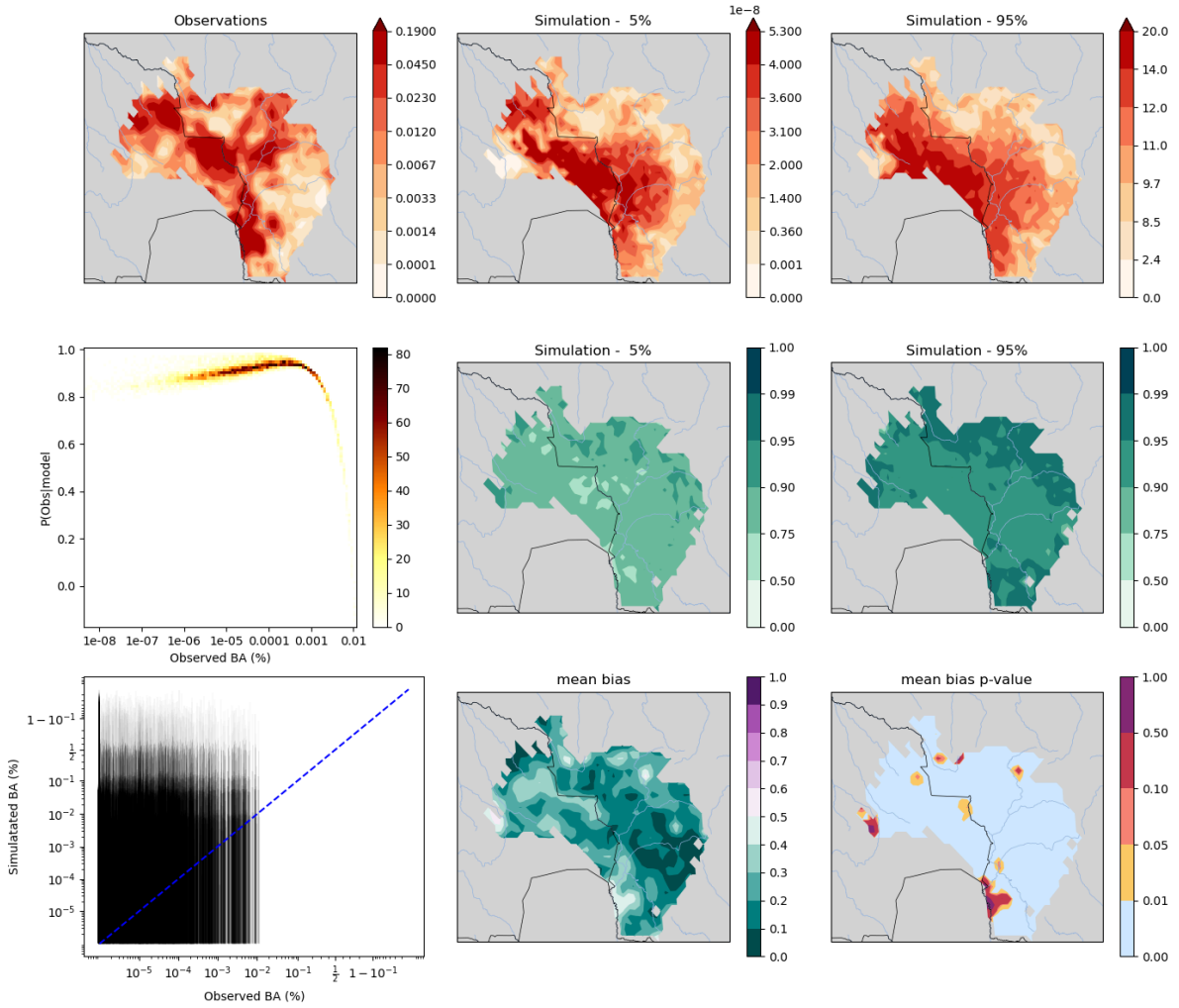

Figure S61: As with Northeastern Amazonia, the Pantanal–Chiquitano region shows very similar behaviour to the driver-based model configuration described in **Supplementary Section 9.1.2**. Again, the Near Real-Time setup performs slightly better at capturing extremes: the top 10 % of observed burned area corresponds to approximately the 60th percentile of the posterior, and the top 5 % to around the 65th percentile. This indicates a small remaining underestimation of the most extreme events, but overall good model performance.

S9.2.2.3 Southern California

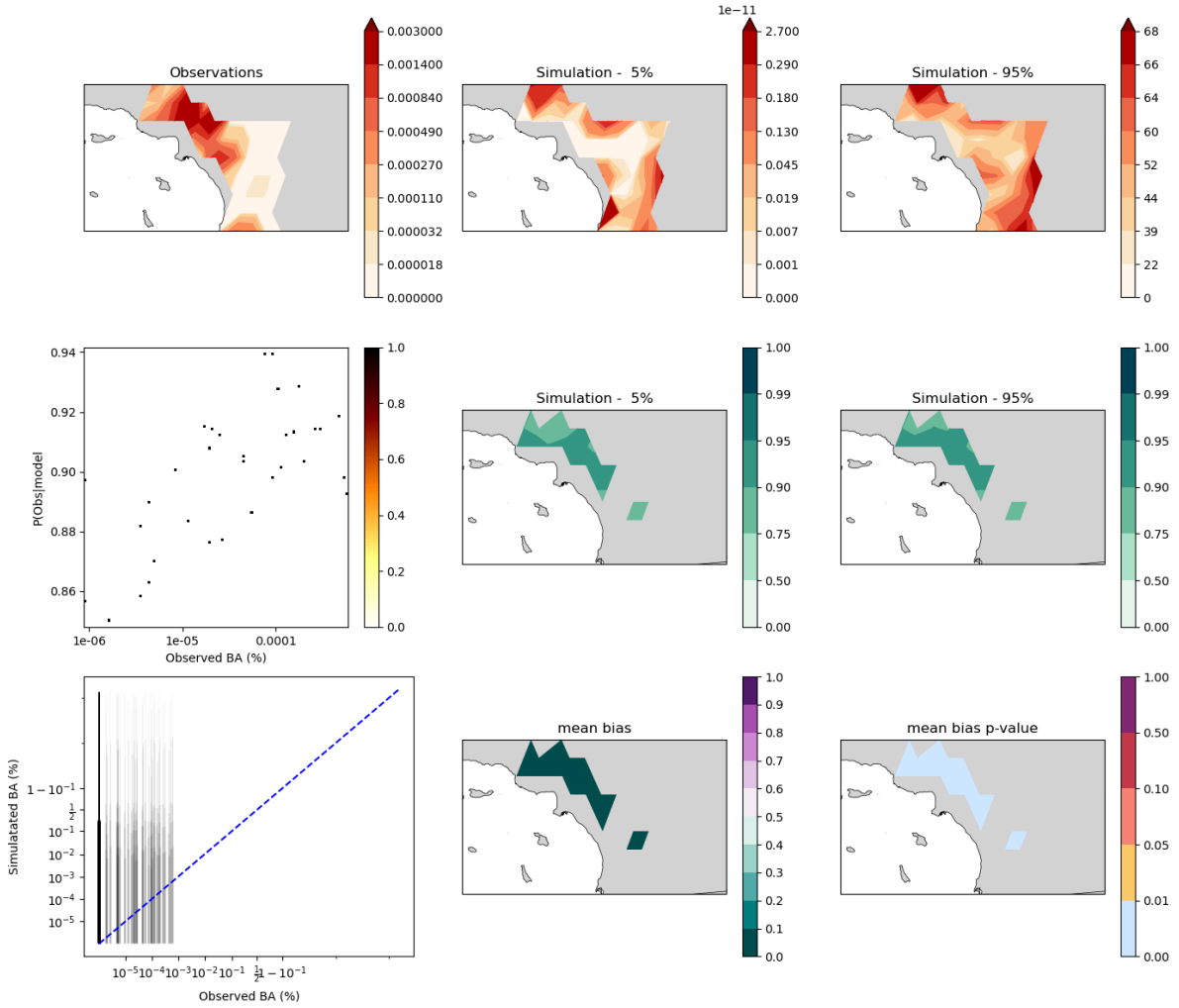

Figure S62: The spatial pattern of burned area in Southern California is slightly offset from observations but still broadly consistent, with high BA captured in both the northern and southern parts of the region. Otherwise, the Near Real-Time setup behaves similarly to the driver-based configuration described in **Supplementary Section 9.1.3.** Observed burned areas fall around the 58th percentile of the posterior distribution, indicating a model that is largely free from systematic bias.

S9.2.2.4 Congo Basin

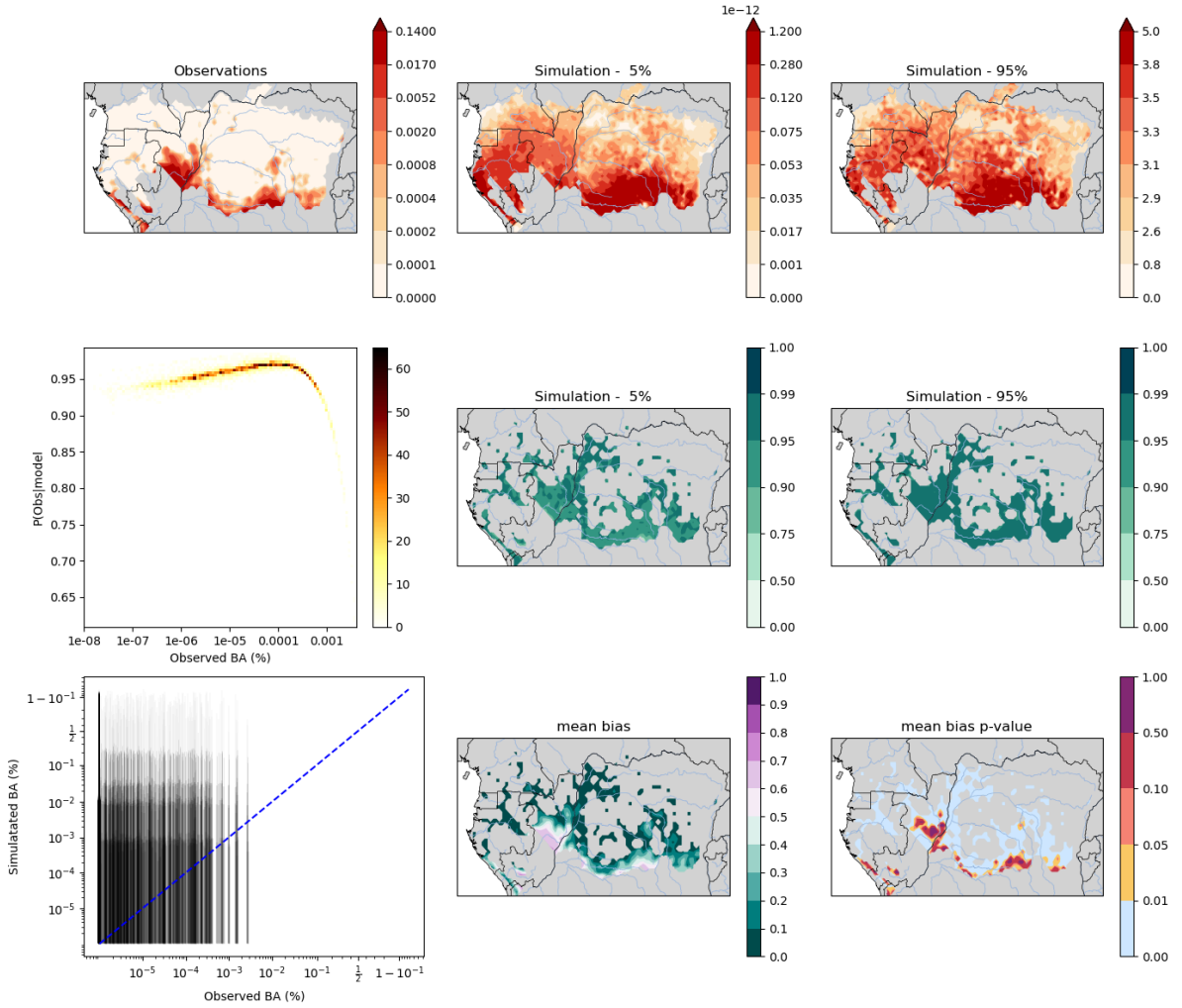

Figure S63: The Congo Basin results are again similar to the driver-based setup described in **Supplementary Section 9.1.4**, though with additional pockets of possible burning appearing throughout the central basin. As with other regions, the Near Real-Time configuration captures extremes more effectively, with the top 10% of observed burned area occurring at the 58th percentile and the top 5% at the 66th percentile of the posterior distribution.

S5.3 ConFLAME evaluation - ISIMP

Here, we apply the same evaluation method described in **Supplementary Section 9.1**, but using the Near Real-Time (ISIMIP) configuration outlined in **Section 5.1.3**. The evaluation protocol is slightly modified to account for the extended data availability period. Specifically, the model is trained on data from 2002–2009 and evaluated on 2012–2019, providing an out-of-sample assessment of model performance following the approach of Barbosa et al. (2025).

S5.3.1 Northeast Amazonia

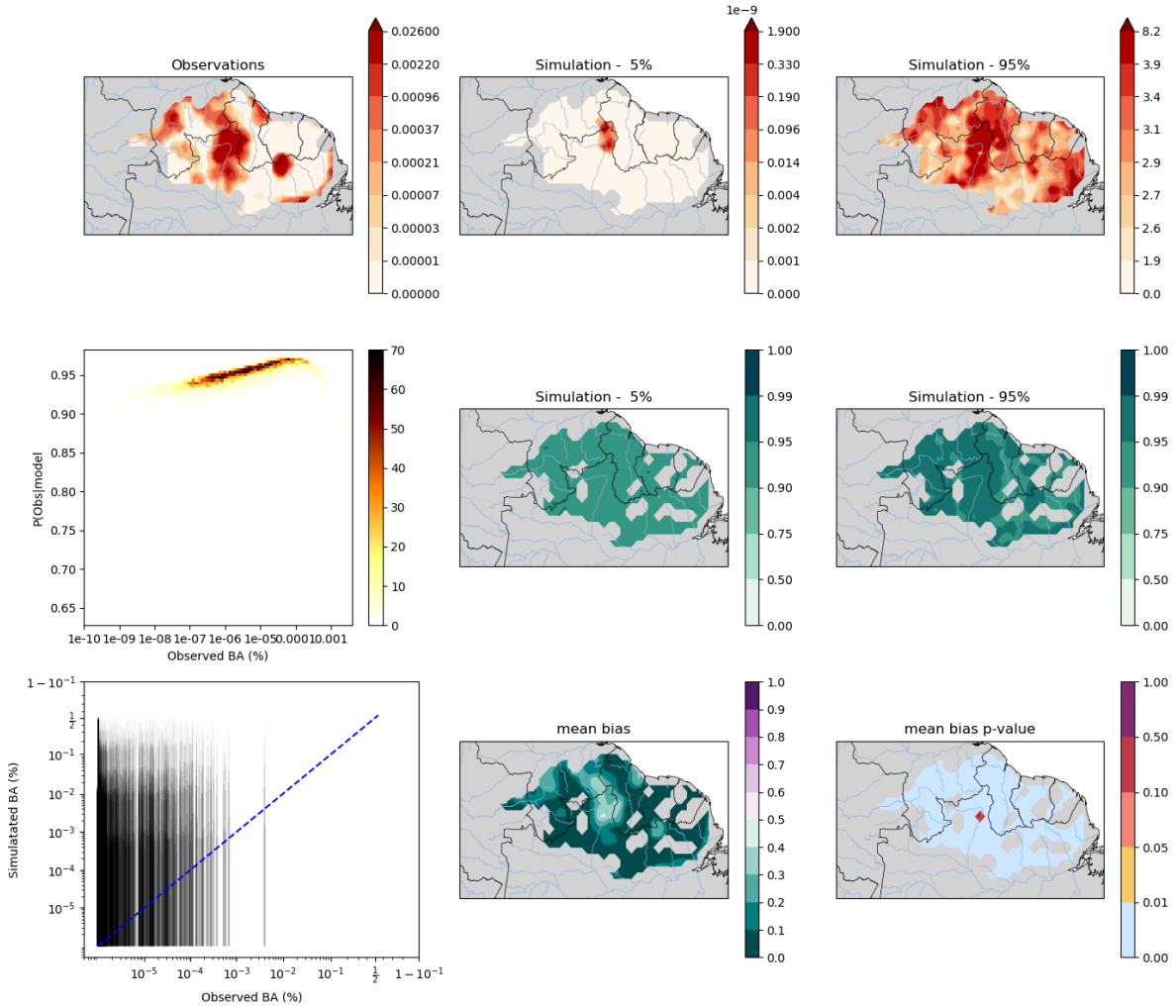

Figure S64: The spatial pattern simulated by the model closely follows that of the observed burned area in Northeastern Amazonia, though it suggests that burning could extend further into forested regions where observations may underestimate fire activity. The posterior distribution is notably wider than in the Near Real-Time configuration, which may help explain why attribution to total climate forcing (using the ISIMIP setup) is associated with greater uncertainty. However, the absence of systematic bias at the extremes, with the top 10% of observed burned area corresponding to the 53rd percentile and the top 5% to the 57th percentile of the posterior, which indicates that any detected signal would still be robust and statistically credible.

S5.3.2 Pantanal and Chiquitano

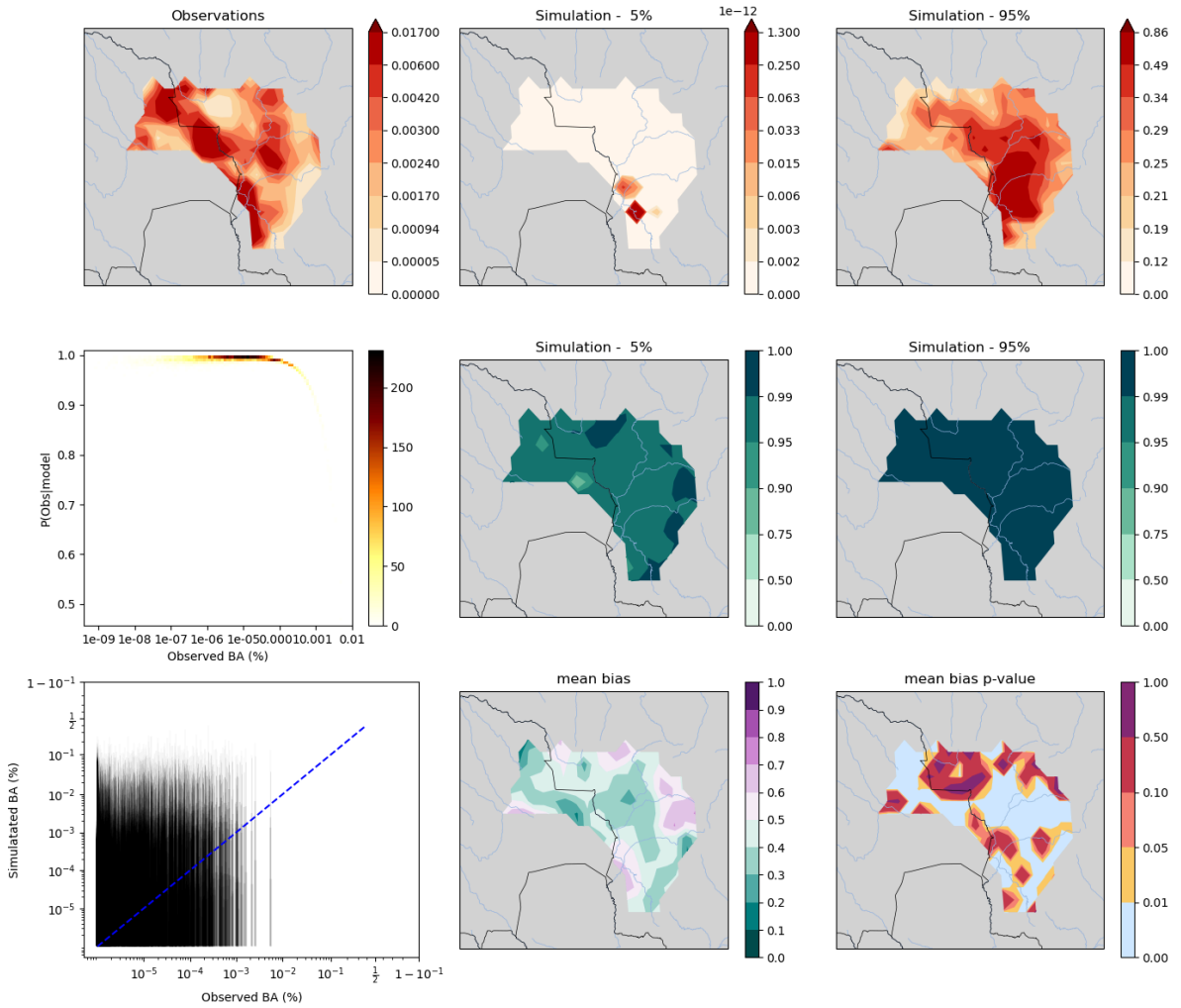

Figure S65: The model successfully captures the spatial distribution of burned area observed in the wetlands of the Pantanal and the adjacent areas to the east. However, it performs less well in representing the dry forests of Chiquitano, particularly in Bolivia. Despite this, observed burned area still falls within the simulated posterior range. The probability of the observations given the model, P(Obs | Mod), remains consistently high—around 0.95 or higher. Across the region, the model is largely unbiased, largely due to the wide uncertainty range. Extreme values are also relatively unbiased, though slightly underestimated compared to observations (with observed values averaging the 77th percentile for the top 10% of burned area and the 79th percentile for the top 5%). Overall, this supports a high degree of confidence in any formal attribution derived from this model.

S5.3.3 Southern California

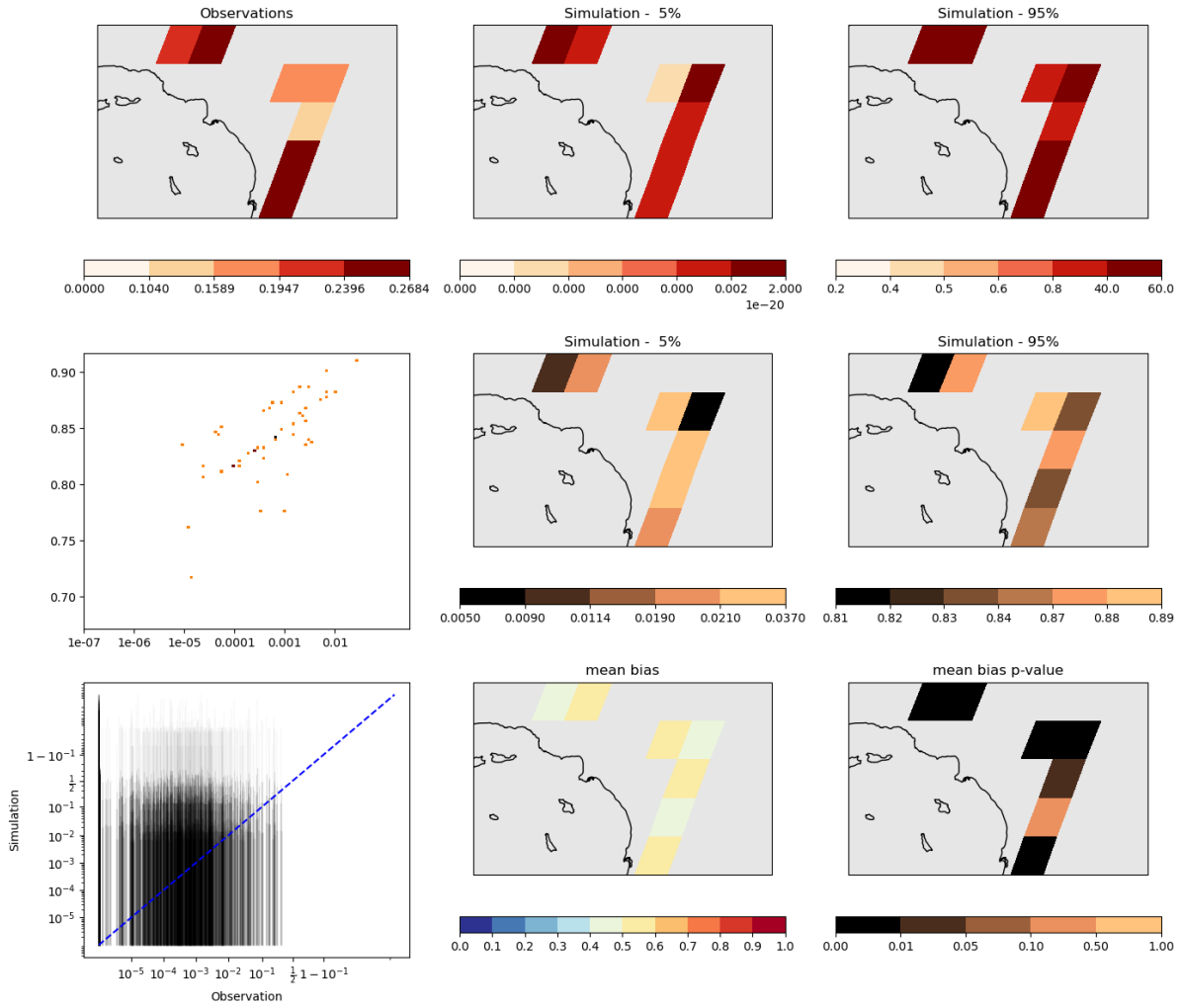

Figure S66: The coarser resolution of the ISIMIP setup means that there are too few grid cells to make meaningful spatial comparisons. Nonetheless, observations generally fall within the modelled range. The probability of the observations given the model, P(Obs | Mod), is not always high but reaches approximately 0.9 for higher burned area values. The model is also largely unbiased, with the mean position of all observed burned areas at the 67th percentile within the posterior distribution.

S5.3.4 Congo Basin

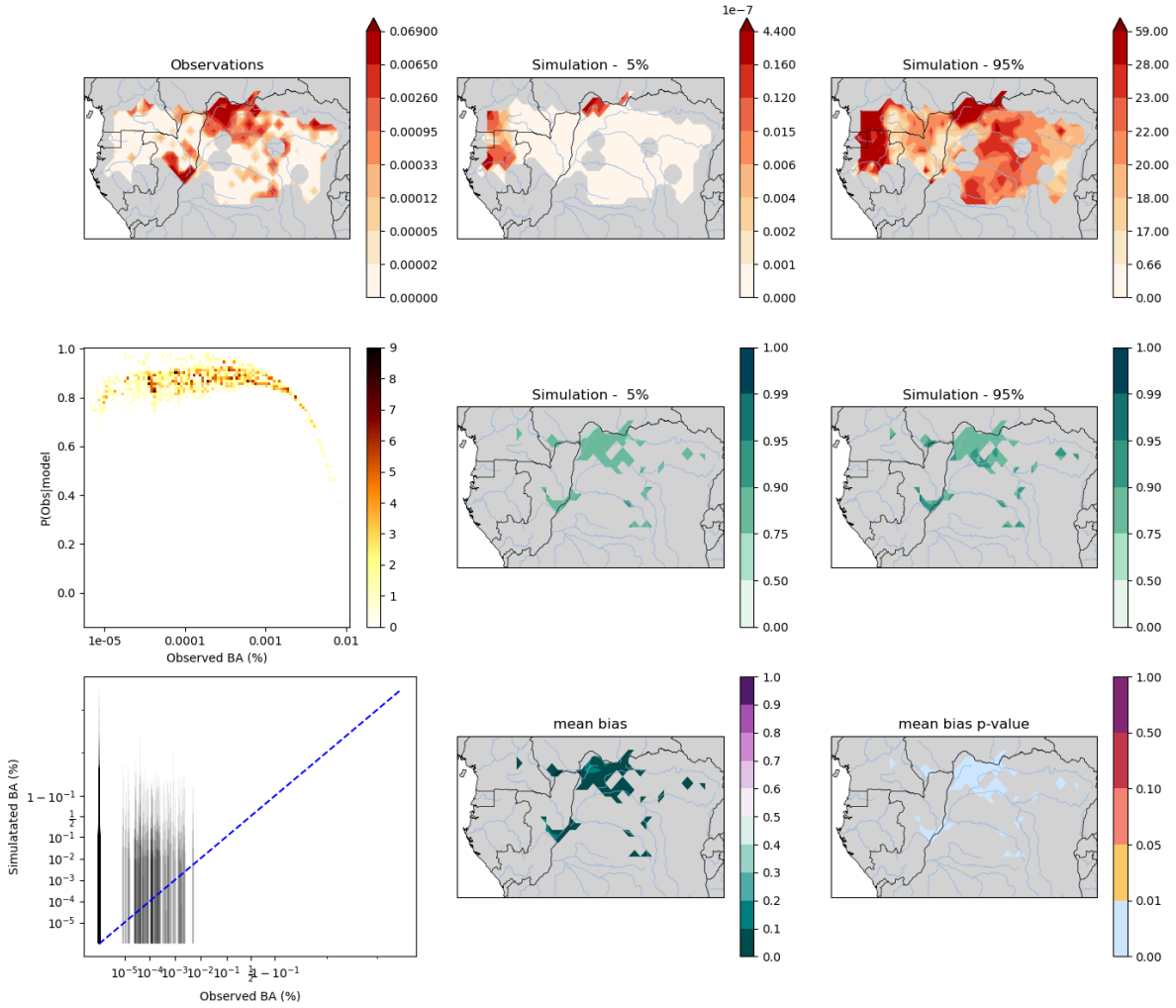

Figure S67: Over the longer period, observations also show some burning in the northern part of the basin, which is captured by the simulation. The model suggests the possibility of more extensive burning in the eastern basin than observed. Nonetheless, the model is relatively unbiased at the extremes, with the top 10% and 5% of burned area falling near the 50th percentile of the posterior distribution.

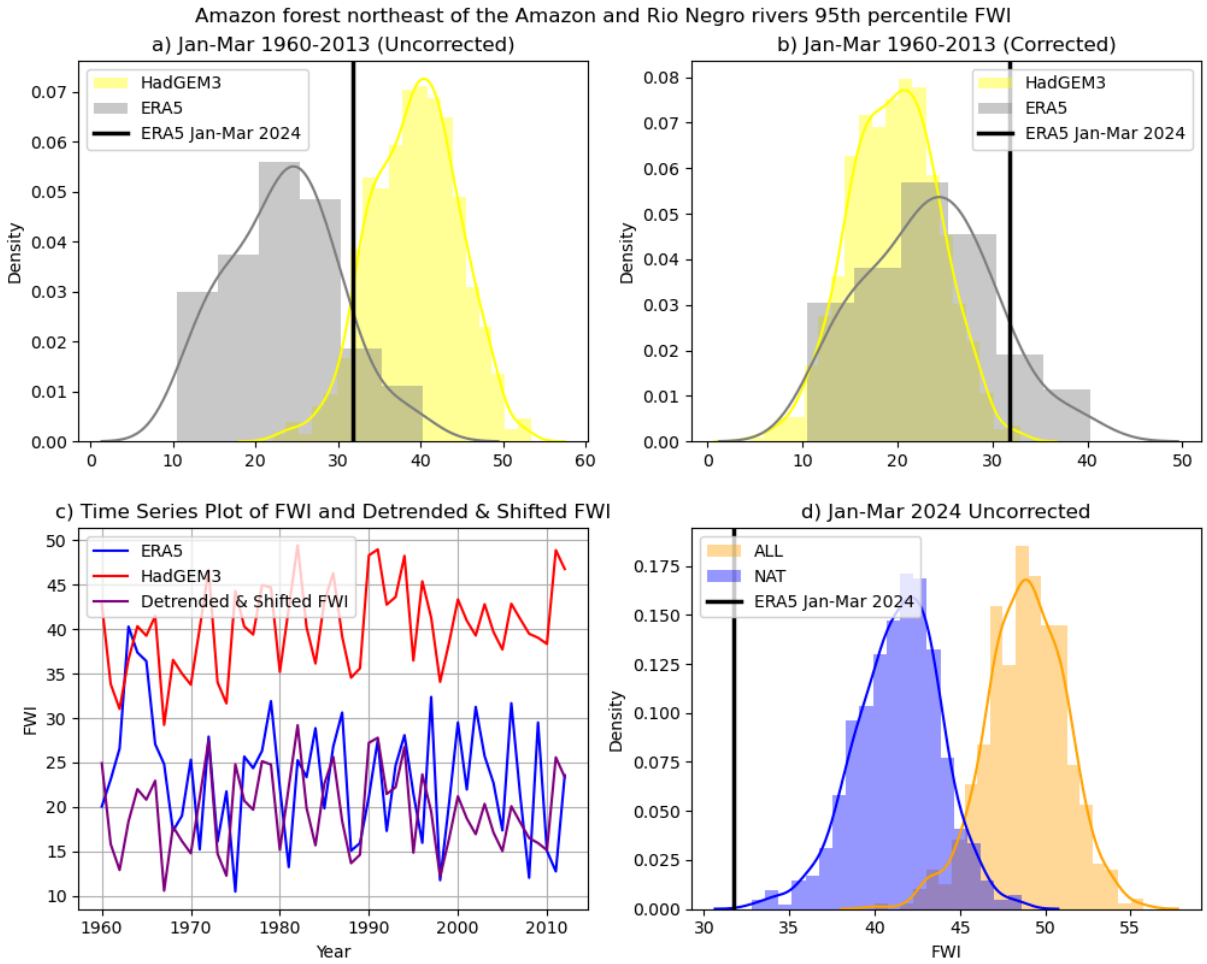

Figure S68: Bias correction for Amazon forest northeast of the Amazon and Rio Negro rivers. Historical ensemble of HadGEM3 (yellow) compared to ERA5 (grey) 95th percentile of FWI for the historical period (1960-2013), shown as probability density before correction (a) and after correction (b), and one member shown as a time series (c, where HadGEM3 is shown in red, ERA5 in blue and corrected HadGEM3 in purple). HadGEM3 ensemble for 2024 shown before bias-correction (d). ERA5 2024 event shown as black vertical line on all probability density plots.

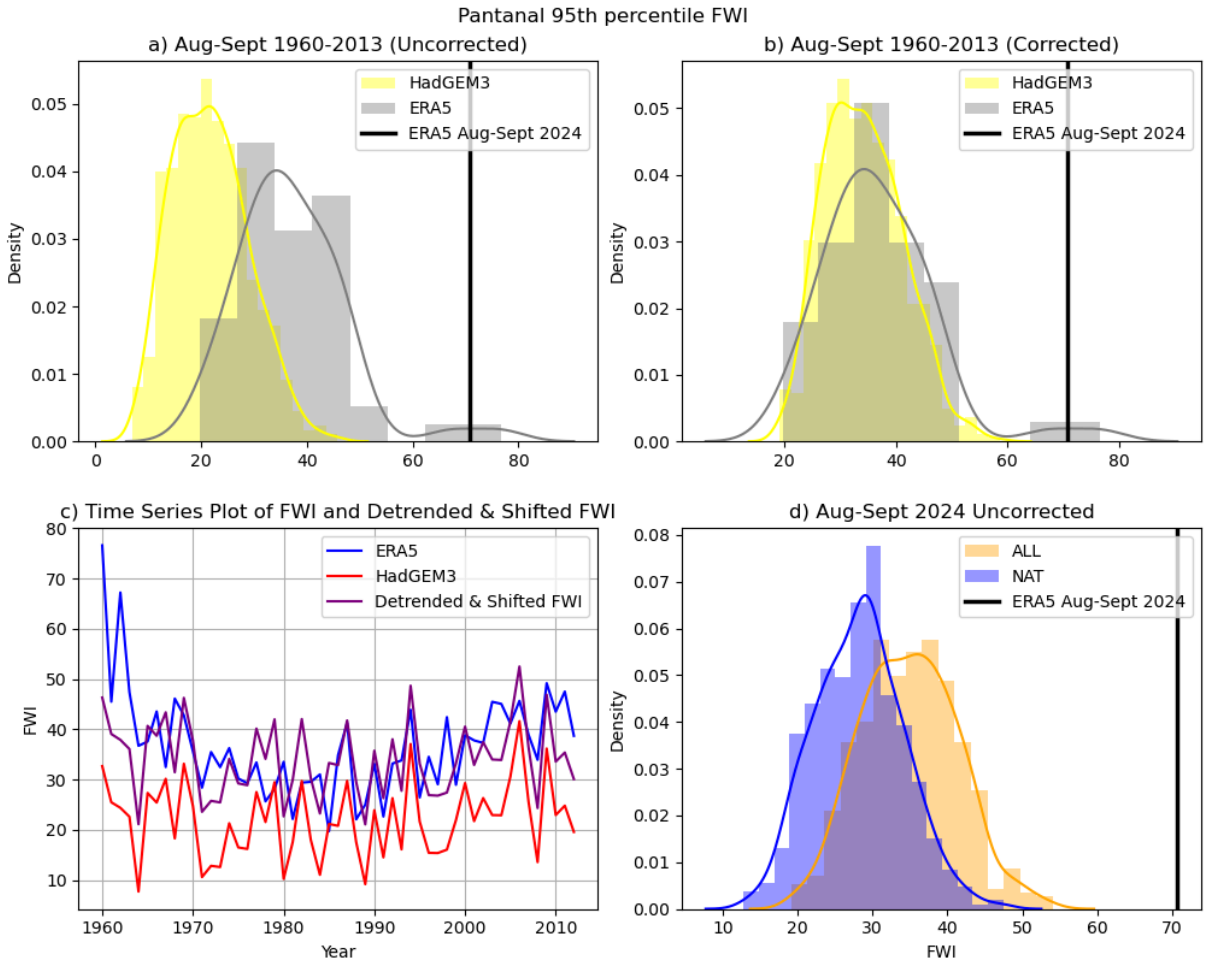

Figure S69: As for **Figure S68**, but for Pantanal & Chiquitano

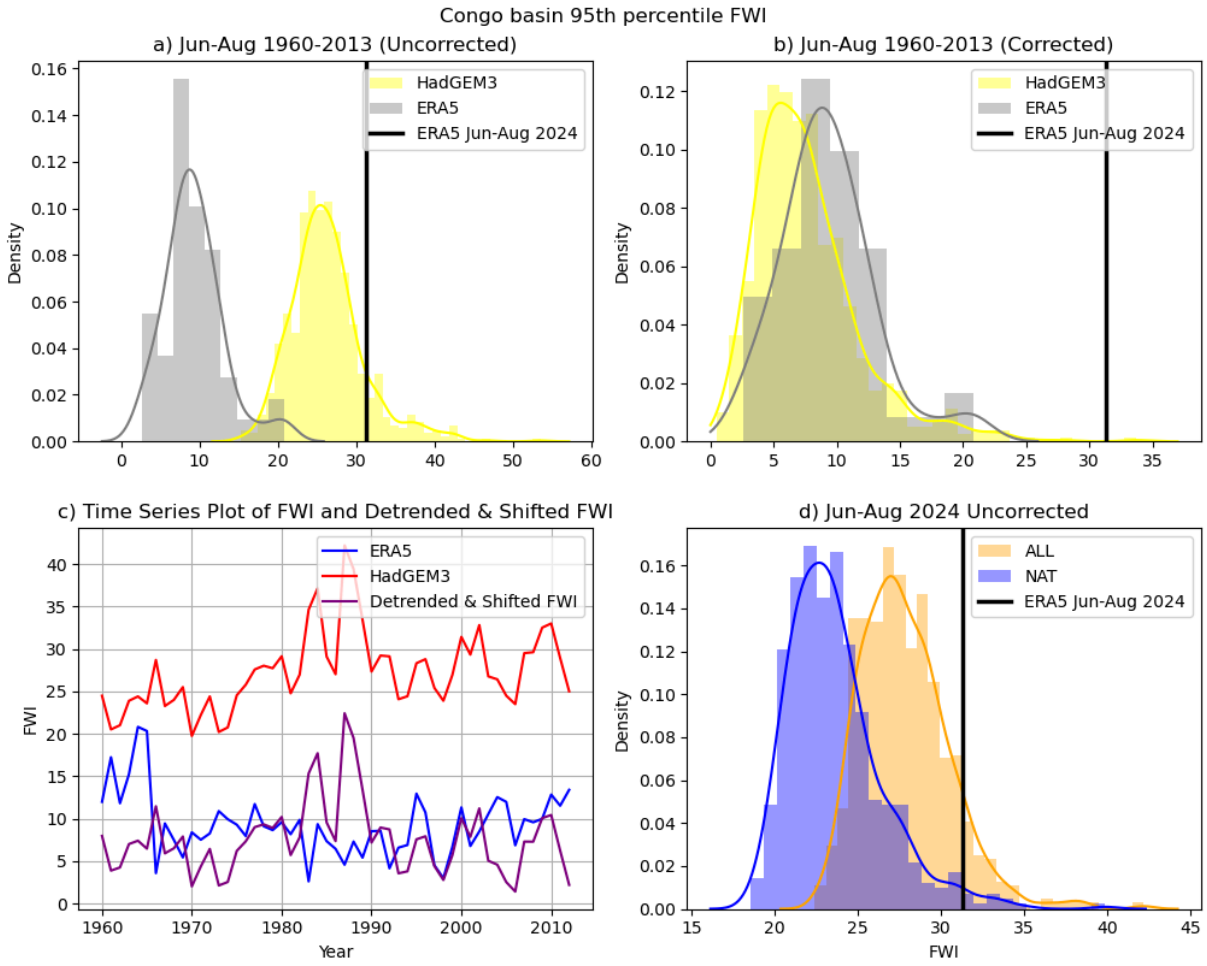

Figure S70: As for **Figure S68**, but for Congo basin

Supplementary References

Abatzoglou, J. T., Williams, A. P., Boschetti, L., Zubkova, M., and Kolden, C. A.: Global patterns of interannual climate--fire relationships, Glob. Chang. Biol., 24, 5164–5175, 2018.

Abatzoglou, J. T., Williams, A. P., and Barbero, R.: Global emergence of anthropogenic climate change in fire weather indices, Geophys. Res. Lett., 46, 326–336, https://doi.org/10.1029/2018gl080959, 2019.

Andela, N., Morton, D. C., Giglio, L., Chen, Y., van der Werf, G. R., Kasibhatla, P. S., DeFries, R. S., Collatz, G. J., Hantson, S., Kloster, S., Bachelet, D., Forrest, M., Lasslop, G., Li, F., Mangeon, S., Melton, J. R., Yue, C., and Randerson, J. T.: A human-driven decline in global burned area, Science, 356, 1356–1362, https://doi.org/10.1126/science.aal4108, 2017.

Barbero, R., Abatzoglou, J. T., Steel, E. A., and K Larkin, N.: Modeling very large-fire occurrences over the continental United States from weather and climate forcing, Environ. Res. Lett., 9, 124009, https://doi.org/10.1088/1748-9326/9/12/124009, 2014.

Barbosa, M. L. F., Kelley, D. I., Burton, C. A., Ferreira, I. J. M., da Veiga, R. M., Bradley, A.,

Molin, P. G., and Anderson, L. O.: FLAME 1.0: a novel approach for modelling burned area in the Brazilian biomes using the maximum entropy concept, Geosci. Model Dev., 18, 3533–3557, https://doi.org/10.5194/gmd-18-3533-2025, 2025.

Boussetta, S., Balsamo, G., Arduini, G., Dutra, E., McNorton, J., Choulga, M., Agustí-Panareda, A., Beljaars, A., Wedi, N., Munõz-Sabater, J., de Rosnay, P., Sandu, I., Hadade, I., Carver, G., Mazzetti, C., Prudhomme, C., Yamazaki, D., and Zsoter, E.: ECLand: The ECMWF land surface modelling system, Atmosphere (Basel), 12, 723, https://doi.org/10.3390/atmos12060723, 2021.

Burton, C., Betts, R., Cardoso, M., Feldpausch, T. R., Harper, A., Jones, C. D., Kelley, D. I., Robertson, E., and Wiltshire, A.: Representation of fire, land-use change and vegetation dynamics in the Joint UK Land Environment Simulator vn4. 9 (JULES), Geoscientific Model Development, 12, 179–193, 2019.

Burton, C., Betts, R. A., Jones, C. D., Feldpausch, T. R., Cardoso, M., and Anderson, L. O.: El Niño Driven Changes in Global Fire 2015/16, Front Earth Sci. Chin., 8, https://doi.org/10.3389/feart.2020.00199, 2020.

Burton, C., Kelley, D. I., Jones, C. D., Betts, R. A., Cardoso, M., and Anderson, L.: South American fires and their impacts on ecosystems increase with continued emissions, Climate Resilience and Sustainability, 1, e8, https://doi.org/10.1002/cli2.8, 2022.

Burton, C. A., Lampe, S., Kelley, D., Thiery, W., Hantson, S., Christidis, N., Gudmundsson, L., Forrest, M., Burke, E., Chang, J., Huang, H., Ito, A., Kou‐Giesbrecht, S., Lasslop, G., Li, W., Nieradzik, L., Li, F., Chen, Y., Randerson, J., Reyer, C. P. O., and Mengel, M.: Global burned area increasingly explained by climate change, Nat. Clim. Chang., 1–7, https://doi.org/10.1038/s41558-024-02140-w, 2024.

Burton, C. A., Ciavarella, A., Kelley, D., Hartley, A. J., McCarthy, M., S. New, Betts, R. A., and Robertson, E.: Very high fire danger in UK in 2022 at least 6 times more likely due to human-caused climate change, Environ. Res. Lett., 20, https://doi.org/10.1088/1748-9326/adb764, 2025.

Center for International Earth Science Information Network (CIESIN): Gridded Population of the World, Version 4 (GPWv4): Population Count, Revision 11, 2025.

Chuvieco, E., Lucrecia Pettinari, M., Lizundia-Loiola, J., Khairoun, A., Danne, O., Boettcher, M., and Storm, T.: ESA Fire Climate Change Initiative (Fire_cci): Sentinel-3 SYN Burned Area Grid product, version 1.1, 2024.

Clark, D. B., Mercado, L. M., Sitch, S., Jones, C. D., Gedney, N., Best, M. J., Pryor, M., Rooney, G. G., Essery, R. L. H., Blyth, E., Boucher, O., Harding, R. J., Huntingford, C., and Cox, P. M.: The Joint UK Land Environment Simulator (JULES), model description – Part 2: Carbon fluxes and vegetation dynamics, Geoscientific Model Development, 4, 701–722, https://doi.org/10.5194/gmd-4-701-2011, 2011.

CMES: Fire danger indices historical data from the Copernicus Emergency Management Service, https://doi.org/10.24381/CDS.0E89C522, 2019.

Cunningham, D., Cunningham, P., and Fagan, M. E.: Evaluating forest cover and fragmentation in Costa Rica with a corrected global tree cover map, Remote Sens. (Basel), 12, 3226, https://doi.org/10.3390/rs12193226, 2020.

Di Giuseppe, F., Pappenberger, F., Wetterhall, F., Krzeminski, B., Camia, A., Libertá, G., and San Miguel, J.: The potential predictability of fire danger provided by numerical weather

prediction, J. Appl. Meteorol. Climatol., 55, 2469–2491, https://doi.org/10.1175/jamc-d-15-0297.1, 2016.

Dimiceli, C., Carroll, M., Sohlberg, R., Kim, D.-H., and Kelly, M.: MOD44B MODIS/Terra Vegetation Continuous Fields Yearly L3 Global 250m SIN Grid V006, https://doi.org/10.5067/MODIS/MOD44B.006, 2015.

Eden, J. M., Wolter, K., Otto, F. E. L., and Jan van Oldenborgh, G.: Multi-method attribution analysis of extreme precipitation in Boulder, Colorado, Environ. Res. Lett., 11, 124009, https://doi.org/10.1088/1748-9326/11/12/124009, 2016.

Eden, J. M., Kew, S. F., Bellprat, O., Lenderink, G., Manola, I., Omrani, H., and J., van O. G.: Extreme precipitation in the Netherlands: An event attribution case study, Weather and climate extremes, 21, 90–101, 2018.

Efron, B. and Tibshirani, R.: The problem of regions, Ann. Stat., 26, 1687–1718, https://doi.org/10.1214/aos/1024691353, 1998.

Eyring, V., Bony, S., Meehl, G. A., Senior, C. A., Stevens, B., Stouffer, R. J., and Taylor, K. E.: Overview of the Coupled Model Intercomparison Project Phase 6 (CMIP6) experimental design and organization, Geosci. Model Dev., 9, 1937–1958, https://doi.org/10.5194/gmd-9-1937-2016, 2016.

Giglio, L.: VIIRS/NPP Burned Area Monthly L4 Global 500m SIN Grid V002, https://doi.org/10.5067/VIIRS/VNP64A1.002, 2024.

Giglio, L., Boschetti, L., Roy, D. P., Humber, M. L., and Justice, C. O.: The Collection 6 MODIS burned area mapping algorithm and product, Remote Sens. Environ., 217, 72–85, https://doi.org/10.1016/j.rse.2018.08.005, 2018.

Gneiting, T. and Katzfuss, M.: Probabilistic forecasting, Annu. Rev. Stat. Appl., 1, 125–151, https://doi.org/10.1146/annurev-statistics-062713-085831, 2014.

Goss, M., Swain, D. L., Abatzoglou, J. T., Sarhadi, A., Kolden, C. A., Williams, A. P., and Diffenbaugh, N. S.: Climate change is increasing the likelihood of extreme autumn wildfire conditions across California, Environ. Res. Lett., 15, 094016, https://doi.org/10.1088/1748-9326/ab83a7, 2020.

Guzman-Morales, J. and Gershunov, A.: Climate change suppresses Santa Ana winds of southern California and sharpens their seasonality, Geophys. Res. Lett., 46, 2772–2780, https://doi.org/10.1029/2018gl080261, 2019.

Hantson, S., Arneth, A., Harrison, S. P., and Kelley, D. I.: The status and challenge of global fire modelling, 2016.

Hawkins, L. R., Abatzoglou, J. T., Li, S., and Rupp, D. E.: Anthropogenic influence on recent severe autumn fire weather in the west coast of the United States, Geophys. Res. Lett., 49, https://doi.org/10.1029/2021gl095496, 2022.

Hersbach, H., Bell, B., Berrisford, P., Biavati, G., Horányi, A., Muñoz Sabater, J., Nicolas, J., Peubey, C., Radu, R., Rozum, I., Schepers, D., Simmons, A., Soci, C., Dee, D., and Thépaut, J.-N.: ERA5 hourly data on single levels from 1940 to present, https://doi.org/10.24381/cds.adbb2d47, 2023.

Huang, H., Xue, Y., Li, F., and Liu, Y.: Modeling long-term fire impact on ecosystem characteristics and surface energy using a process-based vegetation–fire model

SSiB4/TRIFFID-Fire v1.0, Geosci. Model Dev., https://doi.org/10.5194/gmd-2020-122-supplement, 2020.

Huang, H., Xue, Y., Liu, Y., Li, F., and Okin, G.: Modeling the short-term fire effects on vegetation dynamics and surface energy in Southern Africa using the improved SSiB4/TRIFFID-Fire model, https://doi.org/10.5194/gmd-2021-116, 2021.

Hugelius, G., Tarnocai, C., Broll, G., Canadell, J. G., Kuhry, P., and Swanson, D. K.: The Northern Circumpolar Soil Carbon Database: spatially distributed datasets of soil coverage and soil carbon storage in the northern permafrost regions, Earth Syst. Sci. Data, 5, 3–13, https://doi.org/10.5194/essd-5-3-2013, 2013.

Ito, A.: Disequilibrium of terrestrial ecosystem CO2 budget caused by disturbance-induced emissions and non-CO2 carbon export flows: a global model assessment, Earth Syst. Dyn., 10, 685–709, https://doi.org/10.5194/esd-10-685-2019, 2019.

Jolly, W. M., Cochrane, M. A., Freeborn, P. H., Holden, Z. A., Brown, T. J., Williamson, G. J., and Bowman, D. M. J. S.: Climate-induced variations in global wildfire danger from 1979 to 2013, Nat. Commun., 6, 7537, https://doi.org/10.1038/ncomms8537, 2015.

Jones, M. W., Abatzoglou, J. T., Veraverbeke, S., Andela, N., Lasslop, G., Forkel, M., Smith, A. J. P., Burton, C., Betts, R. A., van der Werf, G. R., Sitch, S., Canadell, J. G., Santín, C., Kolden, C., Doerr, S. H., and Le Quéré, C.: Global and regional trends and drivers of fire under climate change, Rev. Geophys., 60, https://doi.org/10.1029/2020rg000726, 2022.

Jones, M. W., Veraverbeke, S., Andela, N., Doerr, S. H., Kolden, C., Mataveli, G., Pettinari, M. L., Le Quéré, C., Rosan, T. M., van der Werf, G. R., van Wees, D., and Abatzoglou, J. T.: Global rise in forest fire emissions linked to climate change in the extratropics, Science, 386, eadl5889, https://doi.org/10.1126/science.adl5889, 2024a.

Jones, M. W., Kelley, D. I., Burton, C. A., Di Giuseppe, F., Barbosa, M. L. F., Brambleby, E., Hartley, A. J., Lombardi, A., Mataveli, G., McNorton, J. R., Spuler, F. R., Wessel, J. B., Abatzoglou, J. T., Anderson, L. O., Andela, N., Archibald, S., Armenteras, D., Burke, E., Carmenta, R., Chuvieco, E., Clarke, H., Doerr, S. H., Fernandes, P. M., Giglio, L., Hamilton, D. S., Hantson, S., Harris, S., Jain, P., Kolden, C. A., Kurvits, T., Lampe, S., Meier, S., Stacey New, Parrington, M., Perron, M. M. G., Qu, Y., Ribeiro, N. S., Saharjo, B. H., San-Miguel-Ayanz, J., Shuman, J. K., Tanpipat, V., Van Der Werf, G. R., Veraverbeke, S., and Xanthopoulos, G.: State of Wildfires 2023–2024, Earth Syst. Sci. Data, 16, 3601–3685, https://doi.org/10.5194/essd-16-3601-2024, 2024b.

Kelley, D. I., Prentice, I. C., Harrison, S. P., Wang, H., Simard, M., Fisher, J. B., and Willis, K. O.: A comprehensive benchmarking system for evaluating global vegetation models, Biogeosciences, 10, 3313–3340, https://doi.org/10.5194/bg-10-3313-2013, 2013.

Kelley, D. I., Bistinas, I., Whitley, R., and Burton, C.: How contemporary bioclimatic and human controls change global fire regimes, Nat. Clim. Chang., 2019.

Kelley, D. I., Burton, C., Huntingford, C., Brown, M. A. J., Whitley, R., and Dong, N.: Technical note: Low meteorological influence found in 2019 Amazonia fires, Biogeosciences, 18, 787–804, https://doi.org/10.5194/bg-18-787-2021, 2021.

Klein Goldewijk, K., Goldewijk, K. K., Beusen, A., Van Drecht, G., and De Vos, M.: The HYDE 3.1 spatially explicit database of human-induced global land-use change over the past 12,000 years, Glob. Ecol. Biogeogr., 20, 73–86, https://doi.org/10.1111/j.1466-8238.2010.00587.x, 2010.

Knorr, W., Kaminski, T., Arneth, A., and Weber, U.: Impact of human population density on fire frequency at the global scale, Biogeosciences, 11, 1085–1102, 2014.

Knutti, R., Sedláček, J., Sanderson, B. M., Lorenz, R., Fischer, E. M., and Eyring, V.: A climate model projection weighting scheme accounting for performance and interdependence, Geophys. Res. Lett., 44, 1909–1918, https://doi.org/10.1002/2016gl072012, 2017.

Krikken, F., Lehner, F., Haustein, K., Drobyshev, I., and J., van O. G.: Attribution of the role of climate change in the forest fires in Sweden 2018, Natural Hazards and Earth System Sciences, 21, 2169–2179, 2021.

Lehsten, V., Tansey, K., Balzter, H., Thonicke, K., Spessa, A., Weber, U., Smith, B., and Arneth, A.: Estimating carbon emissions from African wildfires, Biogeosciences, 6, 349–360, https://doi.org/10.5194/bg-6-349-2009, 2009.

Li, F., Zeng, X. D., and Levis, S.: A process-based fire parameterization of intermediate complexity in a Dynamic Global Vegetation Model, Biogeosciences, 9, 2761–2780, https://doi.org/10.5194/bg-9-2761-2012, 2012.

Li, F., Levis, S., and Ward, D. S.: Quantifying the role of fire in the Earth system – Part 1: Improved global fire modeling in the Community Earth System Model (CESM1), Biogeosciences, 10, 2293–2314, https://doi.org/10.5194/bg-10-2293-2013, 2013.

Liu, J., Feng, X., Gu, X., Zhang, J., Slater, L. J., and Kong, D.: Detection and attribution of human influence on the global diurnal temperature range decline, Geophys. Res. Lett., 49, https://doi.org/10.1029/2021gl097155, 2022a.

Liu, W., Su, X., Zhang, G., and Chen, D.: Projection of future dry-wet evolution in Northwest China and its uncertainty attribution analysis, River, 2, 65–78, https://doi.org/10.1002/rvr2.39, 2023.

Liu, Z., Eden, J. M., Dieppois, B., and Blackett, M.: A global view of observed changes in fire weather extremes: uncertainties and attribution to climate change, Clim. Change, 173, https://doi.org/10.1007/s10584-022-03409-9, 2022b.

Liu, Z., Eden, J. M., Dieppois, B., Drobyshev, I., Gallo, C., and Blackett, M.: Were meteorological conditions related to the 2020 Siberia wildfires made more likely by anthropogenic climate change?, Bull. Am. Meteorol. Soc., 103, S44–S49, https://doi.org/10.1175/bams-d-21-0168.1, 2022c.

Li, Y., Sulla-Menashe, D., Motesharrei, S., Song, X.-P., Kalnay, E., Ying, Q., Li, S., and Ma, Z.: Inconsistent estimates of forest cover change in China between 2000 and 2013 from multiple datasets: differences in parameters, spatial resolution, and definitions, Sci. Rep., 7, 8748, https://doi.org/10.1038/s41598-017-07732-5, 2017.

Lizundia-Loiola, J., Franquesa, M., Khairoun, A., and Chuvieco, E.: Global burned area mapping from Sentinel-3 Synergy and VIIRS active fires, Remote Sens. Environ., 282, 113298, https://doi.org/10.1016/j.rse.2022.113298, 2022.

Lopez, P.: A lightning parameterization for the ECMWF Integrated Forecasting System, Mon. Weather Rev., 144, 3057–3075, https://doi.org/10.1175/mwr-d-16-0026.1, 2016.

Mangeon, S., Voulgarakis, A., Gilham, R., Harper, A., Sitch, S., and Folberth, G.: INFERNO: a fire and emissions scheme for the UK Met Office's Unified Model, Geosci. Model Dev., 9, 2685–2700, https://doi.org/10.5194/gmd-9-2685-2016, 2016.

Mataveli, G., Maure, L. A., Sanchez, A., Dutra, D. J., de Oliveira, G., Jones, M. W., Amaral, C., Artaxo, P., and Aragão, L. E. O. C.: Forest degradation is undermining progress on deforestation in the Amazon, Glob. Chang. Biol., 31, e70209, https://doi.org/10.1111/gcb.70209, 2025.

Mathison, C., Burke, E., Hartley, A. J., Kelley, D. I., Burton, C., Robertson, E., Gedney, N., Williams, K., Wiltshire, A., Ellis, R. J., and Others: Description and evaluation of the JULES-ES set-up for ISIMIP2b, Geoscientific Model Development, 16, 4249–4264, 2023.

McNorton, J. and Di Giuseppe, F.: A global fuel characteristic model and dataset for wildfire prediction, Biogeosciences, https://doi.org/10.5194/bg-21-279-2024, 2024.

McNorton, J., Agustí-Panareda, A., Arduini, G., Balsamo, G., Bousserez, N., Boussetta, S., Chericoni, M., Choulga, M., Engelen, R., and Guevara, M.: An urban scheme for the ECMWF integrated forecasting system: Global forecasts and residential CO_2 emissions, J. Adv. Model. Earth Syst., 15, e2022MS003286, https://doi.org/10.1029/2022ms003286, 2023.

Meijer, J. R., Huijbregts, M. A. J., Schotten, K. C. G. J., and Schipper, A. M.: Global patterns of current and future road infrastructure, Environ. Res. Lett., 13, 064006, https://doi.org/10.1088/1748-9326/aabd42, 2018.

Melton, J., Arora, V., Wisernig-Cojoc, E., Seiler, C., Fortier, M., Chan, E., and Teckentrup, L.: CLASSIC v1.0: the open-source community successor to the Canadian Land Surface Scheme (CLASS) and the Canadian Terrestrial Ecosystem Model (CTEM) – Part 1: Model framework and site-level performance, Geosci. Model Dev., https://doi.org/10.5194/gmd-2019-329-supplement, 2019.

Mengel, M., Treu, S., Lange, S., and Frieler, K.: ATTRICI v1. 1--counterfactual climate for impact attribution, Geoscientific Model Development, 14, 5269–5284, 2021.

Muñoz-Sabater, J., Dutra, E., Agustí-Panareda, A., Albergel, C., Arduini, G., Balsamo, G., Boussetta, S., Choulga, M., Harrigan, S., Hersbach, H., Martens, B., Miralles, D. G., Piles, M., Rodríguez-Fernández, N. J., Zsoter, E., Buontempo, C., and Jean-Noël Thépaut: ERA5-Land: a state-of-the-art global reanalysis dataset for land applications, Earth Syst. Sci. Data, 13, 4349–4383, https://doi.org/10.5194/essd-13-4349-2021, 2021.

Otto, F., van der Wiel, K., van Oldenborgh, G. J., Philip, S., Kew, S., Uhe, P., and Cullen, H.: Climate change increases the probability of heavy rains in Northern England/Southern Scotland like those of storm Desmond—a real-time event attribution revisited, Environmental Research Letters, 13, https://doi.org/10.1088/1748-9326/aa9663, 2018.

Philip, S., Kew, S., van Oldenborgh, G. J., Otto, F., Vautard, R., van der Wiel, K., King, A., Lott, F., Arrighi, J., Singh, R., and van Aalst, M.: A protocol for probabilistic extreme event attribution analyses, Adv. Stat. Clim. Meteorol. Oceanogr., 6, 177–203, https://doi.org/10.5194/ascmo-6-177-2020, 2020.

Quilcaille, Y., Batibeniz, F., Ribeiro, A. F. S., Padrón, R. S., and Seneviratne, S. I.: Fire weather index data under historical and shared socioeconomic pathway projections in the 6th phase of the Coupled Model Intercomparison Project from 1850 to 2100, Earth Syst. Sci. Data, 15, 2153–2177, https://doi.org/10.5194/essd-15-2153-2023, 2023.

Qu, Y., Jones, M. W., Brambleby, E., Hunt, H. G. P., Pérez-Invernón, F. J., Yebra, M., Zhao, L., Moris, J. V., Janssen, T., and Veraverbeke, S.: A new global gridded lightning dataset with high spatial and temporal resolution, , https://doi.org/10.5194/egusphere-egu25-8351, 2025.

Rabin, S. S., Melton, J. R., and Lasslop, G.: The Fire Modeling Intercomparison Project

(FireMIP), phase 1: experimental and analytical protocols with detailed model descriptions, Geoscientific Model, 2017.

Schaller, N., Otto, F., Oldenborgh, G. V., Massey, N., Sparrow, S., and Allen: The heavy precipitation event of may-June 2013 in the upper Danube and Elbe basins, Bulletin of the American Meteorological Society, 95, 2014.

Scholten, R. C., Jandt, R., Miller, E. A., Rogers, B. M., and Veraverbeke, S.: Overwintering fires in boreal forests, Nature, 593, 399–404, https://doi.org/10.1038/s41586-021-03437-y, 2021.

Sellar, A. A., Walton, J., Jones, C. G., and Wood, R.: Implementation of UK Earth system models for CMIP6, Journal of Advances, 2020.

Sexton, J. O., Noojipady, P., Song, X.-P., Feng, M., Song, D.-X., Kim, D.-H., Anand, A., Huang, C., Channan, S., Pimm, S. L., and Townshend, J. R.: Conservation policy and the measurement of forests, Nat. Clim. Chang., 6, 192–196, https://doi.org/10.1038/nclimate2816, 2016.

Smith, B., Wårlind, D., Arneth, A., Hickler, T., Leadley, P., Siltberg, J., and Zaehle, S.: Implications of incorporating N cycling and N limitations on primary production in an individual-based dynamic vegetation model, Biogeosciences, 11, 2027–2054, https://doi.org/10.5194/bg-11-2027-2014, 2014.

Spuler, F., Wessel, J., Comyn‐Platt, E., Varndell, J., and Cagnazzo, C.: ibicus: a new open-source Python package and comprehensive interface for statistical bias adjustment and evaluation in climate modelling (v1.0.1), Geosci. Model Dev., https://doi.org/10.5194/gmd-17-1249-2024, 2024.

ibicus: https://pypi.org/project/ibicus/, last access: 7 August 2024.

Swart, N. C., Cole, J. N. S., Kharin, V. V., Lazare, M., Scinocca, J. F., Gillett, N. P., Anstey, J., Arora, V., Christian, J. R., Hanna, S., Jiao, Y., Lee, W. G., Majaess, F., Saenko, O. A., Seiler, C., Seinen, C., Shao, A., Solheim, L., von Salzen, K., Yang, D., and Winter, B.: The Canadian Earth System Model version 5 (CanESM5.0.3), Geosci. Model Dev. Discuss., 1–68, https://doi.org/10.5194/gmd-2019-177, 2019.

Thonicke, K., Venevsky, S., Sitch, S., and Cramer, W.: The role of fire disturbance for global vegetation dynamics: coupling fire into a Dynamic Global Vegetation Model, Glob. Ecol. Biogeogr., 10, 661–677, https://doi.org/10.1046/j.1466-822x.2001.00175.x, 2008.

Thonicke, K., Spessa, A., Prentice, I. C., Harrison, S. P., Dong, L., and Carmona-Moreno, C.: The influence of vegetation, fire spread and fire behaviour on biomass burning and trace gas emissions: results from a process-based model, Biogeosciences, 7, 1991–2011, https://doi.org/10.5194/bg-7-1991-2010, 2010.

Torres-Vázquez, M. Á., Herrera, S., Gincheva, A., Halifa-Marín, A., Cavicchia, L., Di Giuseppe, F., Montávez, J. P., and Turco, M.: Enhancing seasonal fire predictions with hybrid dynamical and random forest models, NPJ Nat. Hazards, 2, 1–10, https://doi.org/10.1038/s44304-025-00069-4, 2025.

Turco, M., Jerez, S., Doblas-Reyes, F. J., AghaKouchak, A., Llasat, M. C., and Provenzale, A.: Skilful forecasting of global fire activity using seasonal climate predictions, Nat. Commun., 9, 2718, https://doi.org/10.1038/s41467-018-05250-0, 2018.

Turco, M., Jones, M. W., and Di Giuseppe, F.: State of Wildfires 2024-25: Anomalies in

Extreme Fire Weather Days by Continent, Biome, Country, and Administrative Region, https://doi.org/10.5281/zenodo.15538595, 2025.

UNEP, Popescu, A., Paulson, A. K., Christianson, A. C., Sullivan, A., Tulloch, A., Bilbao, B., Mathison, C., Robinson, C., Burton, C., Ganz, D., Nangoma, D., Saah, D., Armenteras, D., Driscoll, D., Hankins, D. L., Kelley, D. I., Langer, E. R. L., Baker, E., Berenguer, E., Reisen, F., Robinne, F.-N., Galudra, G., Humphrey, G., Safford, H., Baird, I. G., Oliveras, I., Littell, J., Kieft, J., Chew, J., Maclean, K., Wittenberg, L., Anderson, L. O., Gillson, L., Plucinski, M., Moritz, M., Brown, M., Soto, M. C., Flannigan, M., Costello, O., Silva, P. S., Fernandes, P., Moore, P., Jandt, R., Blanchi, R., Libonati, R., Archibald, S., Dunlop, S., McCaffrey, S., Page, S., Gonzãƒâ¡lez, T. D. T., Sokchea, T., and Charlton, V.: Spreading like Wildfire: The Rising Threat of Extraordinary Landscape Fires, edited by: Sullivan, A., Kurvits, T., and E., B., United Nations Environment Programme and GRID-Arendal., 2022.

Vitolo, C., Di Giuseppe, F., Barnard, C., Coughlan, R., San-Miguel-Ayanz, J., Libertá, G., and Krzeminski, B.: ERA5-based global meteorological wildfire danger maps, Sci. Data, 7, 216, https://doi.org/10.1038/s41597-020-0554-z, 2020.

van Wagner, C. E.: Development and structure of the Canadian forest fire weather index system, cabidigitallibrary.org, https://doi.org/10.5555/19910646918, 1987.

van der Wiel, K., Kapnick, S. B., van Oldenborgh, G. J., Whan, K., Philip, S., Vecchi, G. A., Singh, R. K., Arrighi, J., and Cullen, H.: Rapid attribution of the August 2016 flood-inducing extreme precipitation in south Louisiana to climate change, Hydrol. Earth Syst. Sci., 21, 897–921, https://doi.org/10.5194/hess-21-897-2017, 2017.

Yue, C., Ciais, P., Cadule, P., Thonicke, K., Archibald, S., Poulter, B., Hao, W., Hantson, S., Mouillot, F., Friedlingstein, P., Maignan, F., and Viovy, N.: Modelling the role of fires in the terrestrial carbon balance by incorporating SPITFIRE into the global vegetation model ORCHIDEE – Part 1: simulating historical global burned area and fire regimes, Geoscientific Model Development, 7, 2747–2767, https://doi.org/10.5194/GMD-7-2747-2014, 2014.

Yue, C., Cadule, P., and Van Leeuwen, T. T.: Modelling the role of fires in the terrestrial carbon balance by incorporating SPITFIRE into the global vegetation model ORCHIDEE--Part 2: Carbon emissions and the role of fires in the global carbon balance, Geoscientific Model Development, 8, 1321–1338, 2015.

Zheng, B., Ciais, P., Chevallier, F., Yang, H., Canadell, J. G., Chen, Y., van der Velde, I. R., Aben, I., Chuvieco, E., Davis, S. J., Deeter, M., Hong, C., Kong, Y., Li, H., Li, H., Lin, X., He, K., and Zhang, Q.: Record-high CO2 emissions from boreal fires in 2021, Science, 379, 912–917, https://doi.org/10.1126/science.ade0805, 2023.

Zubkova, M., Giglio, L., Boschetti, L., Roy, D., Hall, J., and Humber, M. L.: The NASA Visible Infrared Imaging Radiometer Suite (VIIRS) burned area product - VNP64A1, AGUFM, 2024, B13I–1644, 2024.